Photomixed terahertz emitters by multipolar photoconductive terahertz antennas

Alaeddine Abbes

THESIS TO OBTAIN THE DEGREE OF DOCTOR FROM THE UNIVERSITY OF MONTPELLIER

In Electronics

Doctoral school: Information, Structures and Systems

Research unit: Institute of Electronics and Systems – UMR 5214

Photomixed terahertz emitters by multipolar photoconductive terahertz antennas

Presented by Alaeddine ABBES

On December 13, 2021

Under the supervision of Stéphane BLIN and Luca VARANI

In front of the jury composed of

Arnaud GARNACHE, Director of research CNRS, University of Montpellier	President
Guillaume DUCOURNAU, Professor, University of Lille	Reviewer
Julien POËTTE, Associate Professor HDR, Grenoble Alpes University	Reviewer
Vasilis APOSTOLOPOULOS, Associate Professor HDR, University of Southampton	Examinator
Mona JARRAHI, Professor, University of California Los Angeles	Examinator
Annick PÉNARIER, Associate Professor, University of Montpellier	Examinator
Stéphane BLIN, Associate Professor HDR, University of Montpellier	Supervisor
Luca VARANI, Professor, University of Montpellier	Co-supervisor

UNIVERSITÉ DE MONTPELLIER

THÈSE POUR OBTENIR LE GRADE DE DOCTEUR DE L'UNIVERSITÉ DE MONTPELLIER

En Électronique

École doctorale : Information, Structures et Systèmes

Unité de recherche : Institut d'Électronique et des Systèmes – UMR 5214

Sources térahertz photo-mélangées par antennes photoconductrices térahertz multipolaires

Présentée par Alaeddine ABBES
Le 13 décembre 2021

Sous la direction de Stéphane BLIN et Luca VARANI

Devant le jury composé de

Arnaud GARNACHE, Directeur de recherche CNRS, Université de Montpellier	Président
Guillaume DUCOURNAU, Professeur, Université de Lille	Rapporteur
Julien POËTTE, Maître de conférences HDR, Université Grenoble Alpes	Rapporteur
Vasilis APOSTOLOPOULOS, Maître de conférences HDR, Université de Southampton	Examinateur
Mona JARRAHI, Professeur, Université de Californie Los Angeles	Examinatrice
Annick PÉNARIER, Maître de conférences, Université de Montpellier	Examinatrice
Stéphane BLIN, Maître de conférences HDR, Université de Montpellier	Directeur de thèse
Luca VARANI, Professeur, Université de Montpellier	Co-directeur de thèse

UNIVERSITÉ DE MONTPELLIER

Dedicated to my parents
and my little sister...

Innamorati di un'attività *e perditici completamente.*
Nessuno ha mai capito qual è lo ***scopo della vita****, e va bene così.*
Esplora il mondo.
Qualsiasi cosa può essere interessante ***se l'approfondisci abbastanza****.*
Lavoro sodo e per tutto il tempo che desideri *sulle cose che ti dà soddisfazione fare al meglio.*
Per il resto, fai il minimo necessario affinché la società non ti impedisca di fare quello che ami davvero.
Nella vita non conta chi vuoi ***essere****, ma a cosa vuoi* ***fare****.*
- Richard Feymann

Acknowledgements

This work and this experience at IES would have not been possible without the help and the support of my parents throughout my academic path. I always have learnt several things from them, especially those that are not clearly visible, but unconsciously form your character day by day. They deserve the first thanks for all of their efforts during these last 30 years...

I would like to thank Prof. *Guillaume Ducournau* and Prof. *Julien Poëtte* for having accepted to evaluate this work.

I would like to thank Prof. *Mona Jarrahi* and Prof. *Vasilis Apostolopoulos* for having accepted to be part of my jury despite their busy schedule. It was such an honor! I also appreciate their remarks and questions.

I am also grateful to Dr. *Arnaud Garnache* for having accepted to be the president of the jury and for his help for the PhD defense preparation as well as his remarks.

I would like to express my deep gratitude to Prof. *Stéphane Blin* and Prof. *Luca Varani*, my research supervisors. Their advices, patience and their time to read my manuscript have been fundamental to achieve the obtained results.

I would like to thank to the permanent staff of our group, especially to Dr. *Philippe Nouvel* and Prof. *Annick Plagellat-Pénarier*.

I would like to thank our collaborators from UCLA Prof. *Mona Jarrahi* and her PhD student *Ping Keng Lu* for giving the opportunity to visit their lab and for providing us their beautiful devices. The performances achieved in this work are with no doubt related to the high quality of their dies.

Many thanks goes also to my collaborator Dr. *Ramin Emadi* for our fruitful discussions. I really appreciate to work with you.

I would like to thank Prof. *Fernardo Gonzalez-Posada* and clean-room Engineer *Frédéric Pichot* for the training in the clean-room and their long expertise on device fabrication which they kindly shared with me. These skills will be surely useful in the future to fabricate next-generation optoelectronic devices by collaborating with researchers and engineers of the RENATECH network.

I am also grateful to all the people I have met during four years for their friendship and the time spent discussing, playing football/basketball or simply eating/drinking good beers together. Most of them coming from almost all the research groups at IES: Dr. *Isidore Diouf*, Dr. *Mohamed Hammoud*, Dr. *Amine Bassli*, *Mahi Mohamed Touré*, Dr. *Rebecca El-Koussaifi*, Dr. *Baptiste Chomet*, Dr. *Rémi Dardaillon*, *Sebastien Gebert*, *Anastasiia Kudashova* and *Nathan Vigne* from our group, Dr. *Afaf Meghit*, Dr. *Amandine Sandoval*, Dr. *Methapettyparambu Purushothama Jayakrishnan* (*aka JK*), Dr. *Florian Baudry*, *Léo Chamard*, Dr. *Rudy Desgarceaux*, *Claire Jolly*, *David Sanchez*, *Abdelhak Megzari* from M2A group (now RFEF/M2N/ACO groups), Dr. *Eduardo Alvear-Cabezón*, Dr. *Daniel Andrés Díaz Thomas*, Dr. *Zeineb Loghmari*, Dr. *Olivier Delorme*, *Wioletta Trzpil* and *Julien Guise* from NANOMIR group, *Abdallah Oukms*, Dr. *Lorenzo Piscini*, *Sneha Hedge*, *Amine Iklil*, *Mourad Aitakkache* from GEM group, *Samir Bouisri* from RADIAC group. Also, Dr. *Sylvain Dutrieux* and *Manon Chevalier* from Bonetag company and other people coming from IGF (Institut de Génétique Fonctionnelle), especially *Yann Dromard*, *Jordi Haubrich*, *Anthony Pinot*, *Steeve Thirard*, Dr. *Damien Huzard* and many others.

Another special thanks go to my best friends from Italy, the trio *Claudio Saudino*, *Davide Saudino* and *Mickael Rossi*. Forgive me if I wasn't able to come back in Italy regularly during my academic path but I promise you that now I have more freedom to travel, especially to meet some well–know italian researchers ;)

Special thanks go to also my another best friend, *Deniz Tohumcu*. He is now an Engineer in integrated electronics and consultant in a top 500 company, you deserve it well. Don't worry, one day we will found a company together, just to enjoy!

Special thanks go to *Benjamin Saggin*, my colleague as well as my best friend. He is the best person I could ever met. You had always such an optimism and faith on me, I really appreciate it. You will be able to follow your ultimate dream. Unfortunately, the time has come where our paths diverge but I promise that I will come back soon (somewhere in France excluding Montpellier and Paris héhé :D).

Last but not least, I want to adress my largest thanks to the person that has changed my life the most, my beloved partner *Loona* (a PhD student too and we defended our thesis the same month!). Her daily presence has made my life thousand times happier than what I could barely imagine. Her incredibly contagious and constant optimism in everything has been my strongest motivation in giving the best from myself. I leave for a new experience being aware that this time, from the beginning, we will be together facing new challenges in Canada and achieve our biggest dreams.

Contents

List of Figures

List of Tables

Acronyms

CMOS Complementary Metal-Oxide-Semiconductor.

CST Computer Simulation Technology.

DAST trans–4′–(DimethylAmino)–N–methyl–4–Stilbazolium Tosylate.

DF–VeCSEL Dual–Frequency Vertical External Cavity Surface–Emitting Laser.

DFB Distributed FeedBack.

ESA Electrical Spectrum Analyzer.

FIT Finite Integral Technique.

FSR Free Spectral Range.

FWHM Full Width at Half Maximum.

HEMT High Electron Mobility Transistor.

IMPATT IMPact ionization Avalanche Transit-Time.

IR InfraRed.

LG Laguerre-Gauss.

LT Low Temperature.

MIMO Multiple Input Multiple Output.

MITATT MIxed Tunneling Avalanche Transit-Time.

MM MultiMode.

MMIC Monolithic Microwave Integrated Circuit.

MOCVD Metal–Organic Chemical Vapor Deposition.

MP MultiPolar antenna.

NTT Nippon Telegraph and Telephone Corporation.

OAM Orbital Angular Momentum.

OSA Optical Spectrum Analyzer.

PCA PhotoConductive Antenna.

PEC Perfect Electric Conductor.

PER Polarization Extinction Ratio.

PIN P-type/Intrinsic/N-type diode structure.

PM Polarization Maintaining.

QCL Quantum Cascade Laser.

RF Radio–Frequency.

RIN Relative Intensity Noise.

RT Room Temperature.

RTA Rapid Thermal Annealing.

RTD Resonant–Tunelling Diode.

SEM Scanning Electron Microscope.

SESAM SEmiconductor Saturable Absorber Mirror.

SM Single Mode.

SMSR Side–mode Suppression Ratio.

SMU Source Measure Unit.

TEM Transverse Electro–Magnetic mode.

THz TeraHertz.

THz-QCL Terahertz Quantum Cascade Laser.

TLM Transmission Line Measurement.

TM Transverse Magnetic.

TUNNETT TUNNEl injection Transit–Time negative resistance.

UTC–PD Uni–Travelling Carriers Photo-Diodes.

VeCSEL Vertical External Cavity Surface–Emitting Laser.

Introduction

A powerful, coherent, tunable, compact, low–cost THz source operating at room temperature is required for a large variety of applications such as astronomy, non–destructive control, biology, medicine and communication. Several types of THz radiation sources have been developed, based on pure electronic methods (e.g. systems based on frequency multiplication in nonlinear devices such Schottky diodes) or pure optical methods (e.g. pulsed optical rectification in non–linear crystals). Each methods present advantages and disadvantages: but in all cases they are typically cumbersome (thus expensive) and/or they present physical limits (such as 3 dB cut–off of electronic sources). Also, they are limited by power (the power drops at higher frequencies for electronic sources), working temperature (e.g. THz–QCL is efficient at low temperature), bandwidth and coherence. More recently, photonic solutions have been proposed in the context of developing THz radiation sources. A first axis consists in developing THz quantum cascade lasers. If these sources are efficient in the infrared range, in the THz range they require the use of cryogenic techniques and are difficult to tune. Another axis combines the advantages of electronic and photonic sources. Two near–frequency lasers (frequency difference in the THz range) produce an optical beating exciting a photoconductive material. The latter, modulating the conductivity of a biased antenna, radiates in the free–space. In the CW regime, they are called "photomixer" and in the pulsed regime, they are called "photoconductive antenna". These devices exploit mature photonic technologies and they are limited only to their optical performances (especially coherence). However, they remain limited in terms of available power output due to the low optical–to–THz conversion efficiency. An initial work on dual–frequency VeCSEL in TéHO (now PhoTéra) research group was carried out in the thesis of R. Paquet. In fact, VeCSELs solutions provide promising features that are not available in any other kind of lasers. These features are all combined: power while maintaining high coherence in terms of polarization, spatially and spectrally, robustness, high–tunability and compactness (quasi–monolithical solution). All of these features operate at room temperature. This thesis continued in this line developing original antennas for photomixers with the aim to increase THz output power.

Outline

The next chapters are organized as follows:

Chapter 1 introduces the state of the art of THz sources and photomixers.

Chapter 2 introduces the state of the art of dual–frequency lasers and explains the choice of

using VeCSELs technology as dual–frequency laser for THz generation.

Chapter 3 is the core of this thesis and focused on THz antenna design for photo–mixers. Initially designed for photo-conductors (PCA), it can be also applied to photo–diodes (in particular UTC–PD). A part of this study has been done (results not included in this manuscript) in collaboration with Dr. R. Emadi from Isfahan University of Technology (Iran).

Chapter 4 is focused on photomixers. SESAM as potential photomixer for THz generation is explored and discussed. This other study concerns the use of InGaAs plasmonic–based photomixers driven by a DF–VeCSEL in collaboration with the PhD student P.–K. Lu and Prof. M. Jarrahi from UCLA (USA). THz power emission is experimentally demonstrated and discussed. These works appear in *2021 46th International Conference on Infrared, Millimeter, and Terahertz Waves* (*IRMMW–THz*).

Résumé

Une source térahertz continue, puissante, cohérente, accordable, compacte, bas coût et fonctionnant à température ambiante est requise pour des applications telles que l'astronomie, le contrôle non destructif, le biomédical et les télécommunications. À l'heure actuelle, peu de sources répondent à ces caractéristiques, la plupart étant difficilement implantable dans le marché. L'objectif de cette thèse est donc de concevoir de nouvelles antennes térahertz pour la génération térahertz par photo-mélange. Cette thèse s'est déroulée à l'Institut d'Électronique et des Systèmes (IES) de l'Université de Montpellier.

Le manuscrit est composé des quatre chapitres suivants :

Dans le **premier chapitre**, un état de l'art est dressé sur les sources THz en général et sur les sources THz basés sur le photo–mélange. Les avantages et les inconvénients des sources électroniques et photoniques seront mentionnés. Enfin, l'approche la plus utilisée actuellement, basée sur le principe de photo–mélange, sera présentée. Trois photomélangeurs sont typiquement utilisés pour l'émission THz, que ce soit en régime pulsé ou continu: les cristaux non–linéaires, les photodiodes à transport unipolaire et les antennes photoconductrices. Leurs avantages et inconvénients sont également mentionnés. Ces trois photomélangeurs peuvent être utilisés dans ou en dehors de la cavité laser bifréquence, selon le type du laser utilisé.

Le **deuxième chapitre** traite de l'état de l'art des sources lasers bi–fréquences et justifie le choix des technologies laser de type VeCSEL (Vertical External Cavity Semiconductor Laser) fonctionnant à $1064\ \mathrm{nm}$ pour la génération THz. Il existe plusieurs types de lasers bi–fréquence, basé sur des technologies fibrés ou semiconductrices. Trois approches permettent de sélectionner deux longueurs d'onde : par modes longitudinaux, par modes de polarisation et par modes transverses. Le principe du VeCSEL bi-fréquence qui est exploité ici est de stabiliser deux modes transverses dans la cavité. Disposer uniquement de deux longueurs d'onde au sein d'une même cavité n'est pas anodin. Si le milieu de l'amplificateur laser offre un milieu de gain homogène, une compétition se produit et le mode le plus fort reste, tandis que le mode le plus faible disparaît. Cependant, un grand nombre de modes coexistent si un milieu de gain inhomogène est utilisé, ou en présence d'effets non linéaires. La configuration du VeCSEL est illustrée sur la Fig. 2.9 (gauche). Une puce semi–conductrice se compose d'un miroir de Bragg à haute réflectivité et de plusieurs puits quantiques qui sont pompés optiquement. La cavité optique en espace libre de $10\ \mathrm{cm}$ de long est fermée par un miroir diélectrique externe. Des masques métalliques sont déposés sur le dessus de la structure semi-conductrice pour sélectionner les deux modes transverses souhaités dans la cavité grâce à des pertes sélectives,

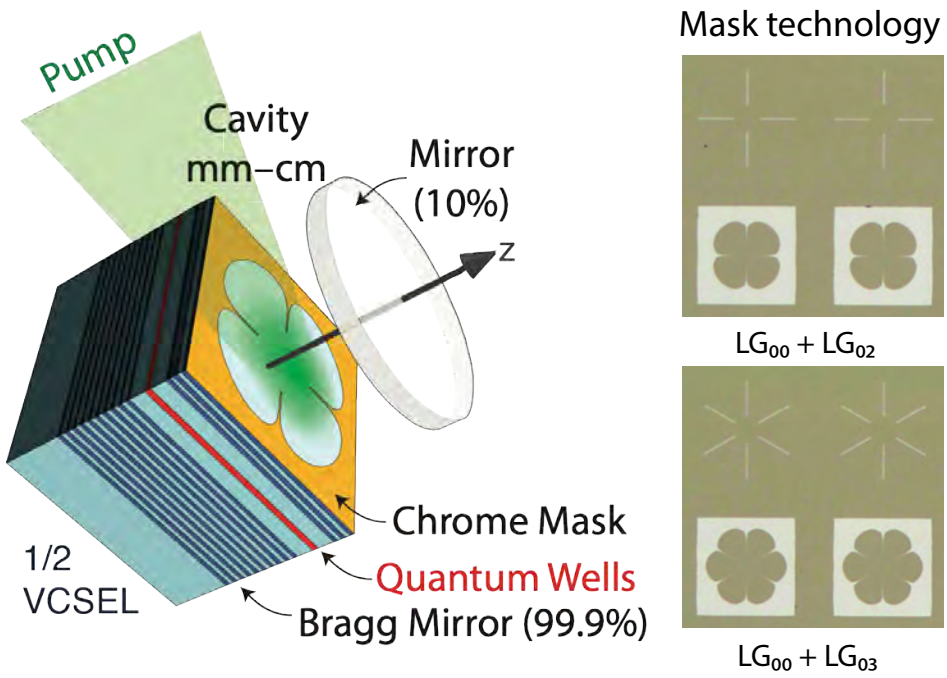

Figure 1 – *Technologie VeCSEL: Gauche) Design et technologie VeCSEL. Cavité courte plano–concave pour l'émission bi–bifréquence. Droite) Masques métalliques pour les modes tranverses* LG_{00} *plus* LG_{0m} *(*$m = 2, 3$ *ici).*

en plus d'un diamètre de faisceau de pompe bien défini pour la sélection du gain modal. Un fonctionnement robuste en double mode transverse est observé dans une telle structure (Fig. 2.9). Des conceptions de masques spécifiques, comme montré dans la Fig. 2.9 (droite), ont permis de démontrer la coexistence de couples de modes de Laguerre Gauss (LG) typiques LG_{00}/LG_{02}, LG_{00}/LG_{03}, ou LG_{00}/LG_{04}. Le fonctionnement en double fréquence se produit grâce au pompage optique qui créé un gradient thermique avec une distribution cylindrique. En conséquence, le mode fondamental (LG_{00}) fonctionne à une température modale plus élevée que les modes d'ordre supérieur (LG_{02}, LG_{03} ou LG_{04}) qui sont exempts d'énergie au centre. Lorsque la puissance de la pompe augmente, le gradient thermique se renforce et la différence de fréquence entre les modes augmente, offrant ainsi une fréquence de battement accordable pour la génération THz, pilotée par la puissance de la pompe optique. Le couple de modes LG_{00}/LG_{03} offre un spectre très stable et cohérent pour toute fréquence de battement dans la gamme 50–900 GHz.

D'après les propriétés du VeCSEL, les deux lignes optiques sont cohérentes (mode longitudinal unique, largeur de ligne spectrale étroite, polarisation unique), et la puissance de sortie totale peut atteindre 80 mW pour un pompage optique de 400 mW [3]. La puissance optique du laser injectée dans la fibre monomode dépend du masque choisi, de quelques dizaines de µW pour les modes LG_{00}/LG_{04} à quelques mW pour les modes LG_{00}/LG_{04}. Des mesures de bruit de fréquence dans le domaine optique et dans le domaine THz ont été réalisées lors d'une précédente thèse et ont montré que le bruit de fréquence du signal de battement était inférieur de 4 ordres de grandeur au bruit de fréquence optique, montrant l'intérêt d'utiliser un laser bi–fréquence par rapport à deux lasers individuels [3]. Les perturbations techniques sont en effet identiques pour les deux modes, et se soustraient lors du battement. L'émission THz a été obtenue en utilisant une photodiode ultra–rapide (UTC–PD) pour le photomélange,

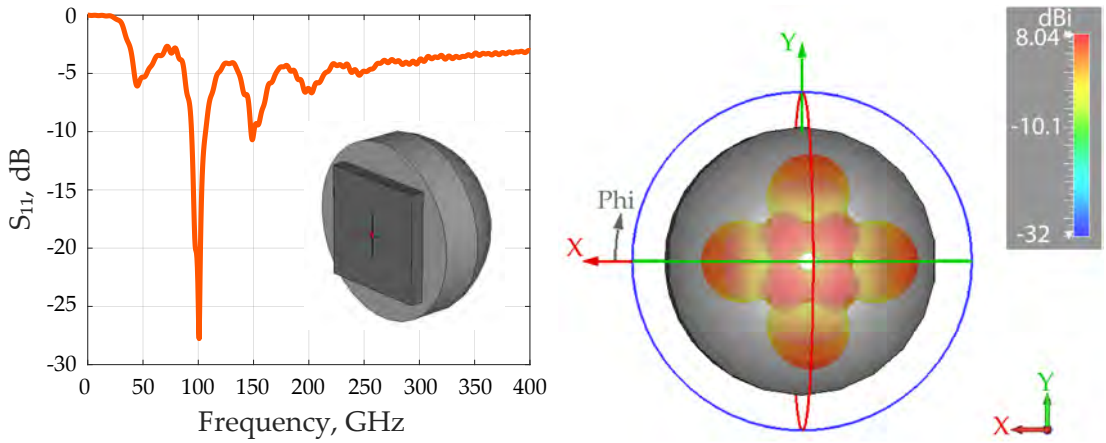

Figure 2 – *Résultats de simulations: Gauche) Paramètres S_{11} de l'antenne multipolaire MP_2 (MP: Multipolar, 2 antennes dipôles croisées). Encart: MP_2 avec une lentille Silicium. Droite) Résultat du champ lontain de MP_2 à* 100 GHz.

mais ces photodiodes sont conçues pour une excitation à 1550 nm, ce qui réduit l'efficacité de la conversion optique en THz et motive l'étude de photomélangeurs conçus pour 1064 nm [3].

Le **troisième chapitre** est le cœur du sujet de thèse et se focalise sur le design d'antennes THz multipolaires. Initialement designées pour les antennes photoconductrices, elles peuvent être utilisées pour les photodiodes à transport unipolaire. Les travaux d'une précédente thèse ont été effectués en utilisant une fibre optique monomode pour collecter le battement optique d'un des lobes des modes transverses. Collecter les battements optiques présents dans tous les lobes permet d'augmenter la puissance THz. Les antennes multipolaires ont été choisies afin de collecter tout le battement optique disponible dans les modes transverses définis précédemment et donc maximiser la puissance THz disponible. Pour cela, des études en simulation numériques sous le logiciel CST ont été effectuées afin de quantifier les pertes dues au couplage électromagnétique. Il s'avère que ces antennes peuvent être utilisées dans un contexte de multiplication du nombre de battement. En effet, malgré un couplage électromagnétique fort, ces antennes ont des gains supérieurs aux antennes classiques (notamment les antennes dipolaires). Pour plus de simplicité, les antennes multipolaires ont été conçues en utilisant un croisement d'antennes dipolaires. Cela permettrait donc de limiter le couplage électromagnétique. Le gain comme l'efficacité d'une antenne sont les deux paramètres fondamentaux pour le choix d'antennes appropriées. L'étude de couplage pour différentes antennes multipolaires a été effectuée pour quantifier à quel point il affecte leurs performances (6 dBi pour deux dipôles croisés versus 2 dBi pour un dipôle simple). Dans la Fig. 2, nous montrons le résultat quand une antenne multipolaire est placée sur une permittivité plus élevée que l'air, ce qui permet de mieux se rapprocher de l'expérience.

Le **quatrième chapitre** se focalise sur les photo–mélangeurs. Le SESAM (Semiconductor Saturable Absorber Mirror) en tant que photomélangeur pour la génération THz est exploré et discuté. L'effet photoconducteur observé donne une perspective encourageante, menant ce type de composant dans l'utilisation en tant que photomélangeur pour la génération THz. Une autre étude concerne l'utilisation d'un photomélangeur à base d'électrodes plasmoniques excité par le laser bifréquence, en collaboration avec le doctorant P.–K. Lu et le Prof. M. Jarrahi de l'UCLA

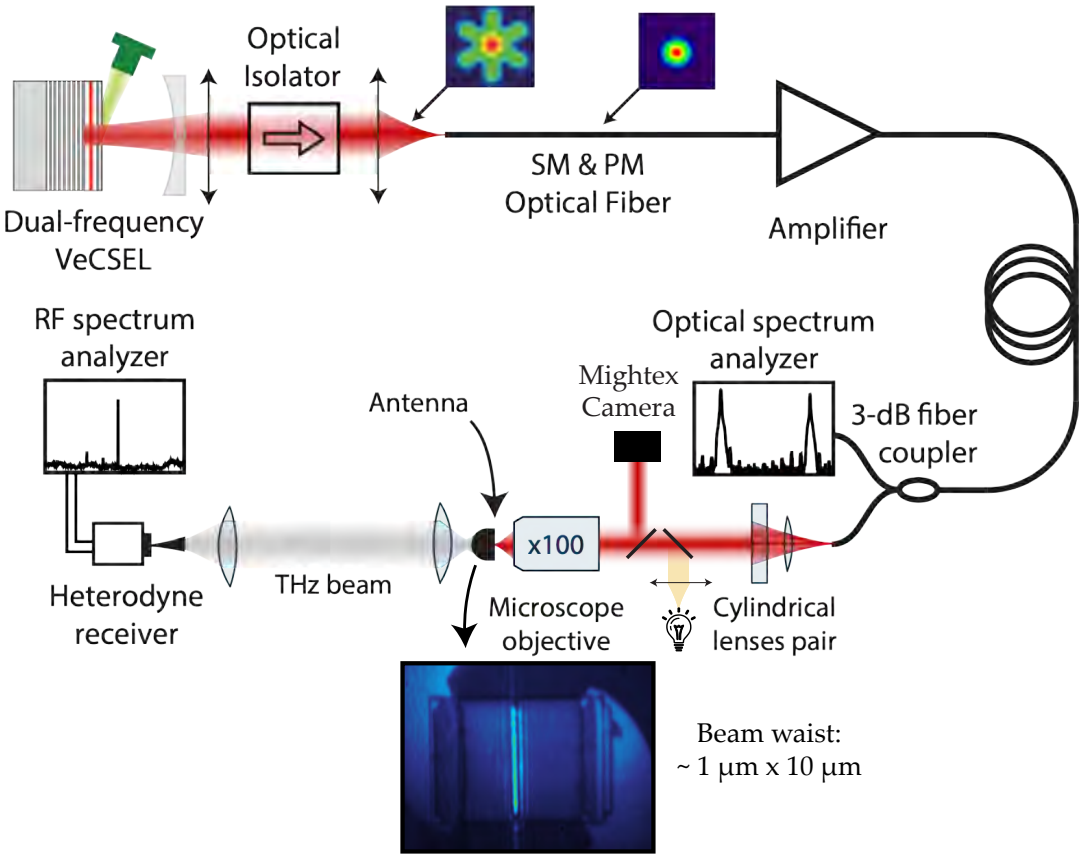

Figure 3 – *Banc expérimental pour l'émission THz en utilisant le VeCSEL bi–fréquence et les photoconducteurs à électrodes plasmoniques. Les photoconducteurs sont à base de InGaAs/GaAs absorbant à* $1064\ \mathrm{nm}$ *en utilisant soit une antenne spirale soit une antenne dipole. Le gap entre les électrodes plasmoniques est de* $1\ \mu\mathrm{m}$.

(USA). Ce photomélangeur est fabriqué sur une structure semi-conductrice épitaxiale constituée d'une couche d'$In_{0.24}Ga_{0.76}As$ non dopée de $200\ \mathrm{nm}$ d'épaisseur et d'une couche d'AlAs de $200\ \mathrm{nm}$ d'épaisseur obtenue par épitaxie par jets moléculaires sur un GaAs semi–isolant. La couche photoconductrice est intégrée à une antenne en spirale logarithmique à large bande et à des électrodes de contacts plasmoniques. Les électrodes de contacts plasmoniques fournissent un temps de transit inférieur à la picoseconde pour la majorité des porteurs photo-générés afin de permettre le photomélange aux fréquences THz sans utiliser un substrat à courte durée de vie des porteurs. Le dispositif est collé sur une lentille en Si à haute résistivité pour améliorer la puissance de sortie THz et réduire la divergence du faisceau. Le setup est présenté sur la Fig. 3. La sortie optique du laser bifréquence est collimatée et injectée dans une fibre monomode à maintien de polarisation qui est décalée par rapport à l'axe optique afin de coupler les modes LG_{00} et LG_{03}. L'alignement de la fibre permet d'égaliser la puissance des deux lignes laser, offrant ainsi un battement optimisé. Le signal est ensuite amplifié à l'aide d'un amplificateur Yb afin de maintenir une puissance de sortie constante tout en accordant la fréquence de battement grâce à la puissance de pompe du laser. Le faisceau optique amplifié est ensuite collimaté et focalisé sur le photomélangeur à l'aide de deux lentilles cylindriques et d'une lentille asphérique pour créer un faisceau ponctuel elliptique autour de l'espace de l'antenne (image sur la Fig. 3). Le faisceau ponctuel elliptique est utilisé pour maximiser la génération de photoporteurs en couvrant la totalité de l'espace entre les deux électrodes plasmoniques. Le faisceau THz généré est collimaté à l'aide d'une lentille en téflon et focalisé avec une autre lentille identique dans un récepteur à tête hétérodyne calibré. La figure 4 montre le spectre

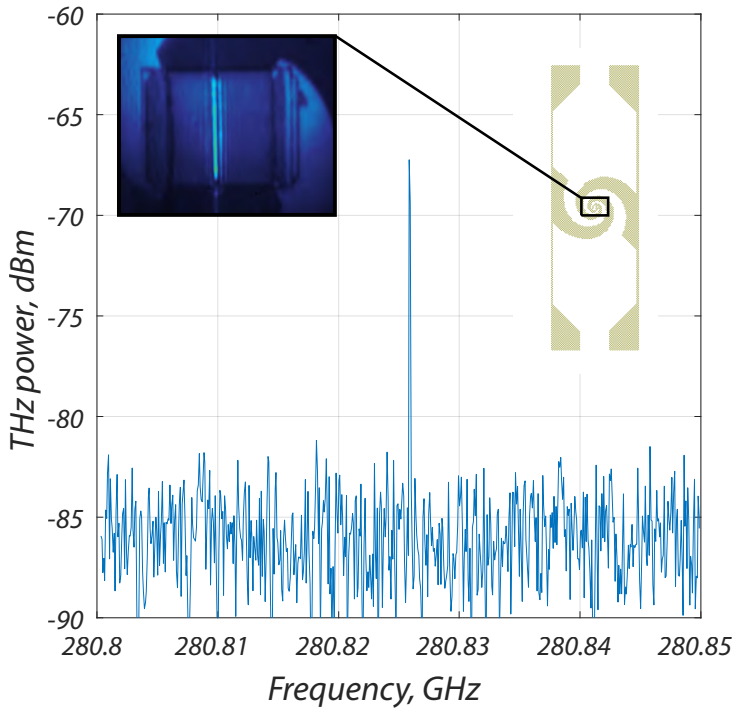

Figure 4 – *Émission THz autour de* 280 GHz *issue d'une antenne à électrodes plasmoniques excitée par le laser bifréquence.*

de puissance THz mesuré, indiquant clairement une fréquence de rayonnement de 280 GHz pour une puissance optique entrante de $\sim$ 30 mW. Malgré une puissance relativement faible, ces résultats donnent ainsi une perspective encourageante pour utiliser ce composant dans la cavité VeCSEL, pouvant mener à un système de conversion opto–THz cohérent, puissant, accordable et compacte.

Pour conclure, la génération THz continue en utilisant le laser bi–fréquence VeCSEL couplé avec les photo–mélangeurs à électrodes plasmoniques a été démontrée pour la première fois en utilisant des sources photoniques et des photoconducteurs fonctionnant à 1064 nm. Cependant, la puissance THz reste relativement faible comparé à l'état de l'art (en utilisant d'autres approches et/ou techniques d'émission THz). Un laser bi–fréquence puissant est nécessaire pour pouvoir augmenter la puissance THz tout en préservant la cohérence (spatiale et temporelle) et l'accordabilité du laser bifréquence. Une antenne multipolaire avec des électrodes plasmoniques ou un réseau des photodiodes à transport uni–polaire pourraient être utilisés pour augmenter la puissance THz de manière significative.

Chapter 1

Overview of THz Sources

Introduction

Terahertz, also called THz or T–rays or even far–infrared, matches with 10^{12} Hz frequencies range. THz waves are situated in the range between microwave and optical frequencies of the electromagnetic spectrum, as shown in the Fig. 1.1a. It is generally assumed that these waves cover the electromagnetic spectrum from 0.1 to 30 THz (i.e. wavelengths in the range from 3 mm to 10 μm) [7, 8]. Since many years, it has been shown that THz waves offer new application possibilities in the fields of spectroscopy [9], biotechnology [10–14], astronomy [15–19], communication [20–26], imaging [27–30], non-destructive control [31] and security [32]. Emerging technologies such as plasmonic–based THz devices [33] or THz metasurfaces [34] and the rapid growth of research interest in THz technologies [35] will probably make them critical players of the technological scenario during the current century. However, the development of these applications depends on the availability of efficient sources. This will require the improvement of existing solutions, by increasing oscillation frequencies for microwave sources or wavelengths for optical sources. Yet, these classic sources of radiation, coming from these two neighboring domains, are characterized by a significant drop of their emission power as they approach the THz frequency range of the electromagnetic spectrum. Hence the name "THz gap" is currently used to indicate the lack of THz sources. In order to situate our approach within these different solutions, a state of the art of existing THz compact sources is drawn up. The powers reached at THz frequencies for purely electronic and optical approaches as well as the combination of these technologies are also showed.

THz radiation can also probe low energy light–matter interactions. These interactions include phonons in solid [36], the rotational transition of molecules and the vibrational modes of large molecules [37]. THz waves can be used to characterize or identify many materials such as solid crystals, gases, polar liquids, and composites, which makes THz technology applicable for biosensing [38], chemical identification [39] and material characterization applications [40]. The energy of photons at THz frequencies is non–ionizing and non–destructive, therefore, THz waves offer many promising and unique applications in biomedicine [41] and non–destructive evaluation [42]. Most of the materials that are opaque in the visible region of the electromagnetic spectrum are much more transparent at THz frequencies. Thus, THz waves can also be used for security screening applications [43].

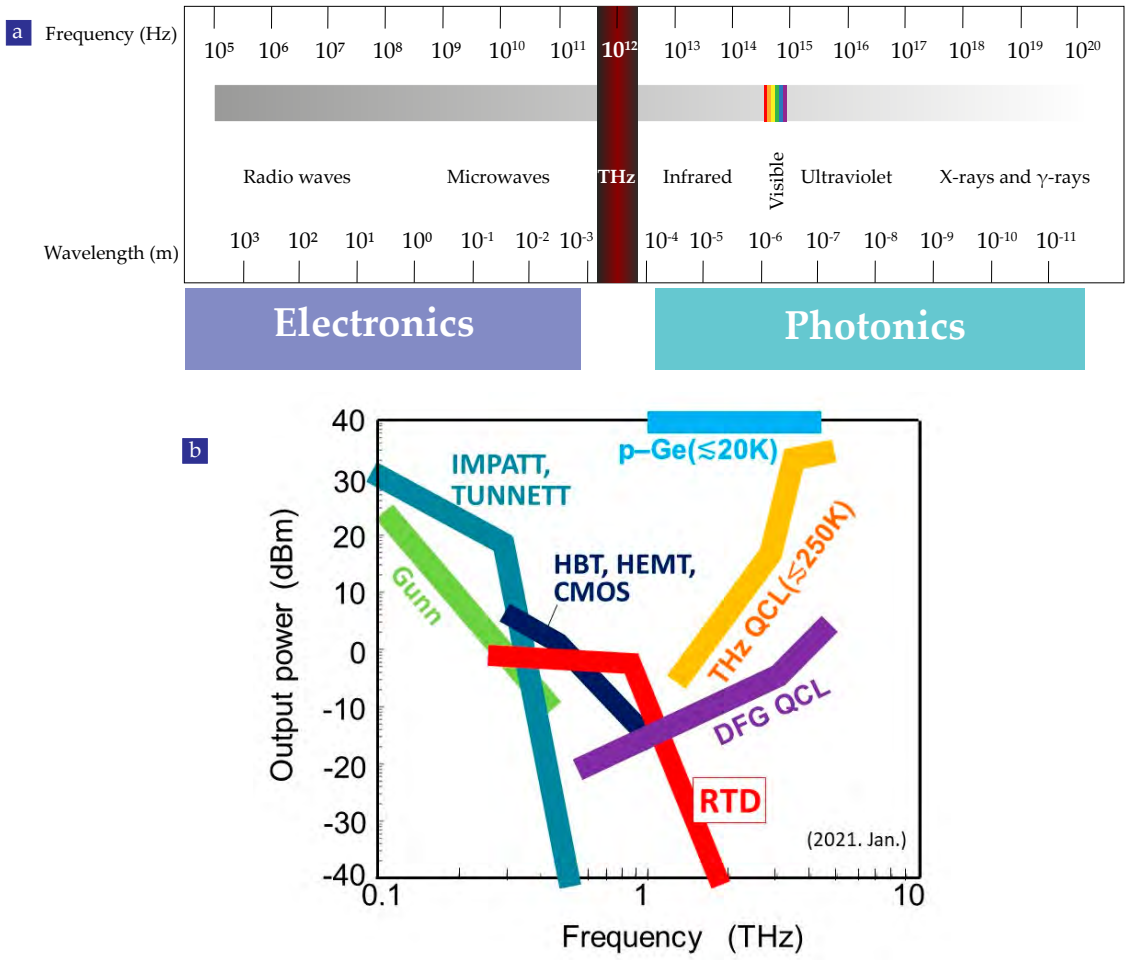

Figure 1.1 – *a) A schematic showing the* THz *range within the electromagnetic spectrum, and lying between Electronics and Photonics. b) Fig. b) is taken from* [6]. THz *emission power as a function of frequency: IMPATT diodes stand for impact ionization avalanche transit–time diode, TUNNET stands for tunnel injection transit time, HBT, HEMT and CMOS stand for Heterojunction Bipolar Transistor, High Electron Mobility Transistor and Complementary Metal Oxide Semi-conductor respectively, RTD stands for Resonant–Tunneling Diode, QCL stands for Quantum Cascade Laser and DFG stands for Difference Frequency Generation.*

An ideal THz source should be powerful ($> \mathrm{mW}$), highly–tunable, highly–coherent ($< 1\ \mathrm{kHz}$), compact (cm range), affordable ($< 1000\ €$) and it should work at room temperature (RT) and above ($\sim 300\ \mathrm{K}$). These values could be different depending on the targeted application.

1.1 Review of THz sources: challenges and applications

This section is subdivided into two parts, showing different approaches to generate THz waves. The former one coming from electronics technology and the latter one coming from photonic technology.

1.1.1 Electronic sources

Electronic sources are used for a wide spectral range, from sub–kHz to GHz–THz generation. The technology used for each application is usually specific, especially for higher frequencies.

For example, to generate GHz–THz waves, multiplication factor technique [44], i.e. non–linear devices capable to generate harmonics in the THz frequencies range, are typically used. Such systems employ a cascade of electronic multipliers in order to reach the frequency of interest. Another way to generate GHz–THz waves is direct emission from a diode. There is a large family of diodes. To cite a few of them as showed in Fig. 1.1b: Schottky diodes [45], Gunn diodes, IMPATT diodes, MITATT diodes, RTD diodes [6], TUNNETT, HEMT, GaN, and UTC [46]. With these diodes, high power (mW range) can be reached at few hundreds of GHz at room temperature. However, the diodes do not offer both high–tunability and coherence at the same time. Virginia Diodes Inc. is the world leader to commercialize Schottky–based diodes and frequency multiplication for THz generation and detection. They all operate at room temperature but, as mentioned above, they suffer of low tunability even if the power at the resonant frequency is in the mW range up to 900 GHz. In fact, to optimize the THz output power, the diodes are mounted with waveguide thus the tunability is limited. In addition, the modulation of these diodes is tricky as it can lead to a drop of the THz output power by a $\times 1000$ factor. The technological process of diodes for large distribution is still complex, expensive, and highly demanding in term of resources. Diodes–based THz sources are still expensive for mass–production. MMIC [47, 48] are also utilized for THz generation. They provide an average milliwatt–level output power up to 100 GHz that strongly drops at higher frequencies. CMOS–based THz devices, THz electronics integrated circuits and hybrid electronic–photonic systems deliver important functionality, such as programmable beam–forming, for future applications in communication, sensing and imaging [49–51].

1.1.2 Photonic sources

High–power THz sources are available such as p–Ge lasers, DFG and parametric but they are cumbersome and so extremely difficult to commercialize. THz-QCL is one of the most promising photonic THz sources [52–55]. VeCSELs sources are the focus of the chapter 2 and THz–QCLs are the focus of this subsection. Lasers are generally based on the process of stimulated emission between two electronic states (Fig 1.2a). The wavelength emitted is then inversely proportional to the transition energy between the two energy levels. However, there are very few materials capable of having gaps narrow enough to reach the wavelengths corresponding to mid–infrared ($10\ \mu$m) or far–infrared ($100\ \mu$m), especially among semiconductors. Moreover, the energy corresponding to 4 THz is of the order of 17 meV and that of the thermal agitation of an electronic gas is 25 meV at room temperature. Therefore population inversion and gain are not possible as conduction and valence bands are coupled by thermal agitation, however a solution has emerged since the invention of the QCLs by J. Faist et *al.* [56]. This laser involves using intersubband transitions instead of interband transitions (Fig 1.2b), typically used in semiconductor lasers. QCL are made up of a succession of semiconductor layers of nanometric thickness (quantum well) whose energy levels are quantified. The laser emission wavelength is not determined here by the gap of the semiconductor material but by quantum engineered energy bands so that the difference between two levels of the adjacent wells correspond to the energy of a THz photon. The QCL use intersubband transitions in a sequence of coupled quantum wells so that electrons descend the structure once polarized, emitting a photon at each elementary layer. The electrons then pass to the next quantum well by tunneling effect. However, although QCLs can achieve good optical and electrical performance, the fact that the energy of THz photons is

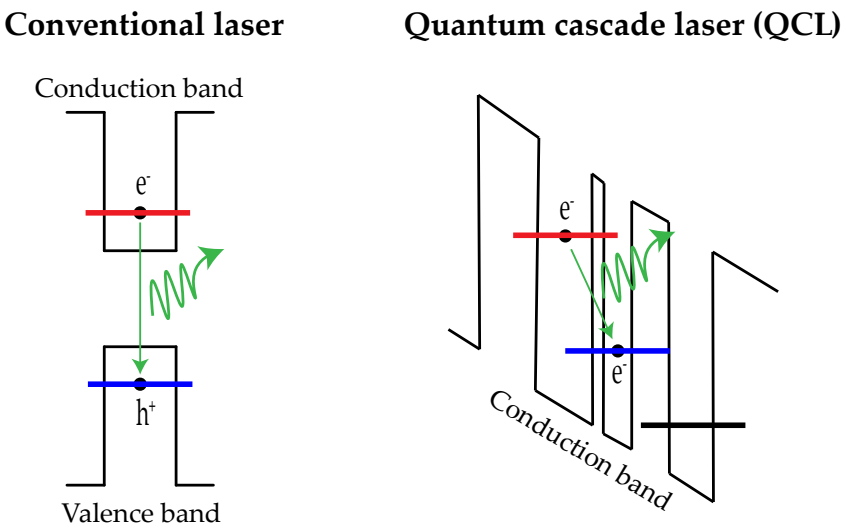

Figure 1.2 – *Comparison between conventional laser and quantum cascade laser: Left) In a conventional laser, electrons may occupy states in one of two energy bands: the valence band and the conduction band. The two energy bands are separated by an energy gap in which there are no permitted states available for electrons to occupy. A single photon is emitted when a high energy electron in the conduction band recombines with a hole in the valence band. The emission wavelength of a conventional laser is therefore determined by the band gap of the material used. Right) A QCL consists of a periodic series of thin layers of varying material composition forming a superlattice. By suitable design of these layer thickness it is possible to engineer a population inversion between two subbands in the system which is required to achieve laser emission. The wavelength emission of a QCL is independent of the energy band gap and therefore THz frequency range is more accessible.*

lower than thermal energy at room temperature requires operation at cryogenic temperatures to avoid filling the energy states thermally, which would annihilate the population inversion. The first THz–QCL was achieved by R. Köhler et *al.* [57] in 2001. Although the first THz–QCL operated only up to a maximum temperature of $T_{max} = 40$ K, improvements in active regions and waveguides have brought inaccessible performance: mW–level of CW power at cryogenic temperature, with T_{max} up to 250 K in pulsed mode (Fig. 1.3) [58–61]. The compactness of a THz–QCL is ideal for many applications. However, due to the size of a THz–QCL, [62–65] and the working temperature, it is difficult to tune. Recent progress on tunability of ~ 600 GHz of a THz–QCL using an external mirror with an excellent spatial coherence is achieved [66]. THz–QCL still remains competitive to other approaches of generating THz waves. Another important thing to note is that the QCL are not spatially and temporally highly coherent. This is due to the imperfect optical confinement and also, to the intersubband transitions which generate optical noise during cascading since there is no correlation (as in amplified stimulated emission) between generated photons. Despite the challenges of the THz–QCL to increase temperature operation, tunability and coherence at the same time, THz–QCL are scientifically and technologically rich to be used for spectroscopy, sensor, or communication. To enable mass–production, the first QCL on silicon was achieved [67]. THz–QCL combs [68, 69] working at room temperature [70] is considered as potential tool for spectroscopy and metrology of the third Millenium. QCL could be used for radio–communication [71] and recently for millimeter–wave photonics [72]. Finally, a QCL is also used to pump a molecular gas laser and generate mW–level output power at 1 THz at room temperature and in CW operation [73, 74].

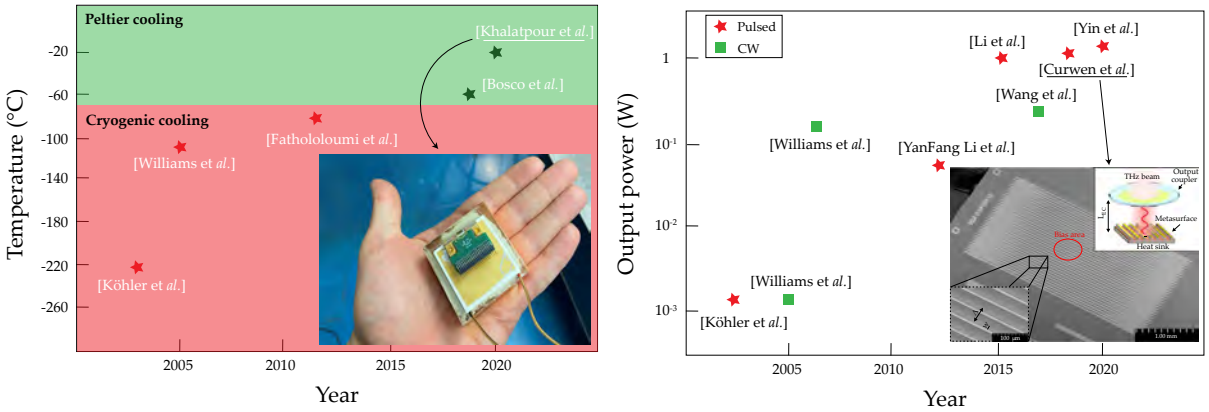

Figure 1.3 – *Roadmaps: Left) Roadmap of working temperature of* THz–QCL. *After the initial rapid increase of* THz–QCL, T_{max} *achieved during the period 2002–2005, progress slowed, eventually stalling in 2012 where the record remained at* -73 °C *until 2019, when* $T_{max} = -63$ °C *was achieved.* $T_{max} = -23$ °C *is achieved this year. The bottom right inset shows a portable terahertz laser system. Right) Evolution of* THz *power of* THz–QCL *in both CW and pulsed regimes. These results were obtained between* 3 THz *and* 5 THz, *at very low temperature* (-265 °C *typically*). *The bottom right inset shows a SEM image of* THz QC–VeCSEL *with a metasurface amplifier used to achieve watt–level output power around* 3.5 THz *at* -267 °C *in pulsed mode operation.*

1.2 Review of photomixing based THz sources

The photomixing techniques are widely used for THz generation [46]. THz waves are generated using a non–linear device excited by two independent lasers or by a dual–frequency laser. Therefore, thanks to the non–linearity of the device, several harmonics in the range of frequencies of interest can be generated. In the industry, photomixing technique is still the most used technique for commercial THz sources. Typically, commercial pulsed THz sources use a femtosecond laser and a photoconductive antenna (PCA) for THz generation and as seen above, it is used for spectroscopy, imaging and non destructive control. Although the photomixing technique is mainly used, the output power decreases sharply toward 1 THz frequencies range. A straightforward solution consists in using a plasmonic–based devices and/or an array of photomixers.

1.2.1 Principle

The photomixing is based on the detection of the beating of two laser beams by an ultra–fast device whose absorption wavelength is compatible with that of optical sources [46, 75]. The photomixer consists of a semiconductor (or crystal) component on which an optical beat is sent, generally obtained by the coupling of two waves of powers P_1 and P_2, of identical polarization and optical pulsations ω_1 and $\omega_2 = \omega_1 + \Omega$, where Ω is the targeted THz pulsation of emission, as shown in the Fig. 1.4. The modulation comes from the beating of two continuous laser sources. The absorption of the two waves creates carriers whose concentration oscillates at the frequency difference Ω of the two incident radiations. The (photo)detection process of the photomixer is typically quadratic, which means that the current or voltage response is proportional to the incident optical power. The frequencies sum and difference are generated and only the frequency components such that $\omega < 1/\tau$ will generate a modulation of the photocurrent, where τ is the photoconductor response time. The other components (such as those in ω_1, ω_2 and $\omega_1 + \omega_2$ and so forth) will be too fast for the detector (more than 600 THz for an excitation around 1 µm).

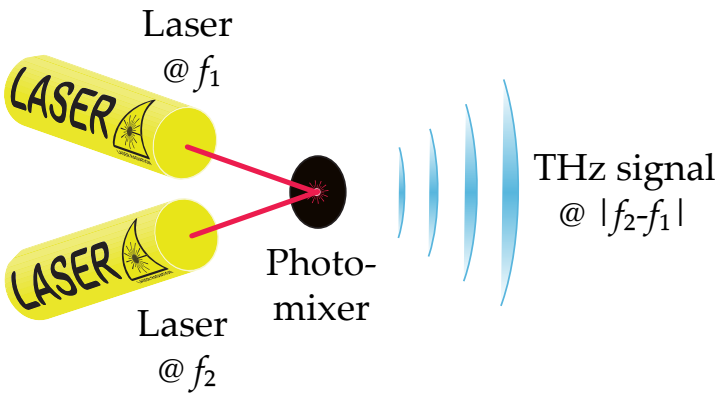

Figure 1.4 – *The beams of each laser* 1 *and* 2 *are mixed together and focused on a photomixer device which generates the terahertz radiation. High tunability (from* 300 GHz *to* 3 THz*) and high coherence (order of* MHz *maximum) could be achieved using this technique. A photomixer is a non–linear device and it could be a crystal, a photoconductor or a photodiode. They could be used in extra– or intra–cavity operation in both CW and pulsed regimes.*

At time t, the detected optical power is expressed as:

$$P(t) = P_1 + P_2 + 2\sqrt{P_1 P_2}\cos[(\omega_1 - \omega_2)t + (\Phi_1(t) - \Phi_2(t))] \tag{1.1}$$

where ϕ_1 and ϕ_2 are the initial phases. The photoconductor under illumination generates a photocurrent modulated at the frequency $f = (\omega_1 - \omega_2)/(2\pi)$. Controlling the optical frequency difference between the two lasers makes possible to tune the emission frequency of this type of source. In addition, it is easier to tune at THz with sources emitting at hundreds of THz. The THz generated power is proportional to the square root of the product of the powers of the two modes ($P_{beat} = 2\sqrt{P_1 P_2}$). The photomixing thus could make possible to obtain a coherent, compact THz source, tunable on a wide frequency band and operating at room temperature. The spectral purity of the beat is linked to the evolution of the relative phases $\Phi_1(t) - \Phi_2(t)$ and therefore, to the phase correlation between the two modes. The phase correlation between the two modes lead to the frequency stability of the THz sources. This illustrates the advantage of using a dual–frequency source rather than two independent sources, since a large part of the fluctuations are assumed to be identical (at first order) for the two laser modes thanks to the use of a common cavity and pumping systems. Thus, the effects of these variations cancel each other out and the beat frequency is stabilized. In addition, the coherence in term of polarization, spatially and spectrally is an important parameter here. Highly-coherent lasers permits to achieve pure and stable optical beat frequency. So, the THz signal will be stronger and more stable at a given frequency. Finally, the powers at each of the two wavelengths must be balanced to optimize the modulation depth.

1.2.2 Non–Linear Crystals

Non–linear crystals are used in many applications, including THz generation. To generate THz waves by difference frequency, monochromatic sources are utilized and to generate THz pulses by optical rectification, femtosecond lasers are used. Optical rectification can also be seen as a special case of generation by frequency difference when it occurs within the same laser beam. In the first case, the signals will be monochromatic with a spectral width of a few kHz. In the second case, the THz signals will be pulsed and therefore wide band, the spectral

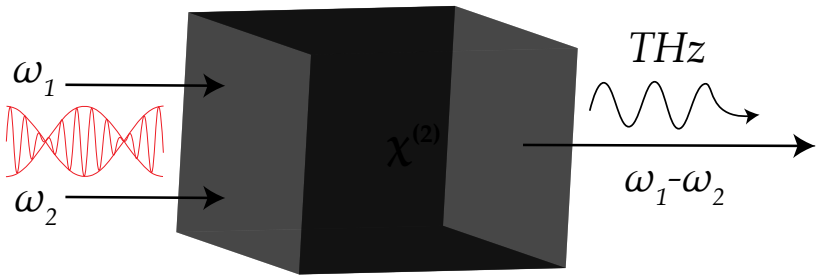

Figure 1.5 – *Two beams are mixed together into a non–linear crystal. This two–wave mixing process $\chi^{(2)}$ converts the two beams into a* THz *beam (Difference Frequency Generation). To achieve very high conversion efficiency high* THz *power and, phase–matching conditions are mandatory.*

width can reach several tens of THz.

A Pulsed regime

Non–linear crystals are mostly used in pulsed regime because the conversion efficiency is usually very low. Recent results at mW–level range are achieved in pulsed regime [76–91], mostly in intra–cavity. However, they are too cumbersome to be commercially available.

B Continuous–wave regime

THz waves are generated thanks to the frequency–difference generation between two incoming signals at different frequencies (Fig 1.5). It is a challenging task to solve the problem of phase–matching between these two inputs inside the crystal. The phase–matching means the ability of the crystal to generate constructive interference at high intensity at the frequency of interest. Another inconvenient of using non–linear crystals as photomixers is their limited tunability since typically the phase–matching condition is possible only in a narrow bandwidth. The second–order nonlinear effects appear in non–centrosymmetric crystals such as ZnTe, GaAs, GaSe or certain organic crystals (DAST). If the incident optical source has two frequency components ω_1 and ω_2, the generated beam has five of them: at frequencies quasi-zero (optical rectification), $2\omega_1$, $2\omega_2$ (frequency doubling), $\omega_1 + \omega_2$ (sum frequency) and $\omega_1 - \omega_2$ (difference frequency). For THz generation, only the frequency beating (difference frequency) are utilized. There are few works in CW [92, 93], as explained above, they suffer in terms of efficiency even if mW–level output power is already achieved. The tunability is also limited.

1.2.3 Photoconductive Antennas

Photoconductive antennas are devices consisting of two metallic contacts deposited on an intrinsic semiconductor substrate absorbing the incident optical beam, i.e. GaAs for a pump wavelength of 800 nm or InGaAs for 1064 nm and 1550 nm (the wavelength changes because the band gap can be changed as function of the Indium content). A voltage difference is applied to the electrodes but, when not illuminated, a weak current flow (due to high resistance) always exists inside the structure (Fig. 1.6). PCA can be utilized in both pulsed and CW regimes.

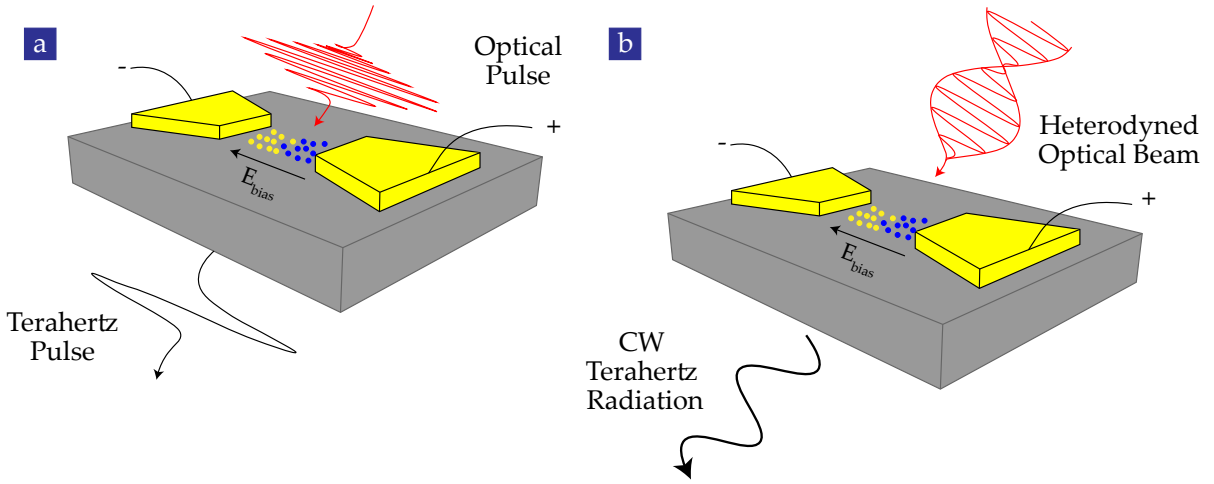

Figure 1.6 – *Operation principle of photoconductive terahertz antenna emitters and detectors. a) Schematic diagram of a photoconductive antenna for pulsed terahertz radiation generation. A femtosecond optical pulse is used to pump the photoconductive antenna and a bias voltage is applied through the antenna electrodes to drift the photogenerated carriers. b) Schematic diagram of a photoconductive antenna for CW terahertz radiation generation. A heterodyned optical beam is used to pump the photoconductive antenna and a bias voltage is applied through antenna electrodes to drift the photogenerated carriers* [94]. *Figures adapted from* [94].

A Pulsed regime

The illumination of the inter–electrode space of the device with an ultrashort laser pulse (Fig. 1.6a) will then create electron–hole pairs in the photoconductor material. The return to equilibrium occurs after a time τ which corresponds to the lifetime of the free carriers, if this is smaller than the transit time between the electrodes. Otherwise, the rapid variation of the carrier density, typically on the order of picoseconds, and their acceleration by the electric field results in a current transient. This temporal variation of the current will lead, in the same way as the Hertz experiment, to emission of electromagnetic waves in the THz frequency range. This principle was first applied at THz frequencies by Brown [95] using two Ti:Sa lasers associated with a photomixer consisting of a spiral broadband antenna and a low–temperature epitaxial GaAs photoconductor (LT–GaAs). The very short lifetime τ_{rec} of the photocreated carriers in this material is due to the recombination mechanism by deep donors intentionally introduced in high concentration. This very short lifetime is needed so that the bandwidth of the PCA will reach the THz frequencies range. This material was obtained by changing the deposition conditions, including lowering the crossing temperature to 200 °C and optimizing the annealing temperature. Since then, new materials have been studied such as ErAs:GaAs [96], InGaAs epitaxial on GaAs [97] or GaAsSb epitaxial at low temperature [98]. It is also possible to create defects by implantation and ion irradiation in materials such as $In_{0.53}Ga_{0.47}As$ [99]. Thus, the transit time of the electrons within the active zone does not limit the bandwidth of the component and the spectral range of the generated signals can reach 30 THz. As for other photomixers, the bandwidth also depends on the RC cutoff frequency related to the geometry of the photoconductor space. The conversion efficiency (or photoconduction gain) depends on the ratio between the carrier lifetime and the transit time to the electrodes via the carrier mobility. A trade–off between carrier lifetime and mobility must be found to reach THz frequencies with the highest possible power. A lot of research has been done in order to find the material with the best compromise. Another way is to work on the geometry of the electrodes by reducing the average path length of the carriers to the electrodes. Considering the drift velocity of

the carriers of most photoconductors, a path length of less than $100\ \mathrm{nm}$ is necessary to obtain a transit time of the order of a picosecond. However, reducing the inter–electrode length means reducing the surface area that can be illuminated and therefore reducing the optical power that can be absorbed by the photoconductor. Knowing that focusing the pump optical beam below a certain size is limited by diffraction and that the maximum optical intensity is limited for thermal heating, structures with a large surface equipped with interdigitated electrodes or plasmonic electrodes [94, 100] have been developed to obtain both an efficient optical coupling and a good conversion efficiency. S.H. Yang *et al.* recently demonstrated the highest optical–to–terahertz conversion efficiency (7.5%) using three–dimensional plasmonic contact electrodes [101] in pulsed regime. Finally, 2D materials–based photoconductors are promising devices for THz generation [102].

B Continuous–wave regime

The same principle applies to PCA working in CW operation, except the use of optical sources. The optical sources used in CW are usually two independent lasers or dual–frequency lasers (Fig. 1.6b). Most research results in CW have been demonstrated by using optical sources operating at $800\ \mathrm{nm}$ or $1550\ \mathrm{nm}$, except the work of Czarny R. *et al.* [97] with their lasers operating at $1064\ \mathrm{nm}$. Since the work of Gregory [75, 103], many tentative to push forward the THz power in CW were done only by a few research groups. mW–level powers have been obtained using plasmonic electrodes devices at $440\ \mathrm{GHz}$ using dual-frequency DFB lasers [104] operating at $1550\ \mathrm{nm}$. mW–level output power is achieved using Fabry–Perot photoconductors (without antennas)[105, 106] using optical sources operating at $1550\ \mathrm{nm}$. These photoconductors present a higher efficiency at $1550\ \mathrm{nm}$ despite the use of a LT-GaAs bulk and an antenna could be fabricated for THz emission in free-space.

Novel materials are required in order to increase the optical–to–terahertz efficiency and thus the THz output power. Currently, plasmonic–based photoconductive antennas provide the best performance in term of THz power. Improvements depends also to the last trends and techniques of nanotechnology fabrication, which they can significantly improve the efficiency. Also, the extension as well as new growing techniques (especially with 2D materials) could better improve the THz power.

1.2.4 Uni–Travelling–Carrier Photodiodes

High–speed telecommunications by optical fibers (typically for a wavelength of $1550\ \mathrm{nm}$) are at the origin of the rise in frequency of photodiodes where the PIN structure is commonly used as a photodetector [107–115]. This one consists in the junction of semiconductor layers of different thickness and doping, illuminated perpendicularly by the optical beam. Unlike photoconductors, the bandwidth of the detector is not based on the lifetime but on the transit time of the carriers through the active zone before being collected (depletion zone or intrinsic zone in the case of PIN). These photodiodes are limited in frequency by the capacity C of the junction and the thickness d of the active zone. This capacity is inversely proportional to the thickness of the active zone and directly proportional to the detection surface S according to the formula $C = \frac{\epsilon_0 \epsilon_r S}{d}$. A compromise is necessary between a very fast collection of the carriers via a decrease of the thickness d of the active zone and the RC time constant. The reduction of the

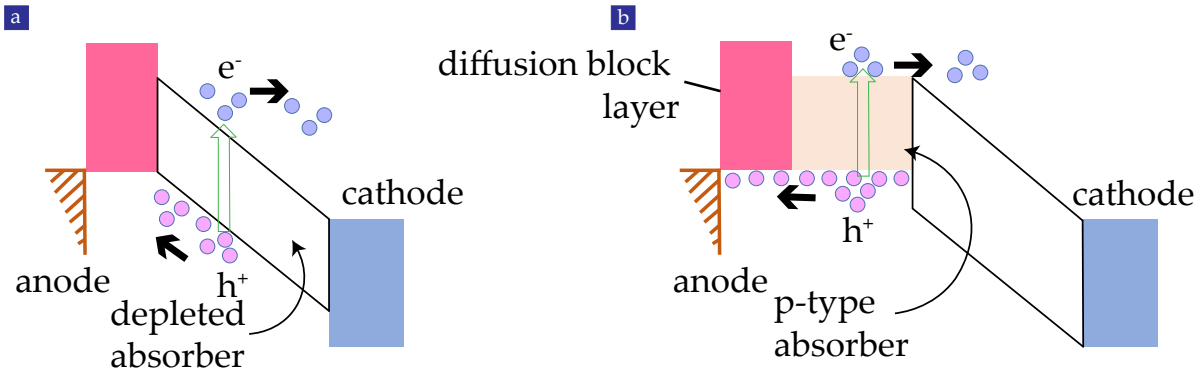

Figure 1.7 – *Band diagram of a) PIN–PD and b) UTC–PD* ***a*** *P–type layer, intrinsic layer and n–type are sandwiched to form two junctions NI junction and PI junction. When a reverse bias voltage is applied, the depletion increases. With a large surface area, higher conversion efficiency and higher photocurrent can be obtained. Thus, higher* THz *output power can be achieved.* ***b*** *UTC–PD. An extended version of a PIN–PD where electron current is dominant in operations. Figures adapted from* [108].

depleted area will however lead to a reduction of the number of absorbed photons and thus a lower conversion efficiency as well as a degradation of the cut–off frequency of the equivalent RC circuit. Another way is to reduce the detection area, but it is now the maximum optical intensity that will limit the power emitted for thermal heating reasons. Moreover, it is not desirable to reduce it below a certain size, of the order of the wavelength of the optical beam, since the focusing will be limited by diffraction. To overcome the dynamic behavior of the slowest carriers, a new photodiode structure has been developed, notably by the NTT laboratories in Japan for the first time [107]. Known as UTC (Fig. 1.7), they are based on the dissociation of the absorption zone from the intrinsic zone, which are confused in PIN photodiodes, so that the speed of the holes, weaker than that of the electrons, does not limit the speed of the photodetector. During the absorption of the photons in the semiconductor, the electron–hole pairs are generated in a doped zone of the p–type, which allows the excess holes to be evacuated quickly towards the contact with a time constant equal to the dielectric relaxation time of the material. The electric field being very weak in the absorbing zone (GaInAs), the electrons move by diffusion to an intrinsic or weakly doped zone called collector (InP) in which the electrons are accelerated under the effect of the electric field. A potential barrier (GaInAsP) is placed against the absorbing region to prevent diffusion from the unwanted side. Thus, it is primarily the electrons that determine the response time in the structure since the dielectric relaxation time of the holes is very short compared to the transit time associated with the electrons. This response time is related to the transit time by diffusion in the absorption layer τ_A and to the transit time τ_C by drift in the collector, the total transit time is estimated as:

$$\tau_t = \tau_A + \tau_C = \frac{W_A^2}{3D_e} + \frac{W_C}{v_e} \tag{1.2}$$

where W_A and W_C are the thicknesses of the absorbing zone and the collector, D_e is the electron diffusion coefficient and v_e is the speed of electrons in the collector. The diffusion is considered only in one spatial dimension (along the device). This is the reason of the factor 3. Under the right bias conditions, the electron velocity in the collector can exceed its saturation value at high field according to a non–stationary transport phenomenon called velocity overshoot, which makes the UTC structure even faster than the PIN structure with a maximum electron

velocity in InP eight times higher than the hole saturation velocity in InGaAs. The advantage of dissociating the absorbing region of the collector is that each of the thicknesses can be adjusted independently, which allows the transit time to be reduced without impacting the RC time constant. Moreover, due to the high electron velocity, the saturation phenomenon occurs for current densities that are one order of magnitude higher for the UTC structure compared to the PIN. This phenomenon is encountered when the density of photogenerated carriers increases significantly, an accumulation of carriers takes place, causing a local weakening of the electric field. This decrease in the field will reduce the velocity of the carriers and the photocurrent no longer increases with the optical power: the photodiode saturates. This effect is accentuated for the slowest carriers like holes.

A Pulsed regime

The first UTC-PDs were firstly characterized using pulsed laser or CW modulated lasers [107, 116]. This was to demonstrate the higher performance in the terms of cut–off frequency compared to PIN-PD. But today, there is lower interest working on this approach as UTC is improving quickly reaching mW–level at $300\ \mathrm{GHz}$ in CW and it is now sufficiently mature to fabricate and test novel approaches in CW directly.

B Continuous–wave regime

Powers of $300\ \mu\mathrm{W}$ at $300\ \mathrm{GHz}$ and $2.6\ \mu\mathrm{W}$ at $1\ \mathrm{THz}$ with the UTC structure are achieved [117]. Only a few research group are capable to fabricate efficient UTCs [22]. They are mostly excited at telecom wavelength $(1550\ \mathrm{nm})$. No UTC designed at $1064\ \mathrm{nm}$ and/or excited by $1064\ \mathrm{nm}$ lasers is reported except in this work [118] where a commercial UTC designed at $1550\ \mathrm{nm}$ is excited by a $1064\ \mathrm{nm}$. In this case, the THz power extraction is less efficient but a power of $1\ \mu\mathrm{W}$ at around $300\ \mathrm{GHz}$ was achieved.

Today, the research work is focused on the thermal dissipation and the efficiency of the antenna, which will allow to increase the performances and to make accessible powers of the order of $> 10\ \mathrm{mW}$ at $300\ \mathrm{GHz}$ (achievable with an array of UTC, if a single UTC provides more that $1\ \mathrm{mW}$) and at room temperature.

1.3 Summary

The realization of compact THz sources based on photomixing is an advantageous solution to reach the THz domain. A coherent and tunable THz emission at room temperature is obtained. However, the low conversion efficiencies remain an obstacle to the emission of power higher than about $10\ \mu\mathrm{W}$ beyond $1\ \mathrm{THz}$. The emitted power is limited by the sensitivity of the photomixer and the maximum intensity that can be focused on it. Improving thermal dissipation and mitigating space charge effects will help pushing the saturation limits of photomixers. Other techniques are developed to circumvent the power problem such as the use of photomixer arrays or intracavity generation with large surface area photoconductive antennas with plasmonic electrodes or a nonlinear crystal. Furthermore, coherent THz generation by photomixing requires the use of a single laser source emitting two correlated frequencies. THz photomixers were mostly excited by $800\ \mathrm{nm}$ and $1550\ \mathrm{nm}$ optical sources despite the availability of optical

sources operating at $1064\ \mathrm{nm}$. Only a very few works were done at $1064\ \mathrm{nm}$ in CW regime but with uncertainty of the estimated THz output power since a bolometer were used. In the next chapters, DF–VeCSEL, which is proved to be a great candidate for photomixing (highly coherent, highly tunable and stable), combined with a photomixer designed at $1064\ \mathrm{nm}$ and in CW regime is demonstrated.

Chapter 2

Continuous–Wave Dual–Frequency VeCSEL for THz Generation

2.1 Fundamentals of Lasers

2.1.1 Introduction

Lasers are devices that generate or amplify coherent radiation at frequencies in the infrared, visible, or ultraviolet regions of the electromagnetic spectrum as seen in the Fig. 1.1 of the previous chapter. Practical laser devices employ an extraordinary variety of materials, pumping methods, and find a great variety of applications. Since the first appearance of coherent light 60 years ago [119], a large variety of lasers is now available. Recently an increased interest for structured light, that could be useful for applications in communication has emerged. Structured light could also be used for optical tweezers (especially using orbital angular momentum (OAM) based sources [3, 120]), metrology, quantum communication and many other applications [121]. The key elements of a laser device are [122–124]:

— a ***laser medium*** consisting of an appropriate collection of atoms, molecules, ions or a semiconducting crystal.

— a ***pumping process*** to excite these collection into higher quantum energy levels and

— suitable ***optical cavity*** (or optical feedback) elements that allow a beam to roundtrip several times and achieve transition.

The attractive properties of a laser radiation are the following:

— **Coherence.** Spatially and temporally and in terms of polarization. M^2 at limit diffraction, with high Side–mode Suppression Ratio (SMSR) > 50 dB means high–quality operation lasers and high polarization extinction ratio (PER) are the principal goals.

— **Power.** Powerful lasers working at room temperature are needed for many application such as spectroscopy, lidar, communication and many others.

— **Tunability.** A highly–tunable laser is useful for applications such as communication and spectroscopy.

An ideal laser (needed for THz source using photomixer) must be sufficiently powerful (> 100 mW), highly–tunable (> 5 THz), highly–coherent spatially ($M^2 < 1.2$) and temporally (FWHM < 1 kHz) with a high PER, compact (cm range), affordable and it should work at room temperature and above (~ 300 K). A powerful, highly–tunable, and highly–coherent light source is achieved only by few lasers including VeCSELs [125, 126].

The performance of the laser–driven THz sources depends strongly on the quality of the laser source. In others words, all these properties of an ideal laser can be transposed to the ideal THz source. The work shown in this chapter was done in close collaboration with C2N CNRS RENATECH technology center for the development of advanced semiconductor components with III-V nanostructures. High–performance lasers mainly depend on passive cavity design and amplifier medium, described in the following sections.

2.1.2 Passive cavity

A Longitudinal modes

The phase shift ϕ in a cavity after one roundtrip must satisfy the condition: $\phi = q2\pi$ where q is an integer representing the longitudinal mode order. The resonator creates strong wavelength discrimination and allows only a set of discrete and periodic longitudinal modes to exist whose spectral periodicity is the free spectral range *FSR* generally expressed as [1, 122]:

$$FSR = \frac{c}{2nL_c} = \frac{1}{\tau} \tag{2.1}$$

with n the refractive index of the medium, L_c the length of the cavity, τ the roundtrip time in the cavity. The losses ($Loss$) per roundtrip in the cavity produce a broadening of the resonance peaks linewidth, whose *FWHM* width is given by [1, 122]:

$$2\pi\delta\nu_c = \frac{w_0}{Q} = FSR \times Loss = \frac{2\pi FSR}{F} \tag{2.2}$$

where Q is the described quality factor of the cavity, w_0 angular frequency, and F is the finesse which characterizes the number of roundtrip in the cavity. In order to obtain a single–frequency operation for each modes, the passive cavity must have a very high quality factor ($Q = \nu/\delta\nu_c$). As an example, in a Fabry–Perot cavity of length $L_c = 10$ mm filled with air and losses $Loss \sim 1\%$ which is mainly determined by the cavity reflection factor, the photon lifetime is $\tau_{ph} \simeq 6.6 \times 10^{-9}$ s, the FSR is 15 GHz and the Finesse is $\simeq$ 600. Fig. 2.1 shows the electric field of the fundamental mode as well as the higher order modes. In addition, intensity as function of frequency is shown in Fig. 2.1 where FSR is frequency difference between adjacent longitudinal modes, $\Delta\nu$ is the FMHW of the longitudinal modes.

B Transverse modes

In a plano–concave configuration, the optical resonator consists of plane mirror and a spherical mirror of radius of curvature R_c, placed at a distance L_c closing the optical cavity. The condition for the cavity to be stable is that the radius of curvature of the beam match with the mirrors. The radius of curvature of the wavefront $R(z)$ of the beam must therefore be infinite

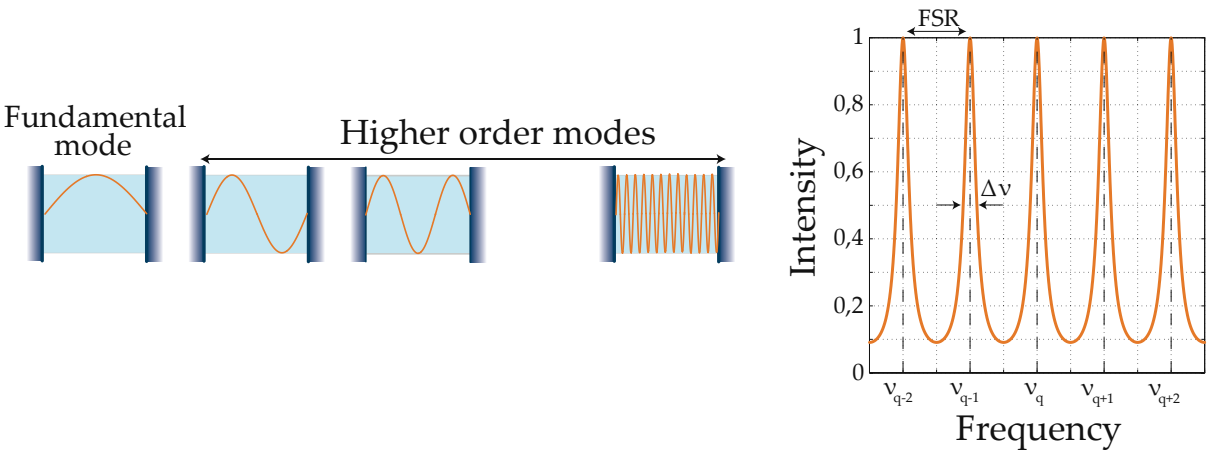

Figure 2.1 – *Illustration of longitudinal modes that might exist in a cavity. Left) Longitudinal modes ranging from fundamental mode to high–order modes. Right) A plot of (transmitted) intensity as function of frequency FSR* [127].

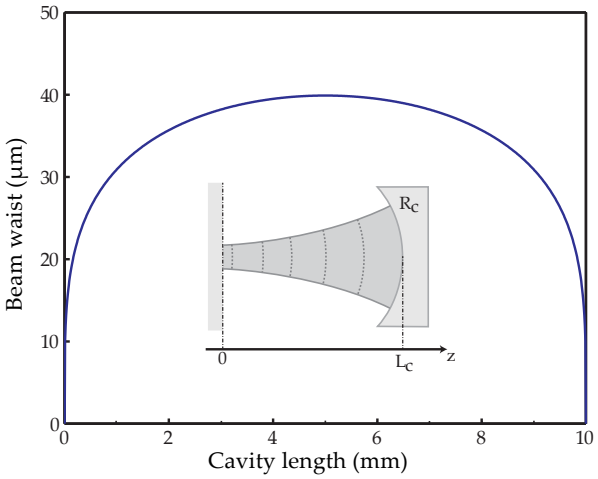

Figure 2.2 – *Evolution of the beam waist (radius at* $1/e^2$ *in intensity) on the plane mirror (near field) as a function of the cavity length for a radius of curvature of the external mirror of* $10\ \mathrm{mm}$ *and for a wavelength of* $1\ \mu\mathrm{m}$*. Inset: Schematic of a resonant cavity formed by a plane mirror and a spherical mirror, the dotted lines represent the equiphase surfaces* [2].

on the plane mirror ($z = 0$) and equal to R_c on the concave mirror ($z = L_c$). Many transverse modes can exist inside the cavity such as Laguerre–Gauss, Bessel–Gauss and Hermite–Gauss transverse modes. As fundamental Gaussian transverse mode is concerned, the waist of the stabilized laser mode on the plane mirror as a function of the cavity parameters is obtained as follow [122]:

$$\omega_0 = \sqrt{\frac{\lambda}{\pi}\sqrt{L_c(R_c - L_c)}} \tag{2.3}$$

The evolution of ω_0 as a function of the cavity length is presented in Fig. 2.2 for a radius of curvature of the external mirror of $10\ \mathrm{mm}$ and for a wavelength of $1\ \mu\mathrm{m}$. The stability is ensured if and only if $L_c < R_c$ even if the extreme edge of stability is to be avoided because it can be more sensitive to mechanical and thermal instabilities.

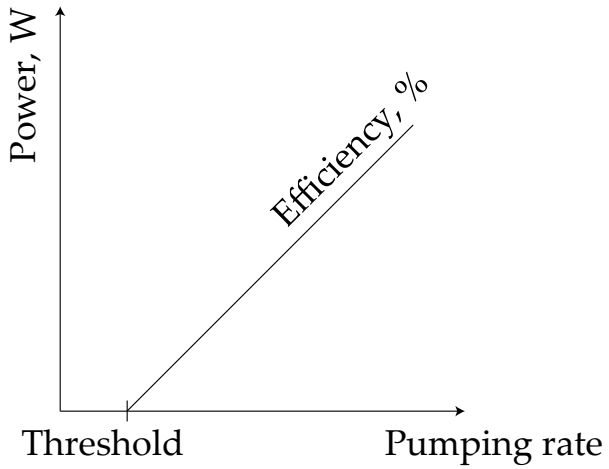

Figure 2.3 – *An example of typical laser characterization: power (expressed in Watt) as function of pumping rate.*

2.1.3 Active cavity

The laser is an active device and the lasing effect is only possible when the gain of the active medium inside the cavity compensate the losses inside the cavity. The energy given to the active medium is by optical pumping (among other ways to pump an active medium).

A Gain medium: static regime

The overlap of the laser mode with the Gaussian intensity distribution of the pump diode must also be considered. It plays a role in the transverse confinement factor of the modal gain which must be high enough to reach the laser threshold. As seen in the Fig. 2.3, the laser threshold is achieved when the gain compensates the loss. In other words, the laser threshold is obtained when all the losses of the cavity are equal to the gain provided by the gain medium via amplification. To achieve a low threshold then the passive cavity losses must be low as possible.

B Gain medium: dynamic regime

The laser medium has a homogeneous broadening gain when the response of each individual atom in the collection is equally and homogeneously broadened. In this regime of strong modal competition, only the mode with the higher gain will win and suppress all the others mode (Fig. 2.4). With this approach, a single–frequency lasers can be generated. Whereas if the laser medium has an inhomogeneous broadening it means that different collections of atoms may contribute independently to the gain of each longitudinal mode and this could lead to a multi–frequency lasers (Fig. 2.4) [122]. A VeCSEL in general has a homogeneous gain, so the high coherence is well–maintained and a single–frequency operation is guaranteed.

2.1.4 Polarization state

The polarization state corresponds to the geometrical spatial orientation of the electromagnetic field (macroscopic definition) and defined by the photon spin (quantum definition). There exist three polarization states: linear, circular, and elliptical. Controlling the polarization is necessary to obtain optimal performances. In fact, optical components and systems characteristics

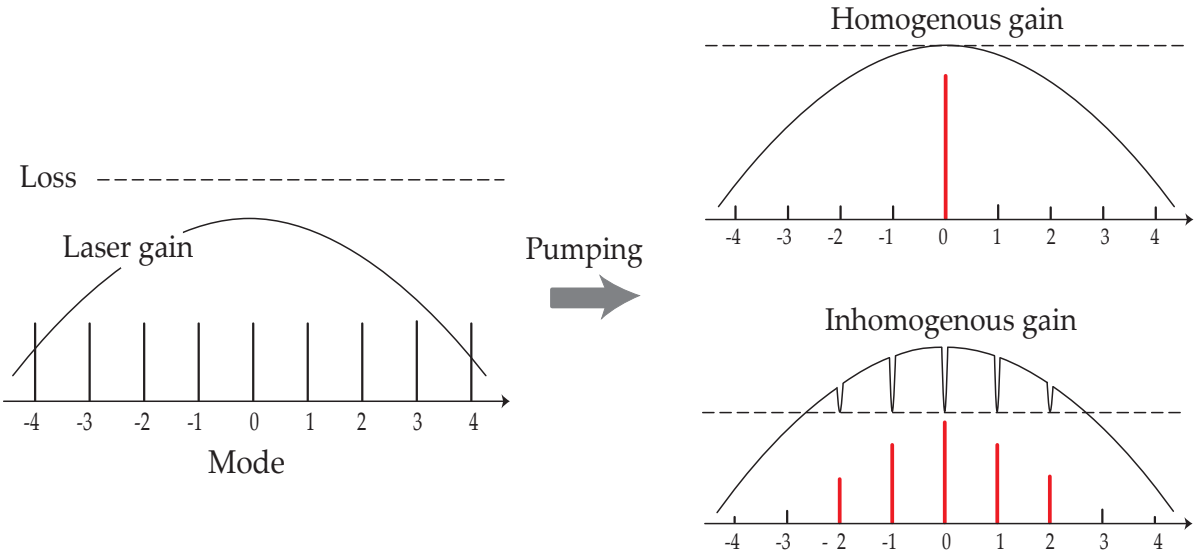

Figure 2.4 – *Schematic representation of the evolution of the laser spectrum in the case of homogeneous and inhomogeneous gain expansion. In the first case, the gain profile cannot exceed the threshold set by the first oscillating mode, leading to a single mode operation. In the second case, the gain profile continues to grow, it is saturated independently on each oscillating mode (spatial and/or spectral hole burning) [2, 128].*

such as reflectivity, insertion loss, and beamsplitter ratios will be different for different polarization. In most cases, the output of a laser is linearly polarized. Different mechanisms are responsible for linearly polarized emission of laser such as laser gain (anisotropic materials) or the resonator losses (when a Brewster plate is used or slightly tilted optical component). So, the polarization of a laser, which is define quantified by PER, is an important parameter for essentially two reasons: to avoid laser instabilities due to polarization switches and to achieve high coherent single–frequency lasers. In practice, the polarization of a laser is measured by using a polarizer and by applying Malus's law.

2.2 Vertical External–Cavity Surface–Emitting Lasers

2.2.1 Why VeCSEL?

VeCSELs technology combine the advantages of solid state lasers in terms of spatial beam quality and optical power with the wavelength flexibility and compactness of semiconductor lasers. The transverse modes of the laser are not guided, and their size is fixed primarily by the cavity. Thus, by adapting the size of the TEM_{00} fundamental mode to the pumping diameter, it is possible to guarantee a laser operation in this mode even for pumping sizes of up to a few hundred μm^2, which is necessary for a high–power emission (> 100 mW). The high finesse cavity (> 300) associated with a greatly reduced amplified spontaneous emission makes possible to reach a sub–MHz laser linewidth [134]. The wavelength of the laser is determined, at first order, by the cavity which allows a large tunability (840 GHz) [135] by adjusting the length of the cavity with a piezo–electric element, as seen in the Fig. **??**. This is a great advantage over monolithic VCSELs where the gain medium and the cavity are strongly coupled. In fact, in a VeCSEL, the length of the cavity and the position of the maximum of the gain can be tuned quasi–independently to adjust the position of the same longitudinal mode with respect to the maximum of the gain curve, for example by combining the effects of a piezo–electric element

and that of temperature. The state of polarization of the VeCSEL is linear thanks to the gain dichroism and the birefringence naturally present in the $1/2$–VCSEL chips. In addition, and thanks to the high finesse cavity, this state is very stable with strong rejection of the low polarization state (80 dB [3]). The external cavity also offers flexibility: the insertion of intra–cavity elements to achieve selection of a unique longitudinal mode or to introduce other functionalities such as the generation of sub–picosecond pulses with a saturable absorber [136], or frequency doubling with a non–linear crystal for IR/THz generation. With all of these mentioned features (coherence, tunability, power, polarization, flexibility), VeCSEL is considered as an excellent photonic solution for laser–driven THz sources.

2.2.2 Fundamental bricks of a VeCSEL

The building blocks of a VeCSEL laser are showed in the Fig. **??**. There are 4 main blocks:

1. **Distributed Bragg Reflector.** First mirror of the cavity. This mirror should have the highest reflectivity in order to reduce the cavity loss.
2. **Quantum wells.** The active medium of the VeCSEL. 6 QWs is often used for laser performance tests. Once the concept is solid, 12 QWs is often used in order to provide high–power.
3. **Anti–reflection coating or additional Bragg reflector.** As mentioned above, the anti–reflection suppress the micro–cavity effect or the additional Bragg reflector reinforces it.
4. **Masks.** Unconventional light can be achieved by using flat photonics technology and without intra–cavity optical elements.
5. **Concave (dielectric) mirror.** Second mirror of the cavity. T_{oc} of 1%, 10% and 20% are typically used to experimentally study the VeCSEL. A piezo-element can be attached to the mirror, so the cavity length can be tuned.

A Distributed Bragg Reflector

In the VeCSEL configuration, the length of the active medium is very small and is equal to the thickness of the quantum wells, i.e. a few tens of nm. Consequently, the gain per pass is relatively low (often less than $2\ \%$) and must be compensated by cavity mirrors of very high reflectivity ($> 99.9\ \%$) to reach the laser threshold. Such high reflectivity can only be achieved by Bragg mirrors. Bragg mirrors are composed of a periodic succession of semiconductor or dielectric layers of different refractive indices and optical thickness equal to $\lambda_B/4$, where λ_B is the wavelength for which maximum reflectivity is achieved. The constructive interference in this multilayer system allows to obtain an ultra–high reflectivity on a spectral band called stop band. The principle of this interference system is illustrated in Fig. 2.5. In a standard $1/2$–VCSEL structure, this mirror is realized with semiconductor materials, which makes possible to realize the complete structure by epitaxy. The reflection coefficient R and the width of the stop band $\Delta\lambda_B$ of a Bragg mirror can be expressed as a function of the refractive index difference $\Delta_n = n_H - n_L$ of the materials and the number of pairs N_p of successive bilayers. Assuming the materials to be transparent and lossless, at normal incidence R_{max} and $\Delta\lambda_B$ are given by:

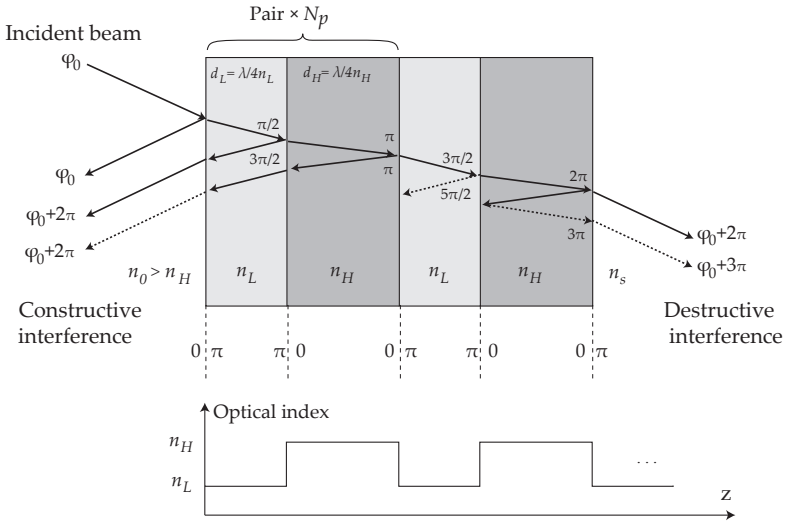

Figure 2.5 – *Schematic representation of the principle of a Bragg mirror* [2].

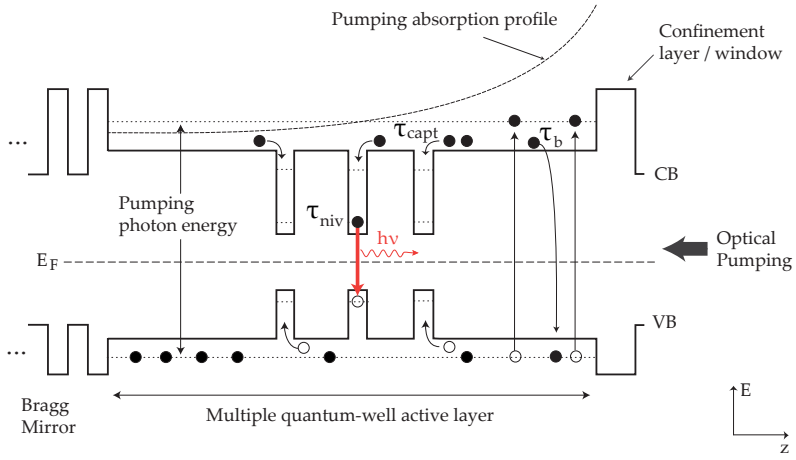

Figure 2.6 – *Schematic description of a* $1/2$*–VCSEL structure with multiple quantum wells under optical pumping. The solid circles represent the states occupied by the electrons and the empty circles represent the free states* [2].

$$R_{max} = \left(\frac{1 - \frac{n_s}{n_0}\left(\frac{n_L}{n_H}\right)^{2N_p}}{1 + \frac{n_L}{n_0}\left(\frac{n_L}{n_L}\right)^{2N_p}} \right)^2 \qquad \text{and} \qquad \Delta\lambda_B = \frac{2\lambda_B \Delta_n}{\pi n_{eff}} \tag{2.4}$$

Thus, depending on the number N_p of bilayers and the indices n_L and n_H, reflection rates R close to 1 can be obtained. For the realization of the $1/2$–VCSEL, it is necessary to choose materials with high index contrast and low optical losses by absorption (energy gap $>$ $h\nu$), thus semiconductor materials in AlAs/GaAs for the epitaxial structures on GaAs are used. With these materials, a reflectivity of more than 99.9 % can be achieved with 25 pairs and a stop bandwidth $\Delta\lambda_B \simeq 100$ nm to $= 1$ µm, much larger than the optical gain width g, which allows tuning the lasing wavelength over a wide spectral range.

B Laser gain: quantum wells and optical pumping

The active medium here is made of InGaAs/GaAs quantum well semiconductor materials emitting at 1 µm. A quantum well is composed of two different gap semiconductor materials: a small gap (InGaAs) surrounded by a larger gap (GaAs), as shown in Fig 2.6. Increasing the

electron population in a well by absorbing an optical pump beam will allow to provide gain. To evaluate the evolution of the gain with respect to the pumping level, one can express the maximum of the gain spectrum g as a function of the excited carrier density N [2] using the following expression [124]:

$$g(N) = g_0 \ln\left(\frac{N}{N_{tr}}\right) \tag{2.5}$$

where g_0 is a fitting parameter, N and N_{tr} are respectively the carrier density and the carrier density at transparency. g is expressed in cm^{-1} or in $\%$ if the thickness of the amplifying medium is considered. For an InGaAs/GaAs well, g_0 is typically $2100\ cm^{-1}$ and $N_{tr} \simeq 1.2 \times 10^{12} cm^{-2}$ [124]. The gain of an InGaAs/GaAs quantum well thus reaches a maximum value of $5000\ cm^{-1}$ or 0.5 $\%$ per pass along the quantization axis. This value is not sufficient to ensure an efficient laser operation in vertical configuration, especially at the threshold. In order to increase the maximum gain of the active medium, a structure with multiple quantum wells is used to reach a gain of several $\%$. A gain of 2%-3% is a typical value, which compensates for internal losses (~ 0.1 – $0.5\ \%$), Bragg mirror losses ($\sim 0.1\ \%$), and output mirror losses ($\sim 1\ \%$). The latter must be the dominant losses to ensure good performance.

The excitation of the carriers takes place directly in the active region of the $1/2$–VCSEL, via the absorption of a pump beam in the quantum well barriers. The longitudinal absorption profile is given by the Beer–Lambert relation:

$$A_b = 1 - \exp(-\alpha_p L) \tag{2.6}$$

where A_b is the fraction of absorbed photon, L is the length of the absorbing path, and λ_p is the linear (effective global) absorption coefficient of the barriers at the pump wavelength λ_p. The length of the active region will thus depend on the absorption coefficient of the barriers at the pump wavelength and the number of wells used. For a structure with GaAs barriers, a $7\lambda_0/2$ length is required to absorb more than $85\ \%$ of the incident pump power and to place all the wells on the antinodes. 6-QWs are typically used to achieve lasing and are located on optical standing–wave antinodes. In the case of a structure with SiN deposition on its surface, the anti–reflection treatment is still effective at the pump wavelength ($\sim\ 785\ \mathrm{nm}$), allowing almost all of the pump power to be transmitted into the active area. In the case of a resonant filter structure, AlGaAs/AlAs pairs are used. Fig. 2.7 illustrates the optical pumping process in a $1/2$–VCSEL structure. The photo–generated carriers in the barriers are confined in the active area by a confinement layer on one side and by the Bragg mirror on the other. These confinement barriers prevent the carriers from recombining on the surface or in the Bragg mirror. The absorption profile will also influence the distribution of the quantum wells along the active area. In order for the gain to be homogeneous for each quantum well, the quantum wells must be distributed so that the carrier density is the same in all wells. Given the small thickness of a quantum well relative to the wavelength, it is possible to place multiple wells on the same maximum of the standing wave. However, to avoid any electronic coupling effects, the wells must be spaced sufficiently far apart ($\sim\ 20\ \mathrm{nm}$), which limits the number of wells per field maximum ($\sim\ 3$). Beyond that, the modal gain at working wavelength λ_0 is reduced due to spectral filtering. Therefore, when the structure has a large number of wells, they should be distributed

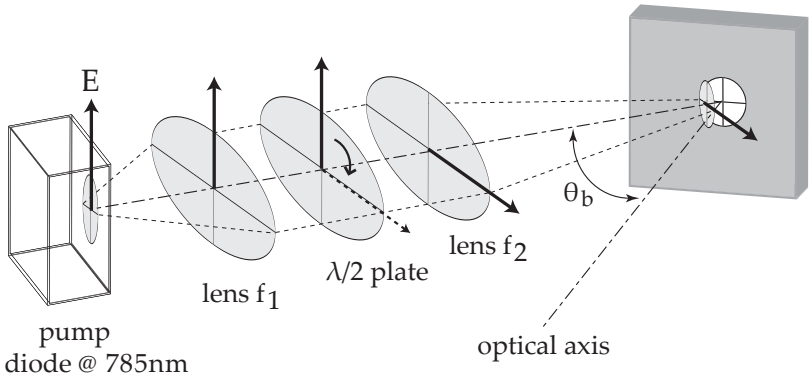

Figure 2.7 – *Schematic of the optical pumping system realized with a polarized single mode pump source. The pump is injected with an angle of incidence $\theta_b \sim 70°$ with respect to the optical axis, corresponding to the Brewster angle* [2].

over several maxima by spacing them so that the pump absorption generates a uniform carrier density in each well. The beam from the pump diode is collimated and focused on the $1/2$–VCSEL structure. For this, two lenses are used whose focal lengths are chosen according to the divergence of the pump beam and the desired size of the latter on the sample. The angle of incidence of the pump beam with respect to the optical axis of the laser cavity is chosen close to the Brewster angle, i.e. $\theta_b = \arctan\left(\frac{n_{sc}}{n_0}\right) \simeq 75^{\circ}$. This allows both to minimize the reflection on the sample surface and to compensate the ellipticity of the beam due to the angle of incidence, which is then quasi–circular on the $1/2$–VCSEL. However, the polarization of the pump beam must be transverse magnetic (TM) to minimize reflection. It is therefore necessary to rotate the polarization by 90° by inserting a half–wave plate between the two lenses (Fig. 2.7), so that the direction of polarization is along the fast axis of the beam.

C Cavity and transverse modes selection

In a VeCSEL, and more generally in lasers, the optical cavity is a crucial element on which many characteristics of the emitted beam are based, such as the spatial and temporal coherence or the laser dynamics. These characteristics will determine the possible photon eigenstates (longitudinal, polarization and transverse) for the VeCSEL laser. The complex optical field can be written as the sum of all resonant eigenmodes of the cold cavity as follows [137]:

$$\overrightarrow{\mathcal{E}}(x,y,z,t) = \sum_n \sum_q \sum_i \underline{E}_{n,q,i}(z,t)\underline{F}_{n,i}(x,y,z)\text{exp}(iw_0 t)\overrightarrow{u_i} \tag{2.7}$$

where $\underline{E}_{n,q,i}(z,t)$ is the complex longitudinal component and $\underline{F}_{n,i}(x,y,z)$ is the complex transverse component of the field of transverse index n, longitudinal index q and projected onto the polarization axis defined by the unit vector $\overrightarrow{u_i}$. Each mode oscillating in the linear cavity makes many roundtrips and thus forms a standing–wave. For the intra–cavity wave to enter resonance, the electric field must be in phase after one roundtrip in the cavity. The wave vector $k = 2\pi/\lambda$ must then satisfy the relation $kL_c + \phi = q2\pi$, where q is an integer and ϕ is the sum of the phase shifts accumulated during the propagation of the wave along the optical path. Assuming a stationary wave along the z axis of the cavity, the expression for the field developed on the basis

of the cavity longitudinal eigenmodes $w_{n,q,i}$ is obtained as follow:

$$\underline{E}_{n,q,i}(z,t) = \underline{E}_{n,q,i}(t)\cos(k_{n,q,i}z)\exp(i(w_{n,q,i} - w_0)t) \tag{2.8}$$

The optical path being mainly determined by the length of the external cavity ($L_{\mu c} \ll L_c$), the spectral interval between two longitudinal modes is expressed as:

$$FSR = \frac{c}{2L_c} \tag{2.9}$$

For a cavity length of $10\ \mathrm{mm}$, the FSR is $15\ \mathrm{GHz}$. However, the laser is likely to oscillate on all longitudinal modes of the cavity located in the part of the gain where the equivalent single pass gain compared to an equivalent loss level. The strategies to guarantee the longitudinal single–frequency operation and the associated $1/2$–VCSEL structures will be showed. The field can be decomposed along two polarization axes $\overrightarrow{u_\parallel}$ and $\overrightarrow{u_\perp}$ form an orthogonal basis ($\overrightarrow{u_\perp} \cdot \overrightarrow{u_\parallel} = 0$) according to the expression:

$$\begin{aligned}\overrightarrow{\mathcal{E}}(x,y,z,t) = &\sum_n \sum_q \underline{E}_{n,q,\parallel}(z,t)\underline{F}_{n,\parallel}(x,y,z)\exp(iw_0t)\overrightarrow{u_\parallel} \\ &+ \sum_n \sum_q \underline{E}_{n,q,\perp}(z,t)\underline{F}_{n,\perp}(x,y,z)\exp(iw_0t)\overrightarrow{u_\perp}\end{aligned} \tag{2.10}$$

In addition, semiconductor materials exhibit slight birefringence, which leads to degeneracy lifting of the polarization modes. The frequency difference between two linear polarization modes depends on the birefringence δn of the semiconductor material, the penetration length of the wave in the semiconductor $L_{\mu c}$ and the external cavity length L_{air} by the following relation:

$$\delta\nu = \frac{L_{\mu c}\delta n}{n_{sc}L_{\mu c} + L_{air}}\nu \tag{2.11}$$

A VeCSEL emitting at $1\ \mu\mathrm{m}$ with $L_{air} = 8\ \mathrm{mm}$, $L_{\mu c} = 3\lambda/2$ (less than structure GaAs barrier due to Beer-Lambert absorption), $n_{sc} = 3.5$ at $1064\ \mathrm{nm}$ and $\delta n = 2.5 \times 10^{-4}$, an intermodal frequency difference of about $15\ \mathrm{MHz}$ is obtained. The laser can therefore potentially oscillate on two polarization modes at the same time or jump between two modes and thus induce additional beat noise or generate strong intensity variations. There is a class of solutions, the Gaussian transverse modes, which are an excellent approximation for lasers using a stable optical cavity formed by spherical mirrors. There are several families of Gaussian transverse eigenmodes that can be stabilized in an optical cavity such as the Hermite–Gauss or Laguerre–Gauss modes. The DF-VeCSEL used during this thesis is based on Laguerre–Gauss modes. Laguerre–Gauss modes are the eigenstates of a rotationally symmetric laser cavity constituting one of the families of Gaussian solutions of the paraxial wave equation. This basis is well adapted to describe the modes stabilized by the hemispherical cavity of a VeCSEL where the thermal lensing effects are limited because the volume of the active medium is much smaller than the volume occupied by the mode. LG modes are characterized by two indices p and m and by a parameter w_0, the radius at $1/e^2$, which gives its size. The radial index p is a positive or zero integer determining the number of zeros ($p+1$ rings) encountered in the radial direction. The azimuthal index m is a relative integer indicating the number of azimuthal zeros ($2m$ lobes). The normalized profile of the electric field of an LG_{pm} mode of the order of $2p + m$ has the expression in

cylindrical coordinates (r, θ) [122]:

$$\underline{E}_{n,i}(r,\theta,z) = E_0 \frac{w_0}{w(z)} \sqrt{\frac{2p!}{(1+\delta_{0m})\pi(m+p)!}} \exp\left(-\frac{r^2}{w^2(z)}\right) L_p^m\left(\frac{2r^2}{w^2(z)}\right)\left(\frac{\sqrt{2}r}{w(z)}\right)^m \times \exp\left\{i\left(-kz + \phi(z)(1+m+2p) - k\frac{r^2}{2R(z)}\right)\right\}\cos(m\theta) \tag{2.12}$$

The parameters $w(z)$ and $R(z)$ represent respectively the radius of the beam (measured at $1/e^2$) and the radius of curvature of the wavefront, and the parameter $\phi(z)$ represents the phase deviation from a plane wave along the axis of propagation, which is called Gouy phase. They are expressed by the following relations:

$$w(z) = w_0\sqrt{1+\left(\frac{z}{z_r}\right)^2} \tag{2.13}$$

$$R(z) = z\left(1+\left(\frac{z_r}{z}\right)^2\right) \tag{2.14}$$

$$\phi(z) = \arctan\left(\frac{z}{z_r}\right) \tag{2.15}$$

with z_R the Rayleigh length:

$$z_R = \frac{\pi w_0^2}{\lambda} \tag{2.16}$$

This length corresponds to the length over which the beam waist increases by $\sqrt{2}$ from its minimum value w_0. These relationships show that the field profile of a perfectly Gaussian beam is entirely determined by only two physical parameters: the wavelength of the laser beam λ in the propagation medium and the size of the beam waist w_0 where the wavefront is planar.

2.2.3 Coherence, power and tunability

The Fig. 2.8 shows typical VeCSEL performances for a short cavity (around $1\ \mathrm{mm}$) using $785\ \mathrm{nm}$ pump diode. The laser is operating at RT in CW at $\lambda \sim 1\ \mu\mathrm{m}$, the threshold density is around $1.8\ \mathrm{kW/cm^2}$ (waist mode of the laser of about $30\ \mu\mathrm{m}$) with a maximum output power of $60\ \mathrm{mW}$. Once the maximum power reached, an effect called thermal roll–over appears. This phenomena is related to the gain shift at higher optical pumping. In this case, the gain begins to lower. To provide more optical power from the VeCSEL, a solution consist to excite optically the $1/2$–VCSEL with a larger pump spot. Another solution consists to use more QWs in order to delay the thermal roll–over. The polarization state of the laser is linear along the [110] direction of the gain mirror with a measured purity better than $75\ \mathrm{dB}$ thanks to the combination of gain dichroism and linear birefringence in the $1/2$–VCSEL gain structure. The laser shows a TEM_{00} circular transverse beam distribution close to the diffraction limit ($\mathrm{M}^2 < 1.2$) with a low divergence ($1°$ FWHM) over the whole laser operation range thanks to its stable optical cavity. This laser is tunable as far as $6\ \mathrm{nm}$ ($1.5\ \mathrm{THz}$). The laser wavelength can be tuned by varying the cavity length or temperature. The spectral shift for the temperature is $0.35\ \mathrm{nm}/K$ (for GaAs

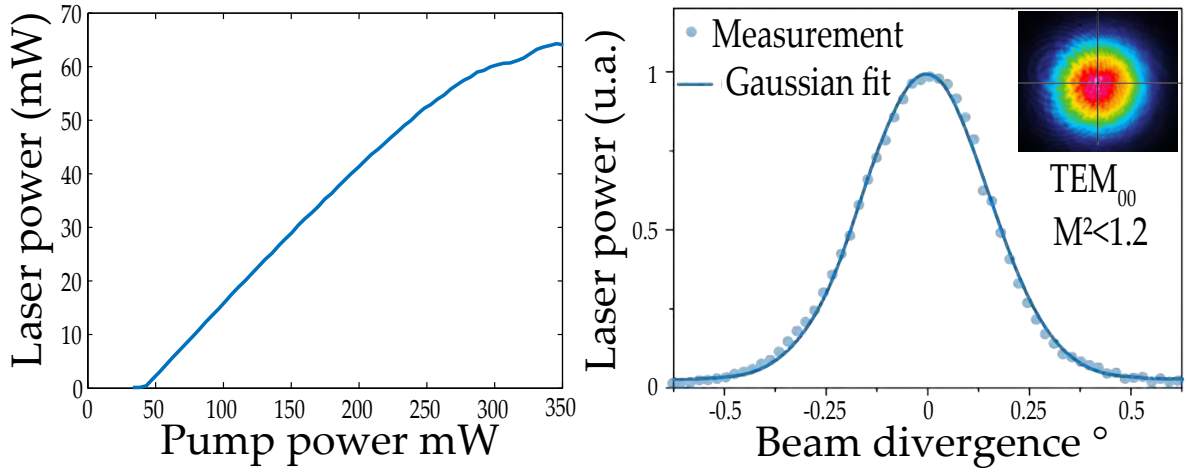

Figure 2.8 – *VeCSEL performances. Left) Output power as a function of pump power at room temperature. Right) typical beam quality for single-mode* TEM_{00} [1].

structures). The SMSR is 60 dB and reached the quantum limit. These measurements were done by a previous PhD student [1].

2.2.4 Applications

VeCSELs appear to have a huge potential for widespread applications. In fact, they combine several important features:

— **Wavelength versatility**: VeCSELs can be used to address a lot of wavelengths inaccessible with traditional solid–state lasers.

— **High–output power and beam quality**: particularly OP–VeCSEL offer a combination of high–output power and excellent beam quality.

— **Cheap mass-production**: VeCSEL gain structures can be fabricated with a wafer technology.

A non–exhaustive list of applications is showed below:

— **High–precision metrology & spectroscopy:** VeCSELs can be used in atomic clocks as they are considered low–noise laser source. Another specific application can be found in interferometry experiences such as VIRGO.

— **THz science and technology:** Dual–Frequency (DF) VeCSEL can be used for THz emission.

— **Communication:** Structured–light laser source can be used for spatial multiplexing and thus, increase transmission capacity in a single optical fiber.

— **Optical trapping:** Coherent vortex–based VeCSEL can be used for optical trapping. They can also control the angular direction of a molecule.

— **Gas analysis:** Single–frequency/dual–frequency VeCSEL can analyze gas in the IR/THz range.

2.3 DF–VeCSEL: state of the art

The use of a dual–frequency laser source in the context of photomixing for the THz generation has certain advantages over the use of two independent sources. Indeed, the lack of correlation between two separate sources will degrade the spectral purity of the THz beat obtained, in particularly for optical sources with low intrinsic spectral quality. In this case, several techniques must be implemented in order to finely control the beat frequency whose spectral purity directly depends on the quality and complexity of these. The use of a single dual–frequency laser source is then a straightforward solution, both in terms of spectral purity and compactness. Through the use of a common cavity and pumping system, the frequency variations of the two modes, due to thermal and mechanical disturbances are reduced and the difference frequency is stabilized. However, emitting on a dual–frequency laser state is not easy due to the tendency of a laser to oscillate in a single mode (for homogeneous–broadening gain medium without non–linearity) system or in several modes ($\gg 2$) (for inhomogeneous–broadening gain medium and/or non–linearity). Thus, an important characteristic of the dual–frequency source is the single–frequency character of each of the two modes. Indeed, the source can send two packets of separate modes with a difference equal to the desired THz frequency. Another parameter is the power delivered by each of the two modes. The two optical powers must be as balanced as possible. In addition, the two frequencies must be transmitted simultaneously. Finally, the last point concerns the tunability of the dual–frequency lasers. It is difficult to have a high tunability for a dual–frequency laser compared to systems with two laser diodes where it is possible to change the temperature/bias current of each of the diodes independently, or changing the angle of the optical grating for extended cavity lasers. Tunability can be done continuously or by mode jump with a value equal to the Free Spectral Range (FSR) of the cavity. Different concepts of dual–frequency sources have already been studied and developed. Among them, we can distinguish two main approaches: the first one is based on the intra–cavity integration of selective wavelength filters in order to select two longitudinal modes, the second one consists in producing a laser source oscillating on two orthogonal polarization modes in order to stabilize the two optical frequencies.

2.3.1 Different strategies

A Longitudinal modes

The basic principle of these sources is based on the extension of their method of obtaining the single–frequency regime to a dual–frequency emission according to a given laser technology. These sources consist of a laser cavity associated with two optical filters, each of which has the role of selecting one of the frequencies or longitudinal modes of the cavity. Different types of dual–frequency lasers have been developed based on monolithic or external cavity semiconductor lasers, doped fiber lasers [138] or Ti:Sa lasers [139, 140]. The filters used in this type of setup are birefringent filters, Fabry–Perot standards or Bragg gratings with high spectral selectivity [141]. The small size of solid–state laser sources has naturally led to the study of alternatives based on distributed Bragg reflector (DBR), distributed feedback (DFB) or vertical cavity surface emitting (VCSEL) semiconductor lasers, offering the prospect of ultra–compact dual–frequency monolithic sources. These different approaches consist in the integration along

the same optical axis of two DBR, DFB or VCSEL laser sections. Lasers using two DBR sections [142], with double DFB sections longitudinally [143, 144] or laterally [145] and with double coupled vertical cavities have been realized. However, few of them offer satisfactory performances mainly due to difficulties in managing the modal competition between the two modes. As a result, these lasers may exhibit stable dual–frequency emission but with limited tunability. The transition from one spectral position to another leads in most cases to repercussions on the previously mentioned characteristics such as single frequency operation on each of the two modes and/or the power balance between them. In addition, the beat frequency range is often restricted to either too small ($< 100\,\mathrm{GHz}$) or too large [146] ($> 3\,\mathrm{THz}$) shift depending on the type of dual–frequency laser developed and the intended application. The operation may become unstable and/or multimode due to too much modal competition, non–linear coupling between the two modes in the gain medium [147] as well as spatial Hole Burning phenomena. Another dual–frequency laser architecture has also been studied [148, 149]. It consists of a collimated anti–reflection treated $1/2$–VCSEL, a diffraction grating and a mirror system. The operating principle is similar to the Littman configuration classically used in external cavity lasers (ECDL), but uses the grating at first order (λ_0) so as to disperse the multimode spectrum of the $1/2$–VCSEL onto a V–shaped structured mirror allowing optical feedback of only two frequencies λ_1 and λ_2. The tunability of the device is obtained mechanically by moving the V–shaped mirror vertically in order to vary the spacing in the propagation plane of the beams and thus the frequencies oscillating in the cavity. The available frequency range depends on the grating dispersion, the focal length of the lens and the size of the V–mirror, the maximum frequency difference being fixed by the width of the $1/2$–VCSEL gain curve. However, the spectral selectivity of this device is not sufficient to ensure emission over a regime where both frequencies oscillate in a single longitudinal mode [150].

B Polarization modes

One solution to modal competition problems is to consider two crossed polarization optical modes sharing the same cavity, which allows to obtain a natural stability of the beat frequency. This approach consists in lifting the degeneracy between the two modes by exploiting the birefringence of some materials to produce two crossed linear polarization states in an optically pumped solid–state laser source. The tuning of the frequency difference between the polarization axes is achieved by using crystals exhibiting an electro–optical effect (Pockels effect, Kerr effect) or thermo–optical effect. Optical beats in the range of a few tens of GHz have thus been obtained. However, the accessible frequency range being inversely proportional to the length of the laser cavity, this cavity architecture is no longer usable for an operation beyond $100\,\mathrm{GHz}$ and towards THz frequencies. Since then, optical frequency differences of several THz between the two modes have been achieved by intra–cavity spatial separation of the two modes, as well as by using a higher bandwidth gain medium [151]. The birefringent crystal is cut at $45°$ from its optical axis, so that it causes a thickness–dependent spacing between the two cross–polarized beams. The beams are separated at the active medium side and then superimposed at the output coupler side. The spatial separation at the gain medium reduces the non–linear coupling between the two modes to achieve simultaneous and robust oscillation. This separation is also leveraged by introducing two thin etalons, one for each mode, which allow for independent selection of the emission wavelength of each state, as well as ensuring that each state oscillates on

a single longitudinal cavity mode. THz beat tunability is achieved by adjusting the orientation of a thin etalon, while the other etalon remains fixed. High spectral purity beats up to 3.1 THz have been achieved with 100% modulation rate using this cavity architecture. This principle has been implemented for the realization of dual–frequency sources having as gain medium crystals such as Nd:YAG [152], Er:Yb:glass [151, 153] or Yb:KGW [154, 155] or a semiconductor [156]. Nevertheless, these sources exhibit relaxation oscillations characteristic of class B lasers where the lifetime of photons in the cavity is short in front of the lifetime of the population inversion, resulting in the appearance of relative intensity noise at relaxation oscillation frequencies of a few kHz to a few MHz and sidebands around the beat. In addition, the dual–frequency nature of the source adds a noise contribution that results from the coupling between the two modes in the gain medium called partition noise or anti–phase noise (applicable only for a few lasers). Today, research is focused on stabilizing the beat frequency [157] and on reducing this anti–phase noise, either by orienting the polarization states of the dual–frequency laser with respect to the crystallographic axes of the gain medium [158], or by realizing a dual–frequency source from a class–A laser whose dynamics is devoid of relaxation oscillations [159].

C Transverse modes

The dual–frequency laser based on transverse modes has been recently demonstrated [3]. The dual–frequency laser is based on VeCSEL technology to ensure high coherence, tunability and power. The laser emits LG transverse modes, where the fundamental mode operating at certain wavelength and the higher transverse modes operating near the fundamental mode wavelength. The spatial overlap between these two transverse modes is small enough to avoid modal competition, and large enough to allow for THz generation by optical beating. In the next section, the results using Df-VeCSEL based on LG transverse modes are shown.

2.4 DF–VeCSEL based on Laguerre–Gauss transverse modes

All the results included in this section were obtained during the thesis of R. Paquet [3, 118]. They are the fundamental basics that would allow to obtain the results obtained in Chap. 4. The DF–VeCSEL is shown in the Fig. 2.9. They were grown on a [001] GaAs doped substrate in a low–pressure metal–organic chemical vapor deposition (MOCVD). They contain a high–reflectivity (99.9%) $Al_{0.85}Ga_{0.15}As$/GaAs 27–pairs Distributed Bragg Reflector (DBR), and a $13\lambda/2$–thick active layer. It contains 6 strain-balanced InGaAs/GaAsP QWs emitting at $\lambda \simeq 1\,\mu m$ and GaAs pump absorbing barriers. Strain compensation layer of GaAsP are included to avoid plastic relaxation of the active region structure. These QWs are located on optical standing–wave antinodes from surface to Bragg such as the excited carrier density is almost equal in all QWs to ensure a low laser threshold and a homogeneous gain [118]. The active region is designed for efficient optical pumping in the thick GaAs barriers with a GaAs commercial diode laser emitting in the 780–830 nm range. The total pump absorption in the barriers is $\sim 87\%$. The 6 QWs provide enough gain to compensate 1% of optical losses. The measured spectral shift of the maximum gain with optical losses is found to be $\delta\nu/\delta g = 600\,\mathrm{GHz}/\%$. QW gain (dichroism) along the [110] crystal axis is measured to be 10% superior to the one along the $[1\bar{1}0]$. The aim is to achieve at least 3 THz optical beating with mainly the contribution of thermal profile gradient from the pump lasers. The transverse filter consists in a 10–nm–thick Cr mask, induces $\sim 90\%$

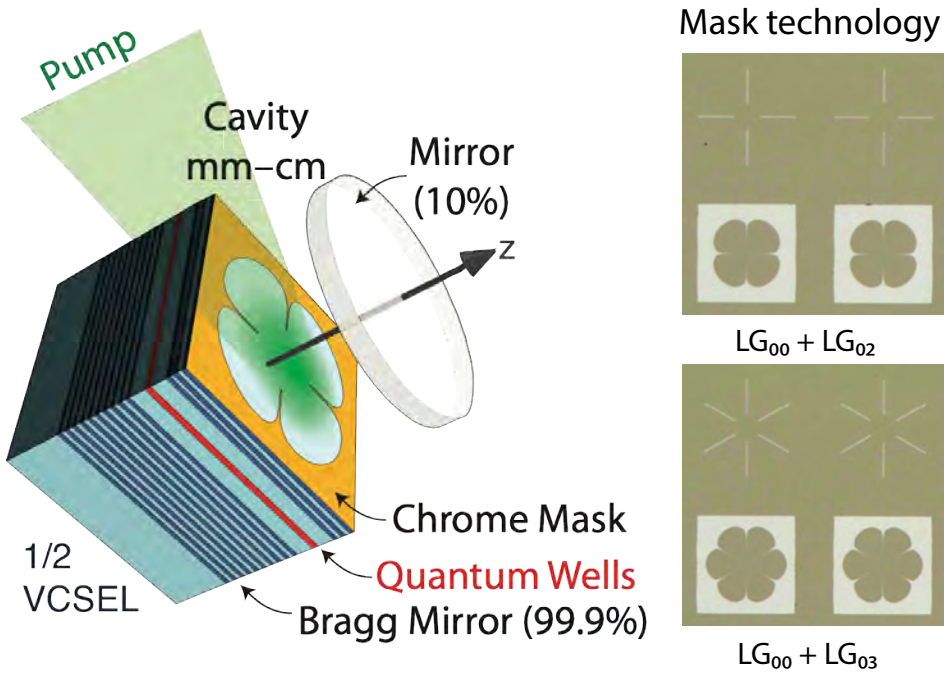

Figure 2.9 – *VeCSEL technology: Left) VeCSEL design and technology. Short plano-concave cavity for dual-frequency emission. Right) Metal masks for the transverse modes* LG_{00} *plus* LG_{0m} $(m = 2, 3$ *here).*

optical losses for a filling factor of 1 [118]. Its transverse shape is computed and processed by a e–beam lithography and reactive ion etching to dramatically increase losses for unwanted LG modes $(> 10\%)$, while ensuring low losses for at least the two targeted LG modes. Two laser design were used in order to reach stable dual–frequency operation: 1/ Structure with resonant filter (additional Bragg reflector) and 2/ Structure with anti–reflection coating. The best results are obtained with 1/ by reinforcing the micro–cavity effect. Fig. 2.10 shows the spatial filter in order to select the wanted LG transverse modes.

Fig. 2.11 illustrates the modal gain of two wanted modes, and their overlap leads to the transverse spatial hole burning that allows for stable dual-frequency operation.

2.4.1 Power and coherence

The maximum output power of the DF–VeCSEL is about 80 mW for an optical pumping power of 400 mW, as shown in the Fig. 2.12. The threshold for each transverse modes is slightly different and the efficiency for the fundamental mode is greater when the threshold of the higher transverse mode is achieved. Fig. 2.12 shows the spectrum of the modes emitted around 1060 nm. The SMSR of each longitudinal modes is $\sim$ 60 dB. It also shows that the difference frequencies are achieved at 300 GHz (black) and at 650 GHz (blue). These are achieved by increasing the optical pump power.

Fig. 2.13 (left) illustrates the spatial distribution of the LG_{00} & LG_{02}. The measurements fit very well with the theory. On the right, the measured waist as function of the propagation distance is shown. The LG_{00} & LG_{02} presents similar results and the M^2 is at diffraction limit. This means that the DF–VeCSEL is highly coherent spatially. This is required for stable and powerful optical beating. Fig. 2.14(a) illustrates the distribution of intensity and phase of each LG transverse modes. The phase shifts from 0 to π for each consecutive lobes. In the Fig. 2.14(b)

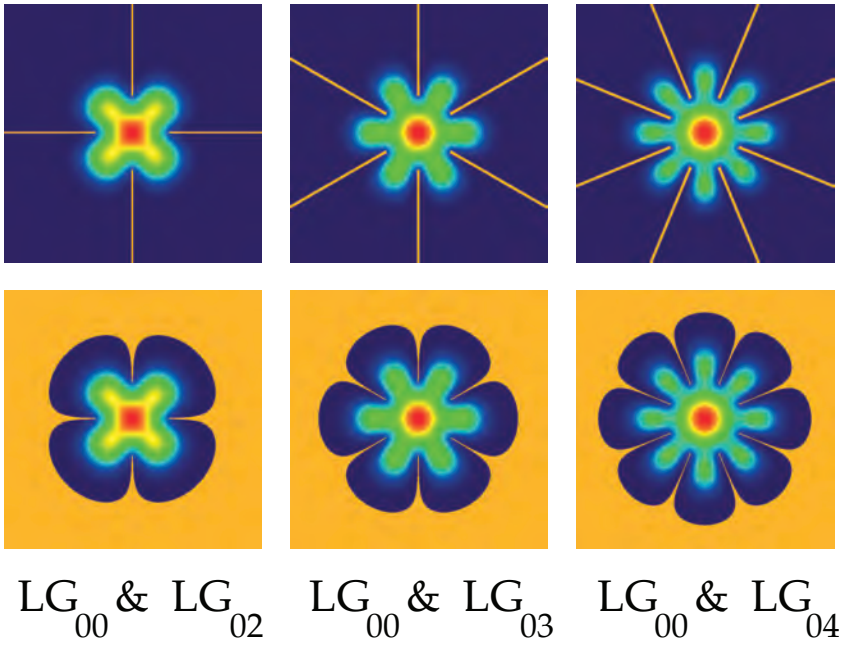

Figure 2.10 – *Geometries in the transverse plane of the loss masks to select modes LG_{00} & LG_{02}, LG_{00} & LG_{03} and LG_{00} & LG_{04} [3]. Top) cross shape mask. Bottom) negative drawing mask. Both select the desired transverse modes.*

is illustrated how to couple the beam into a PM single-mode optical fiber when LG_{00} & LG_{02} is used. Previous simulations were done to quantify the beating efficiency into a single–mode optical fiber [118], as seen in the Fig. 2.15 [118].

2.4.2 THz generation

THz generation using this DF–VeCSEL was already demonstrated using a commercial UTC designed at $1550\ \mathrm{nm}$. During these experiments, the LG_{00} & LG_{02} were used, Fig. 2.16 shows the experimental setup. The optical isolator was used to avoid parasitic feedback. Only one optical beating spot among the 4 possible spot of the LG_{00} & LG_{02} transverse modes was collected by using SM & PM optical fiber (maximum injected power: roughly tens of mW if LG_{00}/LG_{02} is used). No optical amplifier was used. The optical beating was then focused to the commercial UTC–PD. The maximum THz output power of the commercial UTC–PD was $1\ \mu\mathrm{W}$ around $250\ \mathrm{GHz}$. The THz wave is then collimated and focused into the heterodyne receiver using a pair of Teflon lenses ($\sim$ $2\ \mathrm{dB}$ loss in free space including lenses). The THz is then analyzed with a RF analyzer with external heterodyne head, as it can be seen in the Fig. 2.16 (right). A THz output power of roughly $1\ \mu\mathrm{W}$ at around $255\ \mathrm{GHz}$ is illustrated within a span of $50\ \mathrm{MHz}$ and limited by the maximum optical flow of the UTC [118, 160]. The linewidth of the THz pic is at sub–MHz level.

2.4.3 Tunability

Fig. 2.17 (left) shows the tunability of the frequency difference of the DF–VeCSEL as function of the optical pumping power. LG_{00} & LG_{03} and LG_{00} & LG_{04} present similar results in terms of tunability, while the LG_{00} & LG_{02} are less tunable. The coupling between modes decreases

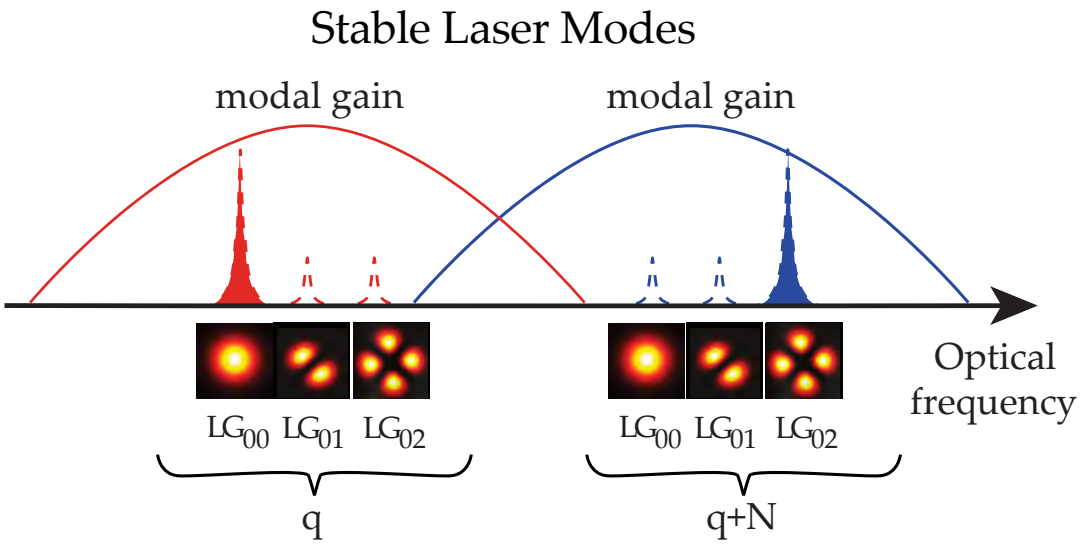

Figure 2.11 – *Spectrum of the dual–frequency VeCSEL* [3]. *N is the adjacent longitudinal modes. These transverse modes selection is through natural hole burning.*

when the order of transverse mode is higher. The latter is due to the spatial coupling between the fundamental transverse mode and the higher transverse mode. To summarize, LG_{00} & LG_{03} presents the best tunability results ranging from 50 GHz to nearly 700 GHz. The physical origin of the great tunability of the DF–VeCSEL is still under investigation, but it relies on the radial thermal gradient related to the optical pumping. The fundamental mode operates at a higher modal temperature than the higher order one, thus leading to a frequency differential driven by the optical pump power. Fig. 2.17 illustrates the tunability of the THz beating as function of the optical pumping power. Two heterodyne receivers were used, the first one operating around 100 GHz and the second one operating around 300 GHz. The THz output power achieved at 82 GHz was low compared to the other THz pics because of the low–optical power of the optical beating and to a reduced antenna efficiency of the UTC–PD emitter. Then, for both heterodyne receivers, the THz power decreases gradually despite an increase of the optical pumping power due to the UTC–PD cut–off frequency and the antenna dimensions.

2.4.4 Frequency noise

Fig. 2.18 (left) illustrates the comparison of the frequency noise performance between optical light and THz light. The LG transverses modes presents similar noise while the THz frequency noise is lower by at least 4 decades. In fact, the optical noise of the VeCSEL is mainly due to the relative intensity noise (RIN) of the pump diode lasers. This validated the concept of dual–frequency lasers because the optical counterparts share the same optical noises and thus the THz frequency noise is reduced. In the Fig. 2.18 (right), the linewidth of the THz beating as function of observation time is shown. The evolution of the linewidth is at Fourier limit for observation time lower than $10^{-}5$, thus proving the stability and the high coherence of the THz beating.

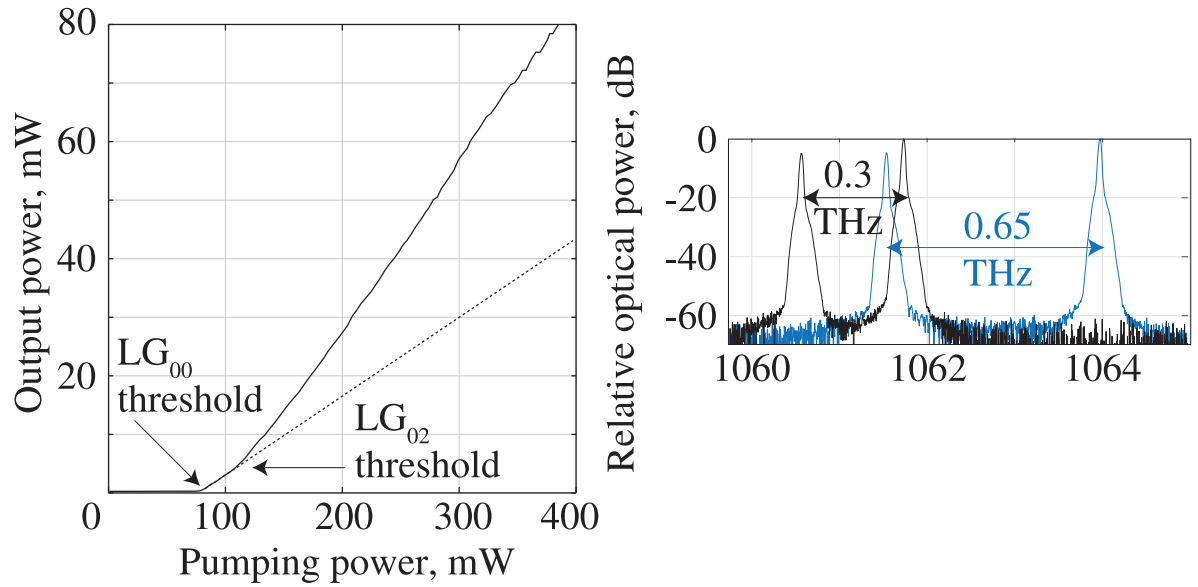

Figure 2.12 – *Optical characterization: Left) Output power as function of pumping power for the LG_{00} & LG_{02}. LG_{00} and LG_{02} have slightly different threshold. A change of efficiency is noted around a pump power of* 110 mW*, revealing the LG_{02} threshold. Right) Spectrum of the bi–longitudinal modes emitted at around* 1060 nm *with spacing modes at* 0.3 THz *(black) and* 0.65 THz *(blue) respectively, by increasing the pumping power* [118].

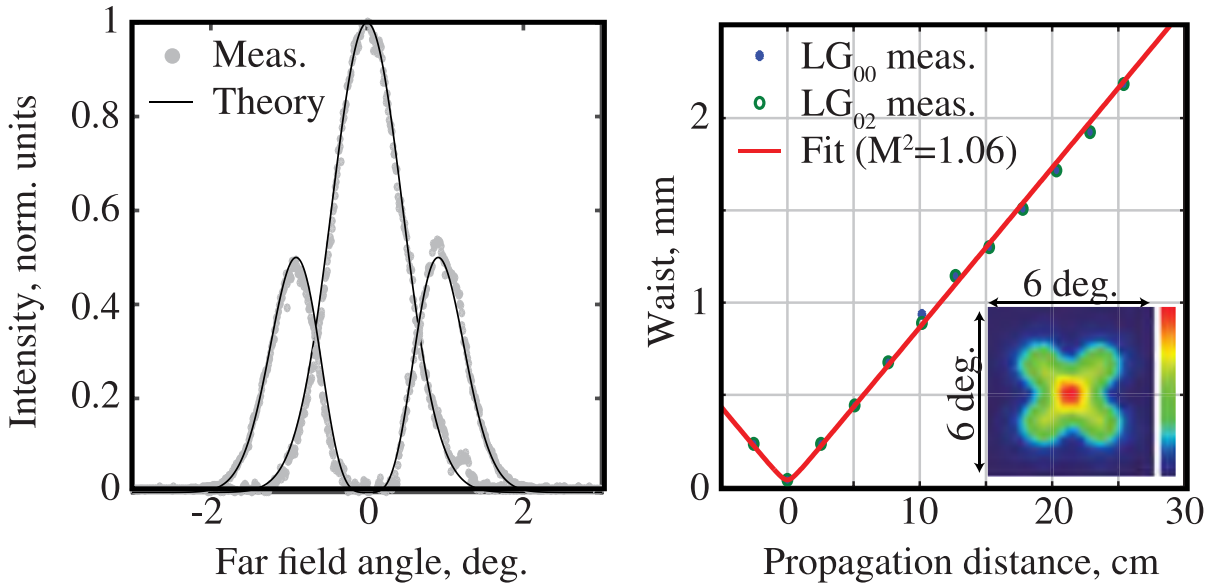

Figure 2.13 – *Optical characterization: Left) Normalized intensity as function of far–field angle (measurement versus theory). Right) Beam waist as function of propagation distance for the LG_{00} & LG_{02}* [118].

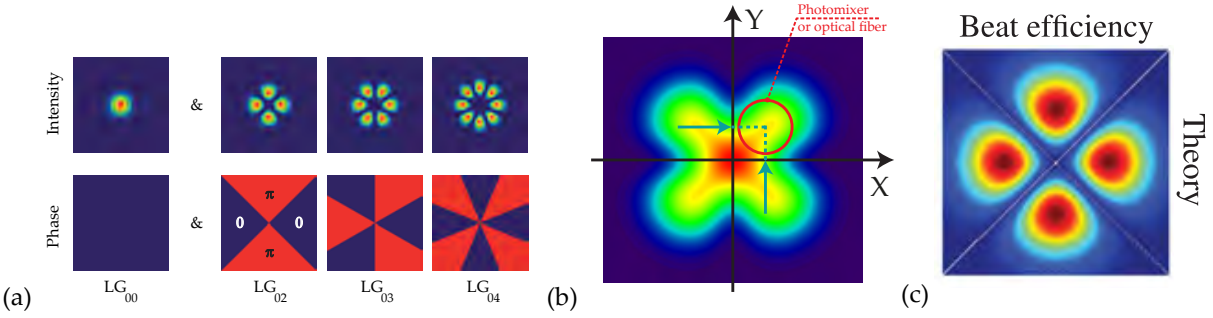

Figure 2.14 – *a) Intensity profiles for the two LG modes of the dual-frequency laser. The first mode is in all cases the fundamental mode LG_{00} and the second higher order mode LG_{0m} with $m \geq 2$ outside the cavity. b) Schematic representation of the single–lobe coupling for the modes LG_{00} & LG_{02} by offsetting the photomixer or optical fiber from the dual–mode beam axis* [3]. *c) Beat efficiency for the transverse modes LG_{00} & LG_{02} inside the single–mode optical fiber (theory)* [118].

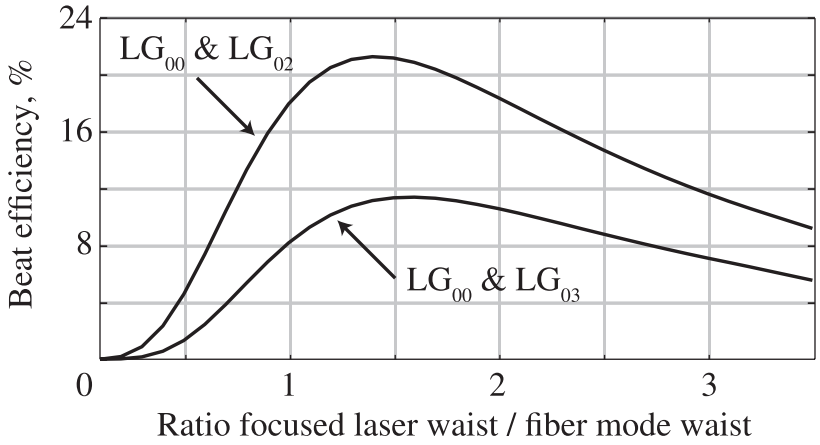

Figure 2.15 – *Beat efficiency (defined as the ratio of the beat power over the beat power that would be emitted if two modes were perfectly collinear.) as function of the ratio of the focused laser waist to the fiber mode waist for* LG_{00} *&* LG_{02} *and* LG_{00} *&* LG_{03} *[118].*

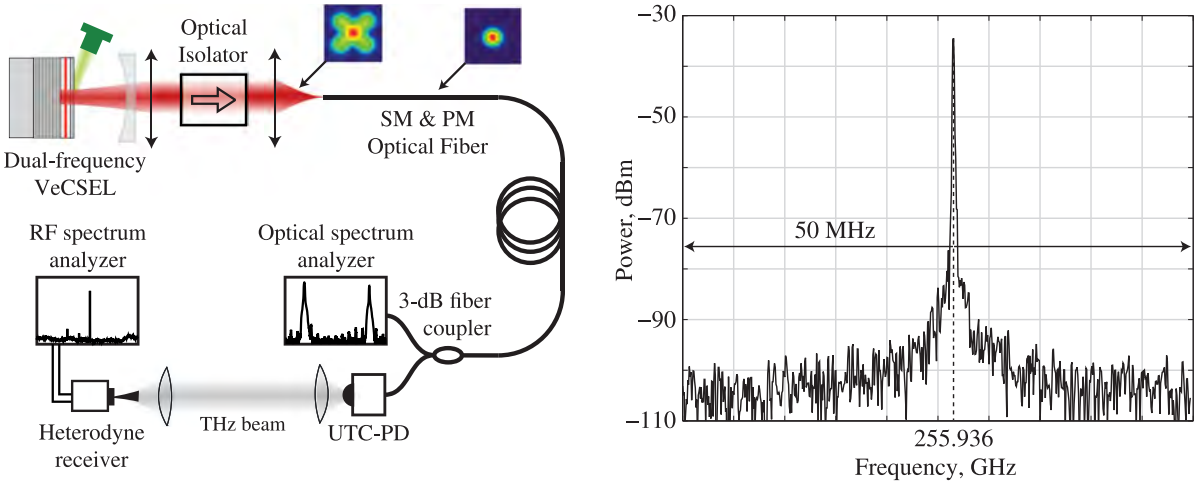

Figure 2.16 – *Experimental results: Left) Experimental setup for* THz *generation using VeCSEL as an optical source and commercially available UTC–PD (designed for* 1550 nm *excitation) as photomixer. Right) Spectra of* THz *emission at around* 255 GHz *[118].*

The DF–VeCSEL is so an excellent candidate for next–generation THz sources, paves the way towards a compact, low–cost, powerful, coherent, and tunable THz source. During this thesis, only LG_{00} & LG_{03} were used because of a trade–off between available beat intensity and the modal competition, related to the spatial overlapping between LG_{00} and the higher transverse modes LG_{0m}.

2.5 Summary

In this chapter, a state–of–the–art of dual-frequency lasers was drawn up to highlight important features including power, tunability and coherence. These features can open the door to many applications such as spectroscopy, communication, imaging, and many others. It is relativity "easy" to fabricate a single–frequency laser or a multi–frequency laser but it is quite challenging for a dual–frequency laser. In fact, the modal competition is too strong to lase in dual configuration mode. Three different approaches are used: longitudinal, polarization and transverse modes. Our DF–VeCSEL is based on the LG transverse modes. Thanks to the competition management, a very stable and coherent CW DF–VeCSEL is now available. Powerful,

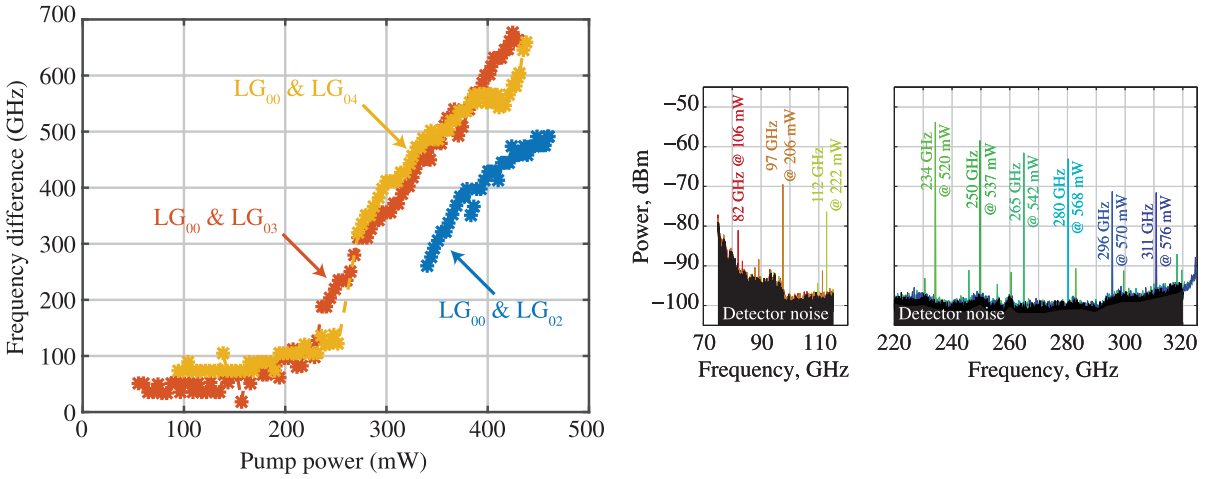

Figure 2.17 – *VeCSEL tunability: Left) VeCSEL tunability for each couple of transverse modes* LG_{00} *&* LG_{02}*,* LG_{00} *&* LG_{03} *and* LG_{00} *&* LG_{04} *as function of pump power. Greater the pump power, greater is the spacing modes. Right)* THz *beating tuned with optical pump power* [118].

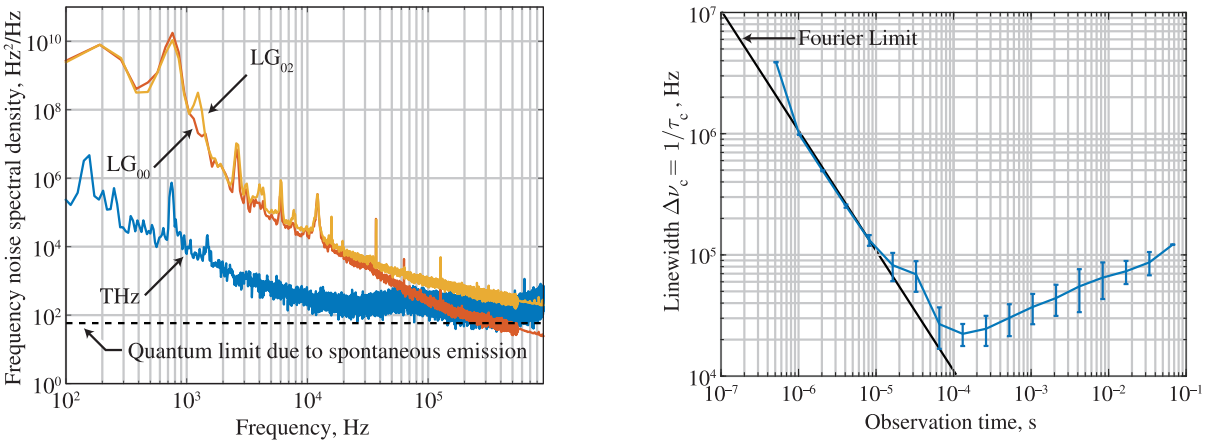

Figure 2.18 – *Frequency noises: Left) Frequency noise spectral density as function of frequency for* LG_{00}*,* LG_{02} *and* THz *beating. Right) Linewidth as function of observation time* [118].

tunable, and coherent dual–frequency laser working at room temperature is required for THz science and technology and can operate both in pulsed and CW modes. The CW DF–VeCSEL based on LG transverse modes meet all these requirements. As a results, a compact, tunable and coherent THz source working at room temperature is available. However, the THz power is still low (< 10 μW at 300 GHz) due principally to the low optical–to–terahertz conversion of photomixers. The goal of multipolar antennas is to be used for spatial multiplexing in order to increase the THz output power.

Chapter 3

Multipolar Antenna: Analysis and Design

Introduction

DF–VeCSELs based on Laguerre-Gauss transverse modes demonstrated to be an excellent candidate for THz emission. However, the THz output power (μW-level) is still low compared to the state–of–the–art even if the photomixer was limited in terms of THz output power due to maximum optical flux acceptance. During previous experiments, only one available optical beat was used. To maximize the optical beating efficiency and so the THz power, original antennas are required. The choice comes naturally to the multipolar antennas as they fit well with the multilobes nature of the Laguerre–Gauss transverses modes. By using these antennas, most of the optical power can be collected by the combination of monopoles. Thus, the THz power could increase by a factor of $\times 4$, $\times 6$ or $\times 8$ depending on the LG transverse modes utilized. The choice of the multipolar antennas over antennas array will be explained later in this chapter. According to the simulation results, multipolar antennas must be designed at higher resonance (R_2 and/or R_3) order in order to increase their efficiency and thus use them for THz generation.

Electromagnetic simulations of antennas help to target optimal geometries preliminary to the sample fabrication and help to understand which parameters have the strongest impact on realized gain and input impedance. In addition, they are useful for the validation of experimentally observed effects. This chapter deals with the multipolar antennas simulations that fits with the transverse modes of the dual–frequency VeCSEL. The aim is to increase the THz power.

3.1 Fundamentals of Antennas

An antenna is usually defined as a metallic device for radiating or receiving radio waves. It is also seen as a transitional device between free–space propagation and a guiding device. Hereafter, the fundamental antenna parameters are briefly highlighted [161]:

— **Radiation pattern.** It is a graphical representation of the radiation properties of the antenna as a function of space coordinates.

— **Beamwidth.** The beamwidth of a pattern is defined as the angular separation between two identical points on opposite of the pattern maximum. Typically, the *Half–Power Beamwidth*

(*HPBW*) is widely used to quantify the angular separation between two identical points.

— **Gain.** Another useful parameter describing the performance of an antenna is the gain. The gain is obtained with respect to the reference antenna. The reference antenna is usually a *lossless isotropic source*. Lossless isotropic source means that an antenna radiates equally in all directions without loss. The gain terms are usually compared with the gain of the reference antenna to quantify the gain of a real antenna. And the gain and the directivity are related by:

$$G_{abs} = e_0(1 - |S_{11}|^2)D_0 \tag{3.1}$$

where
S_{11} is the return loss.
e_0 is the total efficiency.
D_0 is the maximum directivity. The directivity quantifies the ability of the antenna to focus his beam in a direction.

— **Input impedance.** The impedance of the antenna is written as follows:

$$Z_A = R_A + jX_A \tag{3.2}$$

where
Z_A = antenna impedance (ohms)
R_A = antenna resistance (ohms)
X_A = antenna reactance (ohms)

In general, the resistive part of (3.2) consists of two components

$$R_A = R_r + R_L \tag{3.3}$$

where
R_r = radiation resistance of the antenna
R_L = loss resistance of the antenna

This parameter is useful to know in order to design an appropriate matching circuit between the antenna and the circuit, so that the maximum power can be transferred to the antenna or the circuit.

— **Efficiency.** The radiation efficiency of an antenna is the ratio of the gain of an antenna by the directivity.

— **Bandwidth.** The bandwidth of an antenna can be considered to be the range of frequencies, on either side of a center frequency (usually the resonance frequency for a dipole), where the antenna characteristic (such as input impedance, pattern, beamwidth, polarization, side lobe level, gain, beam direction and radiation efficiency) are within an acceptable value with respect to those at the center frequency. In practice, the bandwidth is taken when at $S_{11} = -10$ dB and it is usually 1% of the center frequency (except for quasi–independent frequency antennas).

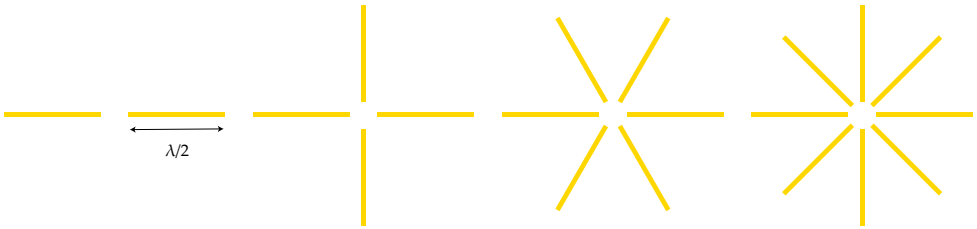

Figure 3.1 – *A dipole antenna and 3 multipolar antennas noted as MP_2 (two crossed dipoles), MP_3 (three crossed dipoles) and MP_4 (four crossed dipoles).*

3.1.1 Dipole antenna

Dipole antennas are some of the simplest, cheapest and in many cases the most versatile antennas for many applications. The radiation resistance of the antenna is strongly dependent upon the current distribution and it can written be as [161]:

$$R_r(\Omega) = \frac{2P_{rad}}{|I_0|} \tag{3.4}$$

where P_{rad} is the radiated power
I_0 is the fed current

The current distribution is assumed to be center–fed and the current vanishes at the end points ($z = \pm l/2$), where the l is the arm length). One of the most commonly used antennas is the half–wavelength ($l = \lambda/2$) dipole. Since its radiation resistance is 73 Ω, which is very near to 50–ohms or 75–ohms characteristic impedance of many transmission lines, its matching to the line is simplified especially at resonance. The total input impedance for $l = \lambda/2$ is equal to:

$$Z_{in} = 73 + j42.5\ \Omega \tag{3.5}$$

The imaginary part associated with the input impedance of a dipole is function of its length. In this case, for $l = \lambda/2$, it is equal to $+j42.5$ which is due the inductance of a long antenna.

3.1.2 Multipolar antenna vs antenna array

An antenna array is a succession of antennas equally spaced by at least $\lambda/2$. While a multipolar antenna, is a circular distribution of antennas with their distance lower than $\lambda/2$, as seen in the Fig 3.1. One could ask the following question: why use a multipolar antenna instead of an antenna array? The inconvenient of the antenna array design that fit with the LG transverse modes of the DF–VeCSEL is that the optical confinement thus the coupling efficiency between the laser beam spot and the antenna array will be very low. The reason is that for antenna array the various elements are typically distanced of d ($d = \lambda/2$) to avoid coupling while LG transverses modes are confined. In this case, a multipolar antennas could be a better solution because the laser light is more confined, and the overall coupling efficiency is improved.

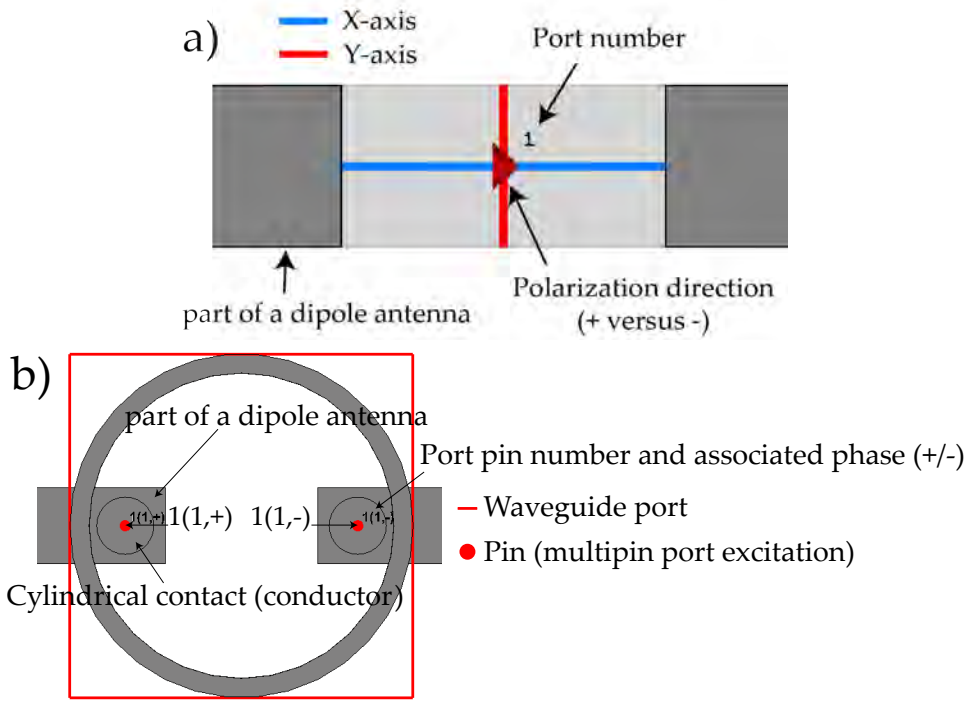

Figure 3.2 – *Difference between the discrete port excitation and multipin port excitation for a dipole antenna: a) Discret port excitation b) Multipin port excitation for a dipole antenna.*

3.2 Design and simulation results

3.2.1 Dipole antenna

A commercially available software, CST Studio Suite® [1] which is a 3D electromagnetic simulator, was used to obtain results presented in the following sections. The software is based on Finite Integration Technique (FIT). The basic idea of FIT is to apply Maxwell equations integral form to a set of staggered grids. In other words, the FIT is a spatial discretization scheme to numerically solve electromagnetic field problems in time and frequency domain.

Dipole antennas operating at 100 GHz are designed and analyzed. A comparison between the discret port and the multipin port is showed. In fact, the discret port is not supported for multipolar antennas so a waveguide containing multiple pins is required in order to simulate the multipolar antennas. The first step is to compare the effect of the multipin port excitation compared to the discret port. Their performances in terms of realized gain, input impedance and their radiation pattern are presented.

A Excitation type: discret port vs multipin port

In the Fig. 3.2, a discret port is represented by a simple arrow between the arms of a dipole antenna while the multipin port is a waveguide containing, in this case, 2 pins. For the discret port, the position of the positive excitation and the negative excitation are defined by the direction of the arrow. For the multipin port, the excitation is defined by a common port (waveguide excitation, indicated by the red square) and defined by the red dots 1(1,+) and 1(1,-) indicating

1. 2017 and 2019 versions were used during this thesis.

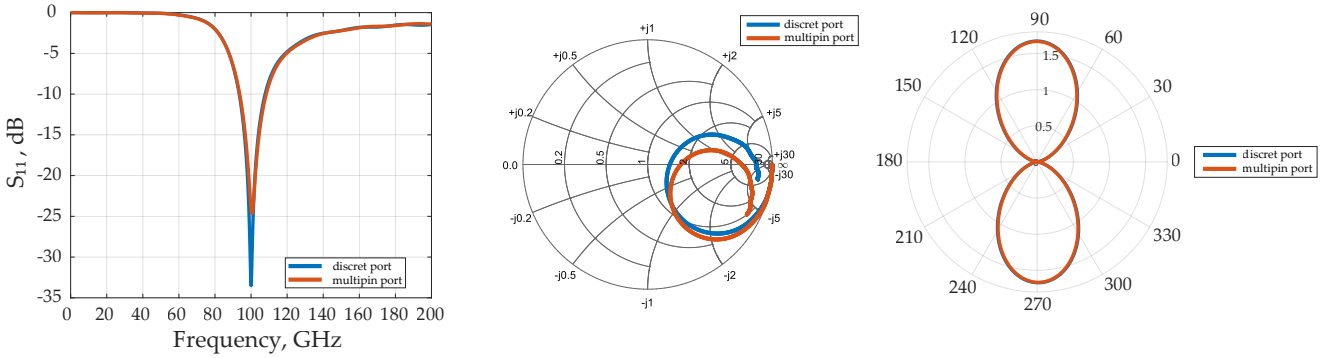

Figure 3.3 – *Comparison of dipole antenna performance using two different ports: discret port and multipin port. Three related figures (S_{11}, Smith chart and radiation pattern.)*

the position of positive and negative excitation. The impedance for both methods is set to 73 Ω.

B Antenna parameters: comparison

The antennas are designed at $\lambda/2$, using PEC as material and in a free–space environment. By doing this, the antennas can be studied independently to other deleterious effects (such relative permittivity and so forth). Fig. 3.3 shows the results for the same dipole and for each excitation type. Although the performance is similar, a loss of about ∼10 dB is displayed in the S_{11} parameter as a function of frequency (from 0 to 200 GHz). This is due to the additional capacitance effect (additional metal) as shown in the Smith chart. The pins sizes are modified in order to be adapted at 100 GHz. In Table 3.1, the fundamental parameters of the antenna and their values for both excitation types are reported. There is almost no difference in terms

Table 3.1 – *Left) Antennas parameters. Right) Principal results.*

	discr. port	multip. port		discr. port	multip. port
Arm length	660	690	Realized Gain (dBi)	2.237	2.231
Gap (µm)	80	80	Bandwidth (GHz)	14.3	14.6
Arm width (µm)	40	40	Tot. Efficiency (dB)	-0.0018	-0.0039

of antenna properties using one port or the other. The total efficiency is determined by the ratio between realized gain and directivity. All the next results on multipolar antennas were obtained by using the multipin approach. Finally, the multipin approach is well suited for experimental results because of the flexibility on the choice of the pin type (positive or negative) and also the numerical study is also extended, i.e. possibility to study the multimode nature of multipolar antennas, polarization diversity as well as the beam–steering (by adding additional phase on one or more pins).

3.2.2 Multipolar antenna: Analysis and Design

Multipolar antennas (MP) are also known as multimode antennas (MM) and are characterized by the presence of several resonant modes depending on the type of excitation, i.e. the spatial distribution of relative phases between each arm of the antenna. Fig 3.1 illustrates the three multipolar antennas MP_2, MP_3 and MP_4. For notation MP_m, m is the number of crossed dipole antennas. Fig. 3.4 shows the far–field pattern of MP_2 with different excitation modes noted as MM_1, MM_2, MM_3 and MM_4 which correspond to the distribution type of positive and

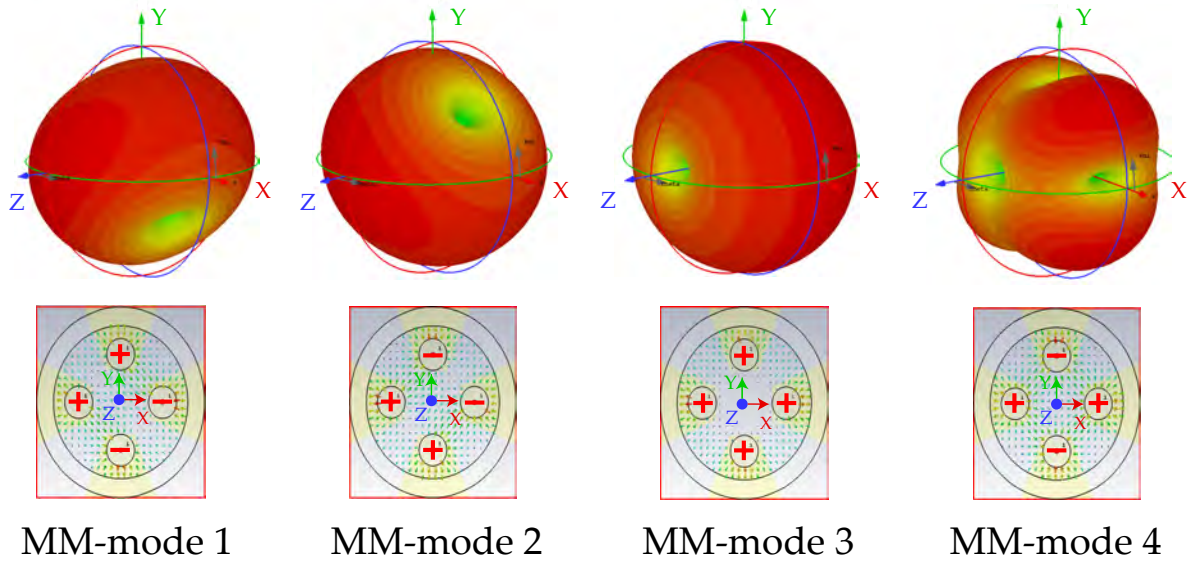

Figure 3.4 – *Multipin approach: Radiation patterns and electric field for difference excitation distribution(MM–mode 1, MM–mode 2, MM–mode 3 and MM–mode 4) for MP_2.*

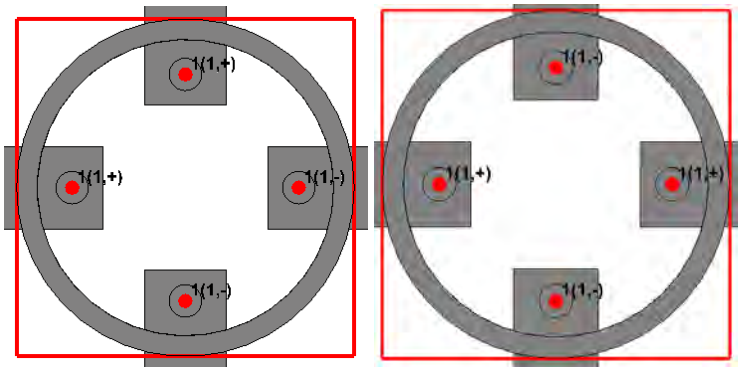

Figure 3.5 – *Excitation modes: Left) MM_1 excitation mode on MP_2. Right) MM_4 excitation mode on MP_2.*

negative pins. Their electric fields are also showed. The mode MM_3 has zero–field along the axis of propagation (z) and the mode MM_4 contains principal multi–lobes, while the MM_1 and MM_2 acts as super dipoles.

At least 2^n excitation modes are possible, where n is the number of dipoles. Each mode has a unique radiated far–field pattern as reported in [162–165]. These results confirm previous work in refs. [163, 164] using the multipin approach. Here, the focus is on the excitation modes noted as MM_1 and MM_4. The MM_4 is mainly used in reference to the spatial distribution of high order Laguerre–Gauss modes as used for dual–frequency laser seen in the previous chapter. These radiation patterns of multipolar antennas show the possibility to spatial multiplexing by changing the excitation type, i.e. switch from MM_1 to MM_4.

In the Figs. 3.5, 3.6 and 3.7, the distribution of positive and negative pins excitation for the modes MM_1 and MM_4 and for each multipolar antennas are showed. MM_1 can be considered as a "super dipole" and thus the realized gain is expected to be double than a classic dipole (excluding the coupling loss).

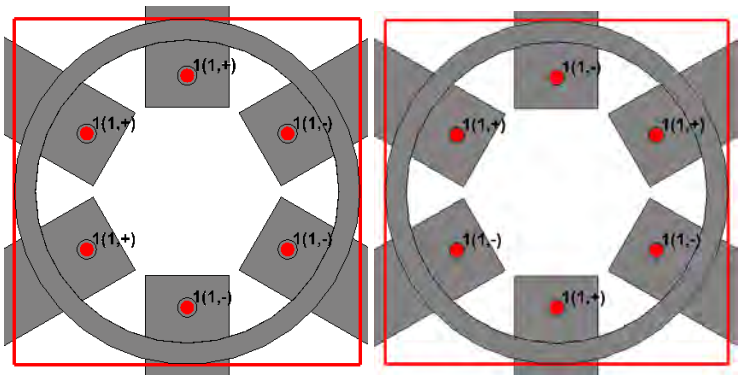

Figure 3.6 – *Excitation modes: Left) MM_1 excitation mode on MP_3. Right) MM_4 excitation mode on MP_3.*

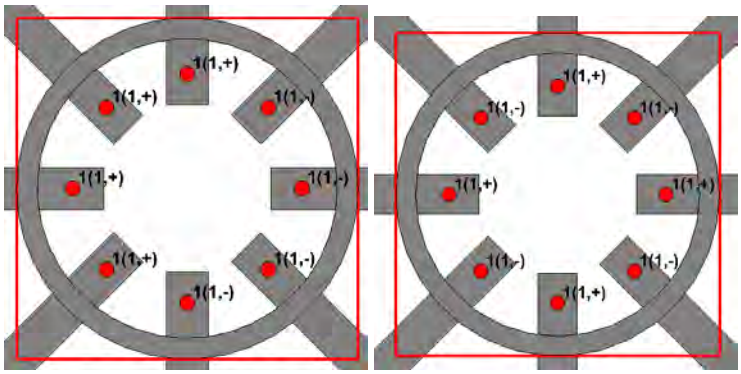

Figure 3.7 – *Excitation modes: Left) MM_1 excitation mode on MP_4. Right) MM_4 excitation mode on MP_4.*

A MP_2, MP_3 and MP_4: S-parameters

Figures 3.8, 3.9 and 3.10 shows the S–parameters for each modes (MM_1 and MM_4) for each multipolar antenna. The length of the arms of the multipolar antennas is varied (between 600 μm to few mm) in order to find the best resonance at 100 GHz. The 100 GHz was initially chosen because of SESAM lifetime but can also used for UTC–PD operating at 100 GHz too. The interest of working at 100 GHz is to demonstrate the proof–of–concept of multipolar antennas then it can be extended to higher frequencies. The first resonance is compared with higher order resonances. The S_{11} parameter results suggest that higher order resonances (R2 and R3) should be used in order to use more efficient multipolar antennas. In fact, the R1 presents at 100 GHz a lower S_{11} value compared to higher order resonances. However, the radiation patterns with design at second and third resonances (R2 and R3) are degraded. This is due to the fact that higher order resonance always give complex pattern associated to the higher modes

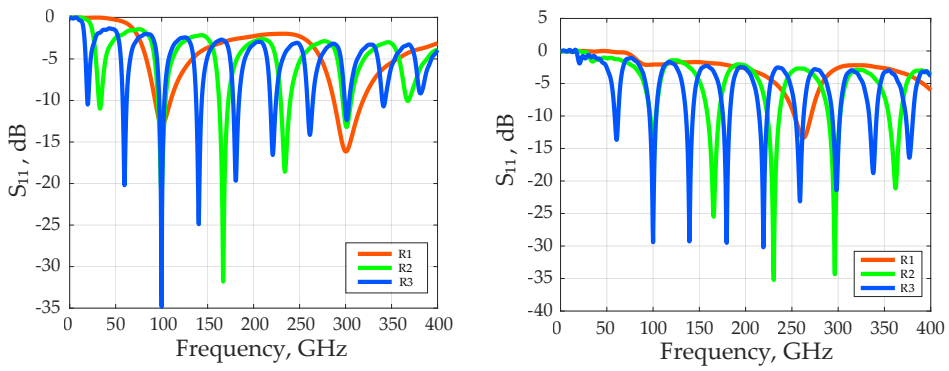

Figure 3.8 – *MP_2: MM_1 (left) and MM_4 (right), S–parameters*

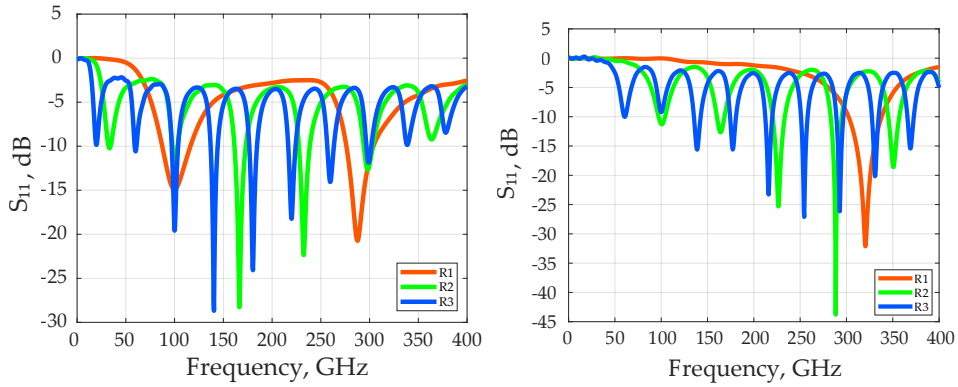

Figure 3.9 – *MP_3: MM_1 (left) and MM_4 (right), S–parameters*

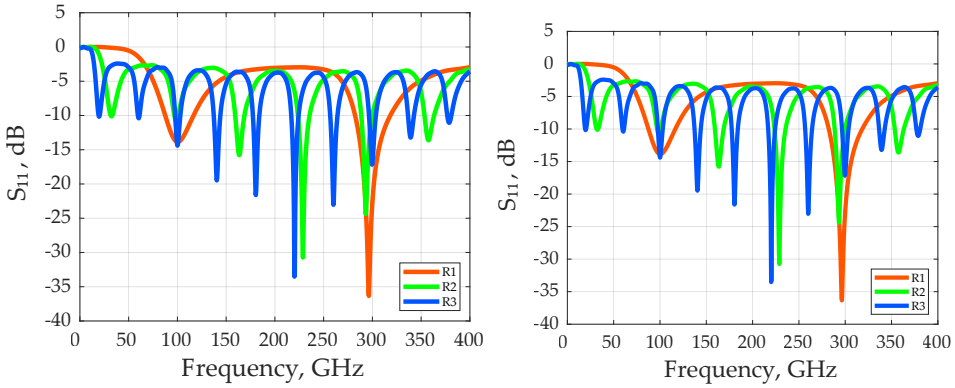

Figure 3.10 – *MP_4: MM_1 (left) and MM_4 (right), S–parameters*

resonances. It is also noted that this is not always extendable (even impossible for MP_4 at first order) to very high resonance order and a compromise need to be found between n resonance (thus the antenna dimension) and the efficiency. The Tables 3.2, 3.3, 3.4, 3.5, 3.6 and 3.7 report the fundamentals parameters of each multipolar antenna for each resonances (R1, R2 and R3).

Table 3.2 – *Key antenna performances: Mode-MM1, R1. Left) 100 GHz. Right) 300 GHz.*

	MP2	MP3	MP4
Rlzd. Gain (dBi)	2.06	1.564	1.2
Bandwidth (GHz)	17.2	29	30.5
Tot. Effic. (dB)	-0.195	-0.77	-1.1

	MP2	MP3	MP4
Rlzd. Gain (dBi)	6.4	3.33	3.43
Bandwidth (GHz)	31.75	27	37.5
Tot. Effic. (dB)	-0.089	-0.114	-0.25

Table 3.3 – *Key antenna performances: Mode-MM1, R2. Left) 100 GHz. Right) 300 GHz.*

	MP2	MP3	MP4
Realized Gain (dBi)	6.58	3.4	3.3
Bandwidth (GHz)	7.6	6.7	4.1
Tot. Efficiency (dB)	-0.06	-0.43	-0.58

	MP2	MP3	MP4
Realized Gain (dBi)	7.1	8.53	7.95
Bandwidth (GHz)	9.21	9.3	11.3
Tot. Efficiency (dB)	-0.22	-0.41	-0.41

Depending on the MM order, the realized gain, directivity as well as the bandwidth are different. By looking on the MM_1 excitation mode, the realized gain decreases at 100 GHz while the bandwidth increases. The directivity in this case remains stable. At 300 GHz, MP_3 has the worst performances in realized gain, directivity and bandwith. As the resonance order increases, the behaviour is different. The R2 at 100 GHz, MP_2 presents the best performances and at 300 GHz,

Table 3.4 – *Key antenna performances: Mode-MM1, R3. Left) 100 GHz. Right) 300 GHz.*

	MP2	MP3	MP4
Realized Gain (dBi)	2.3	7	4.1
Bandwidth (GHz)	5.6	6.6	5.3
Tot. Efficiency (dB)	-2.7	-0.17	-0.33

	MP2	MP3	MP4
Realized Gain (dBi)	4.8	5.3	9.6
Bandwidth (GHz)	5	5.1	7
Tot. Efficiency (dB)	-2.3	-0.44	-0.26

Table 3.5 – *Key antenna performances: Mode-MM4, R1. Left) 100 GHz. Right) 300 GHz.*

	MP2	MP3	MP4
Rlzd. Gain (dBi)	-0.2	-13	-27.2
Bandwidth (GHz)	–	–	–
Tot. Effic. (dB)	-4	-18	-32.4

	MP2	MP3	MP4
Rlzd. Gain (dBi)	4.4	1.08	4
Bandwidth (GHz)	17	35	–
Tot. Effic. (dB)	-0.23	-3.06	-0.63

Table 3.6 – *Key antenna performances: Mode-MM4, R2. Left) 100 GHz. Right) 300 GHz.*

	MP2	MP3	MP4
Rlzd. Gain (dBi)	4	3.3	3.4
Bandwidth (GHz)	6.2	7	–
Tot. Effic. (dB)	-0.24	-0.34	-1.443

	MP2	MP3	MP4
Rlzd. Gain (dBi)	6.8	5.8	4.3
Bandwidth (GHz)	13	12	6.3
Tot. Effic. (dB)	-0.2	-0.034	-0.37

Table 3.7 – *Key antenna performances: Mode-MM4, R3. Left) 100 GHz. Right) 300 GHz.*

	MP2	MP3	MP4
Rlzd. Gain (dBi)	5.9	2.8	4.9
Bandwidth (GHz)	7	–	–
Tot. Effic. (dB)	-0.0035	-0.56	-1.4

	MP2	MP3	MP4
Rlzd. Gain (dBi)	6.7	7.3	5.2
Bandwidth (GHz)	8.2	7.6	6
Tot. Effic. (dB)	-0.13	-0.3	-0.22

the MP_3 shows better results except for the bandwidth. Both MM_1 and MM_4 and for each multipolar antenna, the bandwidth decreases as the resonance order increases. A decrease of a factor between x3 and x5. This is a disadvantage for applications in communication. In terms of efficiency, it differs on the multimode excitation mode. The efficiency values decrease with resonance order on MM_1 excitation mode, while they increase on MM_4.

According to these tables and except the MM_4 R1 case, the multipolar antennas efficiencies are never below -3 dB. This means that the ratio between the realized gain and the directivity are always higher than 50%. To conclude, multipolar antennas present potential exaltation in term of realized gain (from two times to four times), with a reduction of bandwidth while the radiation efficiency remain relatively stable compared to a simple dipole.

B MP_2, MP_3 and MP_4: Impedance input

Figures 3.11, 3.12 and 3.13 show impedance evolution in the Smith chart. They allow to understand how the impedance evolves with the frequency, going to short circuit to open circuit depending on the mode excitation and the multipolar antenna used. For each multipolar antenna, their resonances R1, R2 and R3 show comparable results. However, the difference can be seen with the choice of the modes MM_1 and MM_4. For each multipolar antenna, the MM_1 results do not change significantly. This is due to the fact that MM_1 excitation mode acts as super dipole. However, the MM_4 case results is only dependent on the multipolar antenna used.

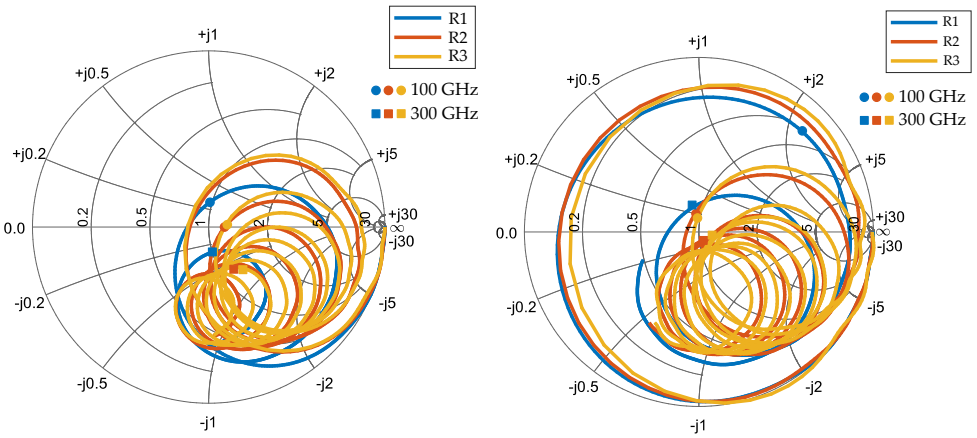

Figure 3.11 – *MP_2 Smith charts. Left) MM_1 for each resonances R1, R2 and R3. Right) MM_4 for each resonances R1, R2 and R3.*

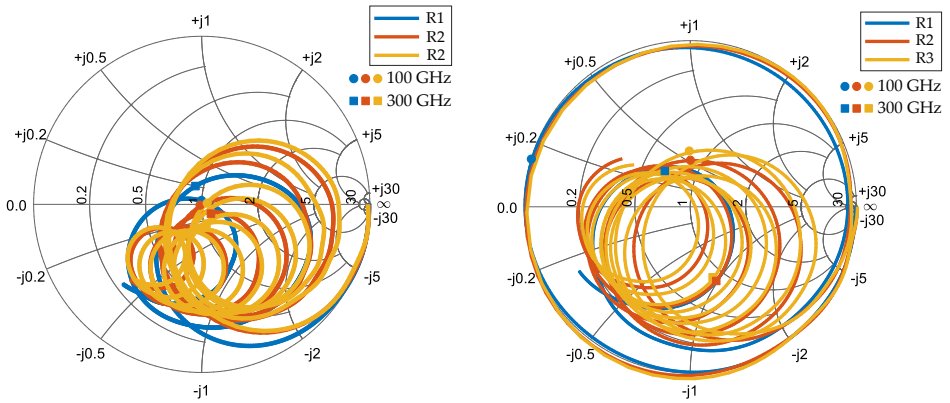

Figure 3.12 – *MP_3 Smith charts. Left) MM_1 for each resonances R1, R2 and R3. Right) MM_4 for each resonances R1, R2 and R3.*

It seems that MP_4 shows better results (mostly near to the center of Smith chart) compared to MP_2 and MP_3.

C MP_2, MP_3 and MP_4: Far-field patterns

Figures 3.14, 3.15, 3.16, 3.17, 3.18 and 3.19 show the far–field radiation patterns for each modes MM_1 and MM_4 for each multipolar antennas at 100 GHz and 300 GHz.

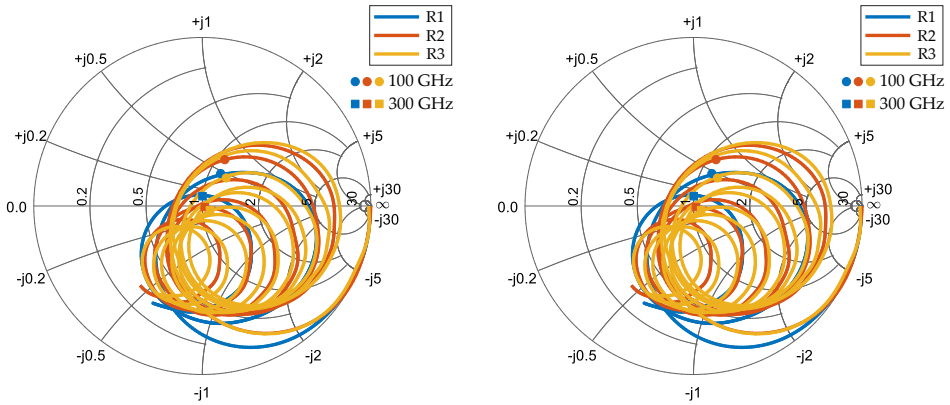

Figure 3.13 – *MP_4 Smith charts. Left) MM_1 for each resonances R1, R2 and R3. Right) MM_4 for each resonances R1, R2 and R3.*

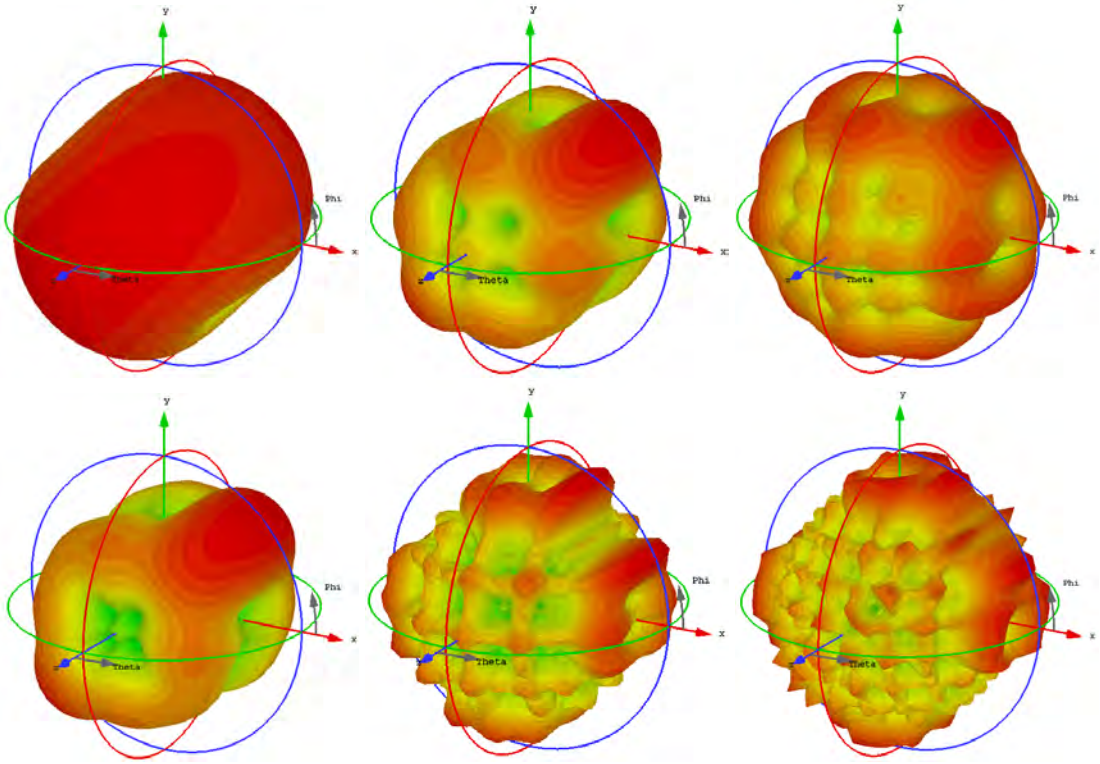

**Figure 3.14 – *Mode–MM1: MP_{02} far–field for* 100 GHz (*top*) *and* 300 GHz (*bottom*) *and for each resonances* (1^{st}, 2^{nd}, *and* 3^{rd}, *from left to right*).

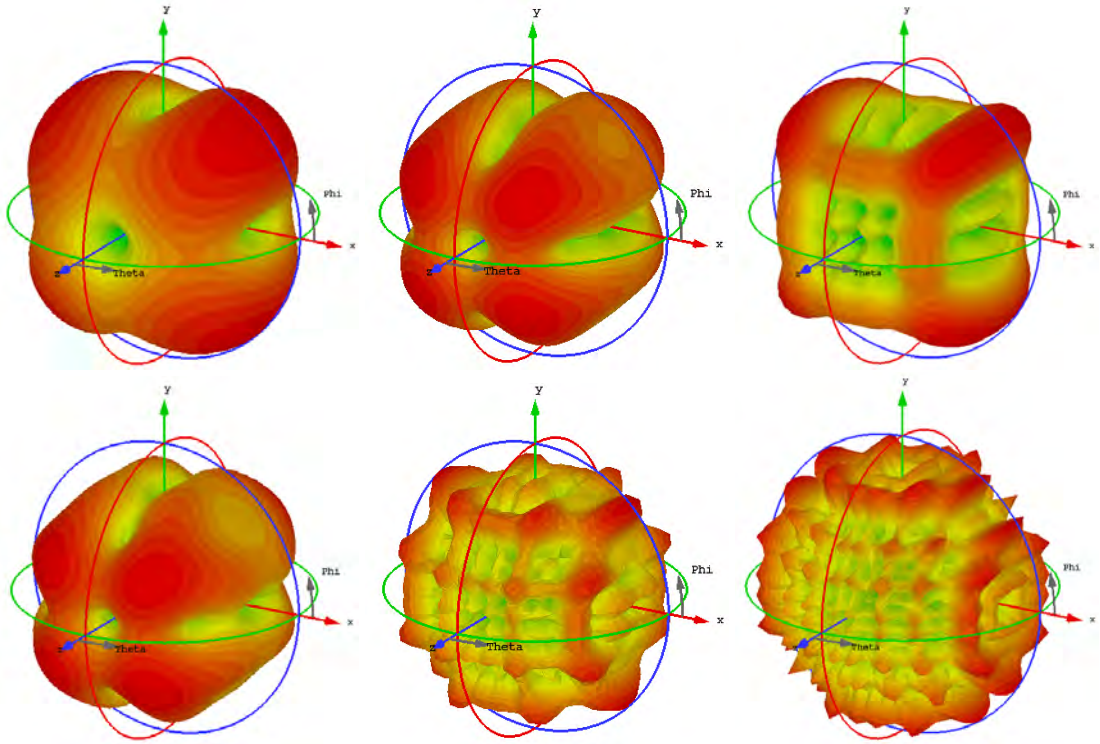

**Figure 3.15 – *Mode–MM4: MP*$_{02}$ *far–field for* 100 GHz (*top*) *and* 300 GHz (*bottom*) *and for each resonances* (1^{st}, 2^{nd}, *and* 3^{rd}, *from left to right*).

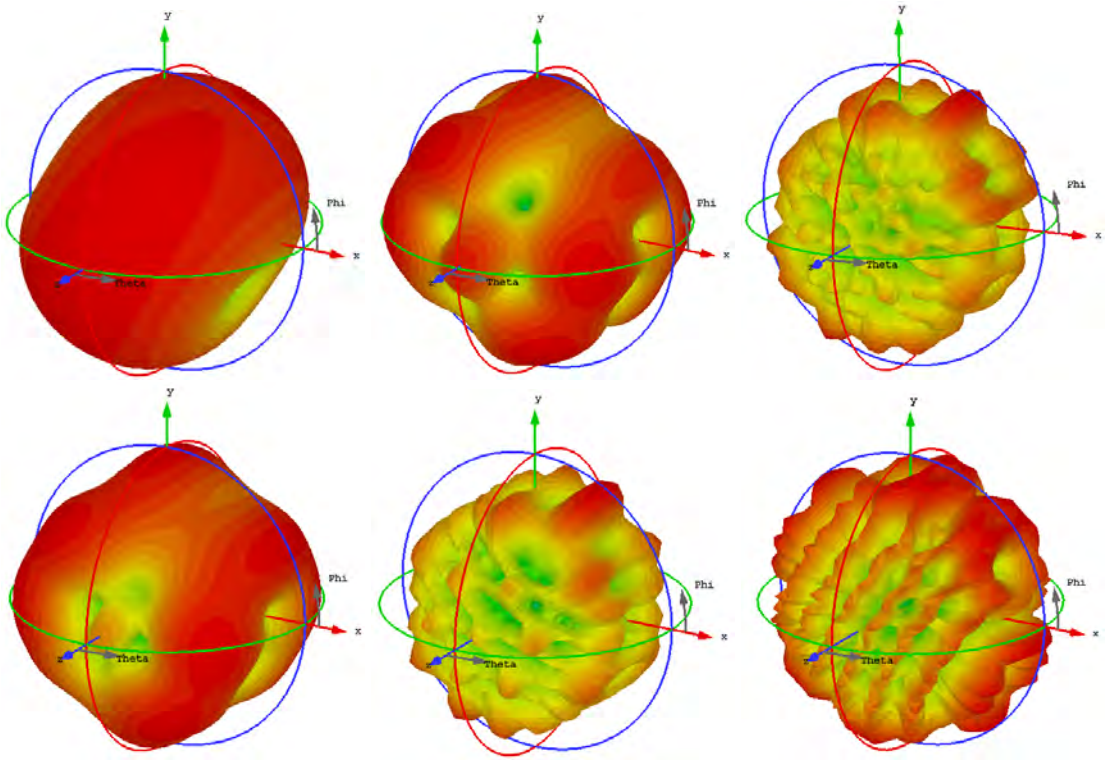

**Figure 3.16 – *Mode–MM1: MP*$_{03}$ *far–field for* 100 GHz (*top*) *and* 300 GHz (*bottom*) *and for each resonances* (1^{st}, 2^{nd}, *and* 3^{rd}, *from left to right*).

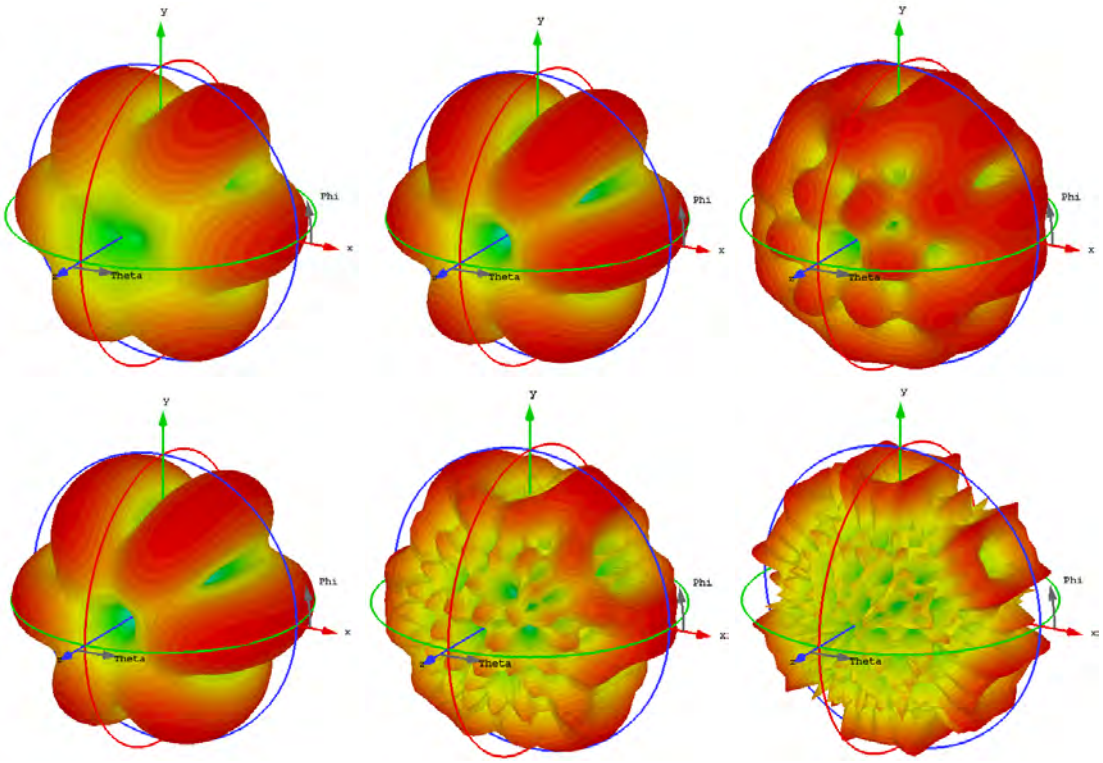

Figure 3.17 – *Mode–MM4: MP*$_{03}$ *far–field for* 100 GHz (*top*) *and* 300 GHz (*bottom*) *and for each resonances* (1^{st}, 2^{nd}, *and* 3^{rd}, *from left to right*).

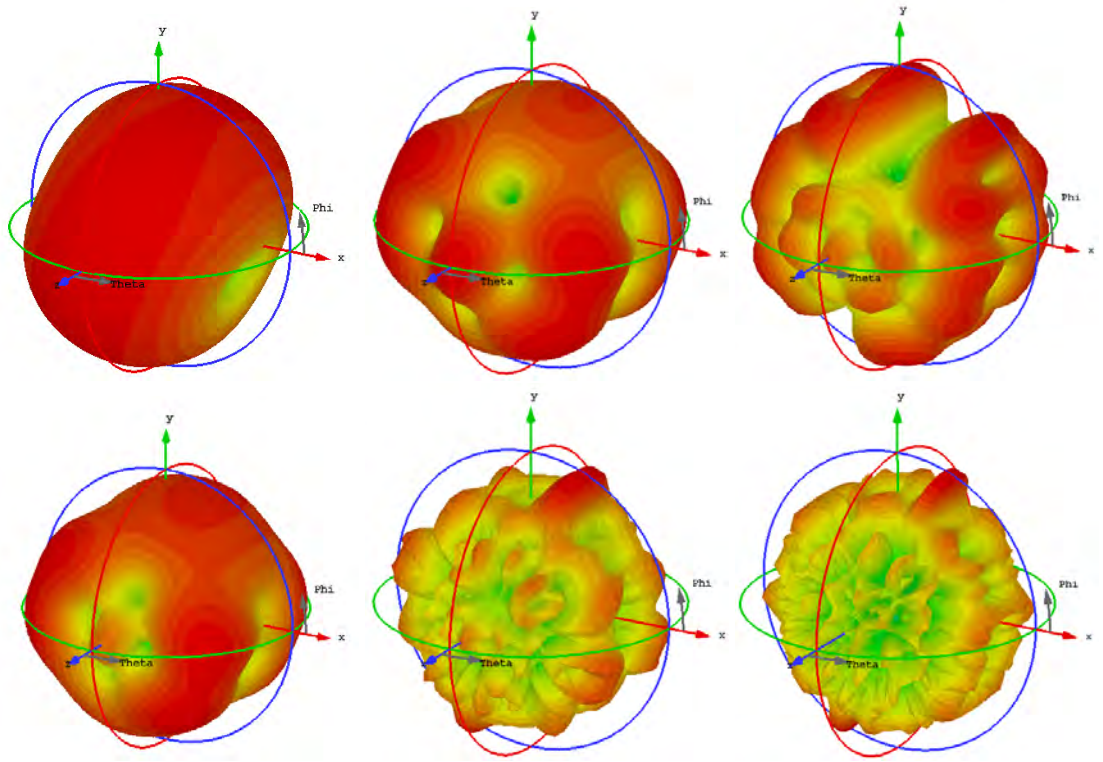

Figure 3.18 – *Mode–MM1: MP*$_{04}$ *far–field for* 100 GHz (*top*) *and* 300 GHz (*bottom*) *and for each resonances* (1^{st}, 2^{nd}, *and* 3^{rd}, *from left to right*).

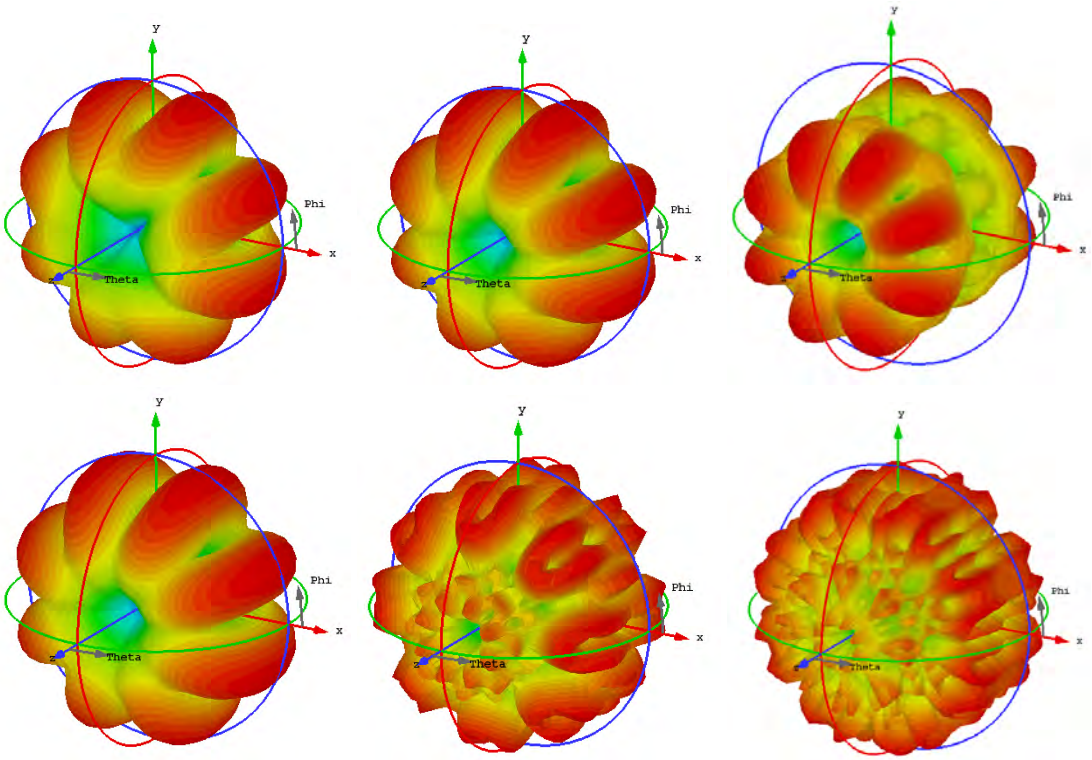

**Figure 3.19 – *Mode–MM4: MP_{04} far–field for* 100 GHz (*top*) *and* 300 GHz (*bottom*) *and for each resonances* (1^{st}, 2^{nd}, *and* 3^{rd}, *from left to right*).

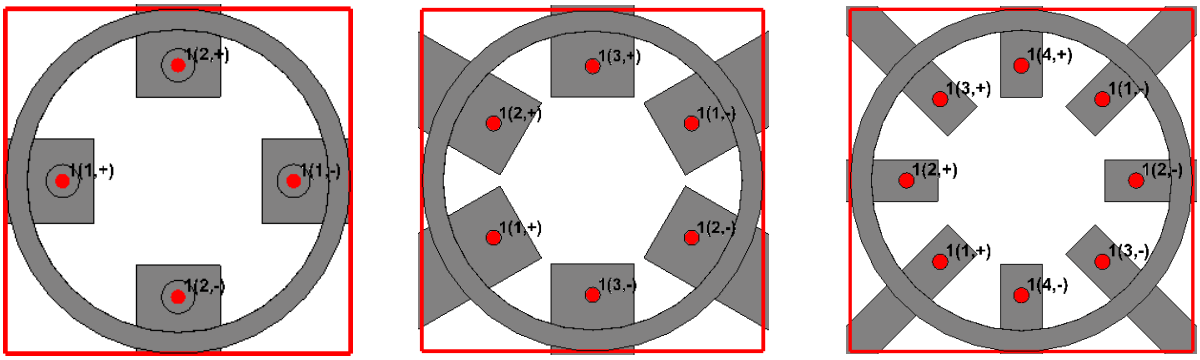

Figure 3.20 – *MP_2, MP_3 and MP_4 showing the pins excitation for coupling study. For a common incoming port excitation, each dipole has a unique differential mode excitation numerated 1, 2, 3 and 4 depending on the number of crossed dipoles.*

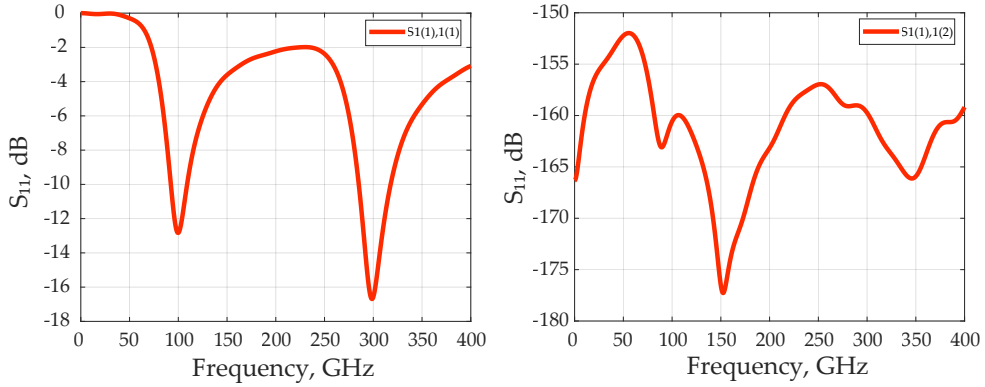

Figure 3.21 – *S_{11} parameters results of MP_2. Left) S1(1),1(1) parameter of two crossed dipoles. Right) S1(1),1(2) parameter can be seen as a transmission between adjacent arms.*

On the top of each figures are radiation pattern operating at 100 GHz while on the bottom of each figures are radiation pattern operating at 300 GHz. As the resonance order is increased (R3), the radiation pattern is more complex and diffractive. For each multipolar antenna under MM_1 excitation, the beam begins with a donut–like shape (super dipole) and then it diffracts when the resonance order increases. And under MM_4, the beam begins with a multi–lobe shape corresponding to the number of the crossed dipoles. Then, the beam diffracts.

D MP_2, MP_3 and MP_4: Coupling between crossed dipoles

To study the coupling between crossed dipole antennas, independent excitation modes called differential modes must be applied for each dipoles as seen in the Fig. 3.20. By applying differential modes, it is thus possible to quantify the coupling between crossed dipole antennas. Under the same waveguide port excitation (port 1), the S–parameters are called differently. For example, for the MP_2, the S1(1),1(1) (pins noted 1(1,+) and 1(1,-)) parameter is the S_{11} parameter of the dipole along x–axis while the S1(2),1(2) (pins noted 1(2,+) and 1(2,-)) is the the S_{11} parameter of the dipole along y–axis. For each multipolar antennas, there are 2, 3 and 4 differential modes to be applied (as seen in the Fig. 3.20). Figures 3.21, 3.22, 3.23 display S–parameters results for each multipolar antenna. They are plotted as function of frequency (from 0 to 400 GHz).

For each figures (left), the reflection coefficient presents two resonances: the first one around

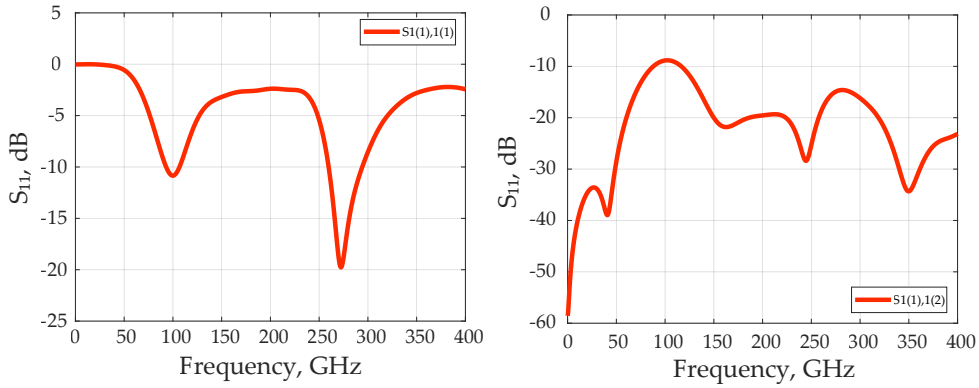

Figure 3.22 – *S_{11} parameters results of MP_3. Left) S1(1),1(1) parameter of three crossed dipoles. Right) S1(1),1(2) parameter can be seen as a transmission between adjacent arms.*

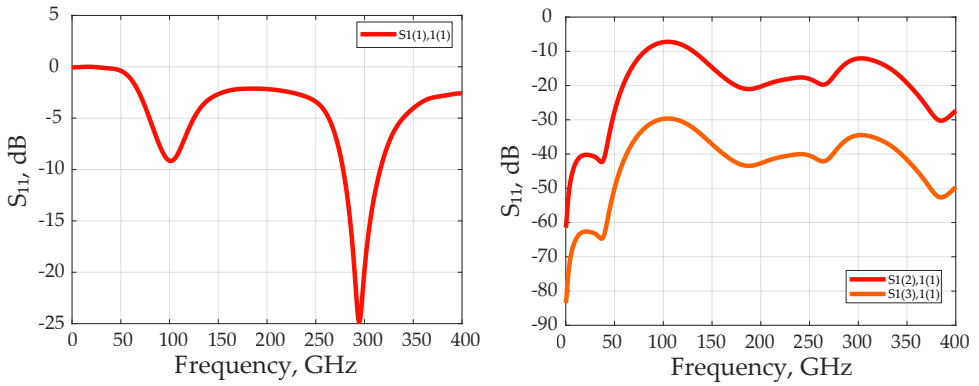

Figure 3.23 – *S_{11} parameters results of MP_4. Left) S1(1),1(1) parameter of four crossed dipoles. Right) S1(2),1(1) parameter can be seen as a transmission between close arms and S1(3),1(1) a transmission between distant arms.*

100 GHz and the second one at around 300 GHz. The first resonance is gradually degraded when the number of crossed dipoles increases, while the second resonance is gradually enhanced. For MP_2 the results show very low coupling effects (at around -165 dB) while in the other multipolar antennas the coupling effects is predominant (at around -20 dB) and for MP_4 antenna (around -40 dB). These coupling effects strongly affect the antenna radiation efficiency. In the Fig. 3.21, the S1(1),1(1) and S1(2),1(2) parameters are the results of the two crossed dipoles studied independently. Their radiation patterns are showed in the Fig. 3.24. The maximum of the radiation pattern in the left is along y–axis while the maximum of the radiation pattern in the right is along the x–axis. Their maximum values (realized gain) are reported in the Table 3.8. Their realized gains are equal and thus the coupling is extremely low (as seen in the Fig. 3.21

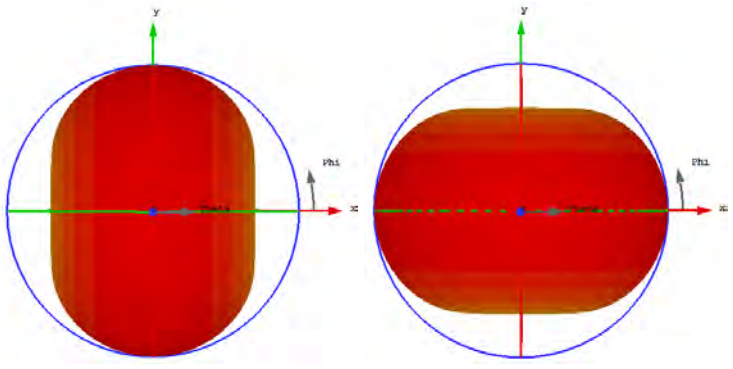

Figure 3.24 – *MP_2: independent far–field of two crossed dipoles.*

Table 3.8 – *Comparison in terms of realized gain between MP_2, MP_3 and MP_4.*

	MP2	MP3	MP4
Realized Gain at 100 GHz (dBi)	2.043	0.9122	-0.3431
Realized Gain at 100 GHz (dBi)	2.043	0.8182	-0.7968
Realized Gain at 100 GHz (dBi)	–	0.6705	-0.6804
Realized Gain at 100 GHz (dBi)	–	–	-1.160

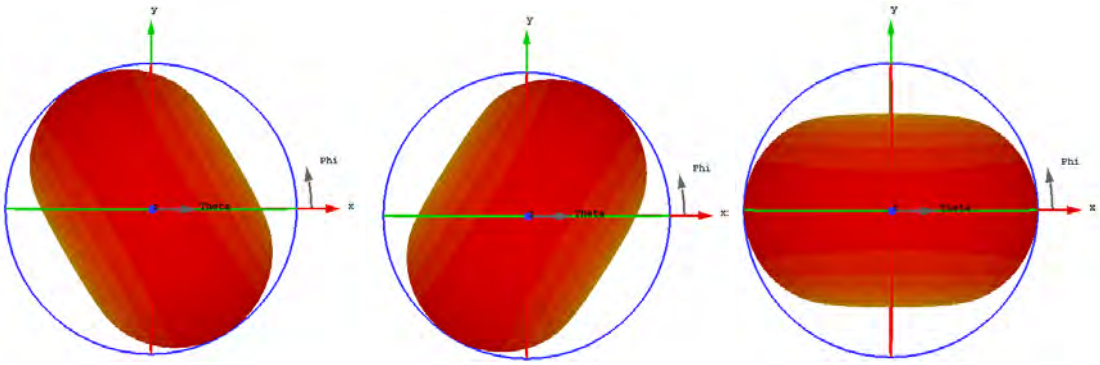

Figure 3.25 – *MP_3: independent far–field of three crossed dipoles.*

in the right). S1(1),1(2) and S1(2),1(1) can be seen as a transmission between two orthogonal modes. The fact that the two dipoles are orthogonal, their coupling effect is practically null. According to these results, the MP_2 has a similar performance than a classic dipole (without taking account the loss when using the multipin port).

The coupling effects appears really from the MP_3. In the Fig. 3.22 right, the S1(1),1(1), S1(2),1(2) and S1(3),1(3) parameters correspond to the crossed dipoles and present results similar to those of MP_2. However, due to stronger coupling between 3 differential modes (as seen in the same figure in the right), there is an energy transfer between the adjacent resonances. In this case, the resonance at 100 GHz of MP_3 is lower than the resonance at the same frequency of MP_2. Fig. 3.25 shows the evolution of the radiation pattern for each independent dipole for the MP_3 configuration. In this case, the realized gains reported in the Table 3.8 are now different for each independent dipole and lower compared to the MP_2 realized gains.

Finally, for the last multipolar antenna MP_4, Fig. 3.23 presents similar results compared to MP_3. Even in this case, the resonance at 100 GHz of MP_4 is lower than the resonance at the same frequency of both MP_2 and MP_3. But, the resonance at 300 GHz of MP_4 is higher than the resonance of both MP_2 and MP_3 at the same frequency. The S2(1),1(2) is transmission result from a dipole to another dipole. But, coupling between distant arms is due to the transmission of S1(3),1(1) and their values are significant to degrade the antenna realized gain reported in the Table 3.8. Far–fields of each dipoles of MP_4 are shown in the Fig. 3.26. The increase of the number of dipoles degrades the performance of each individual dipoles in terms of realized gain. Here again, the coupling becomes stronger with the number of crossed dipoles. In fact, for MP_2 the realized gains of two dipoles are equal because the coupling is very low between two orthogonal dipoles. However, for MP_3 and MP_4, the presence of non–orthogonal dipoles affects their individual performances.

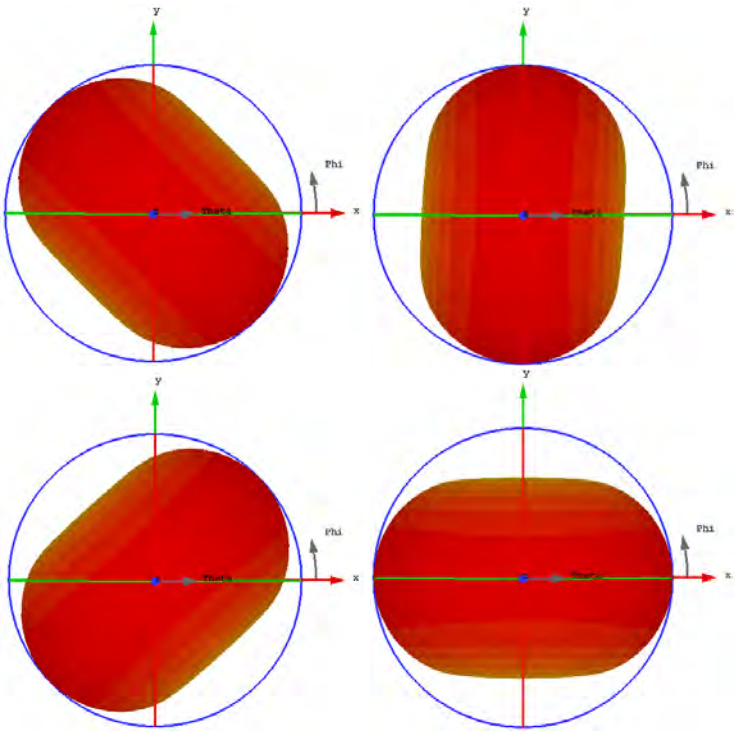

Figure 3.26 – *MP_4: independent far–field of four crossed dipoles.*

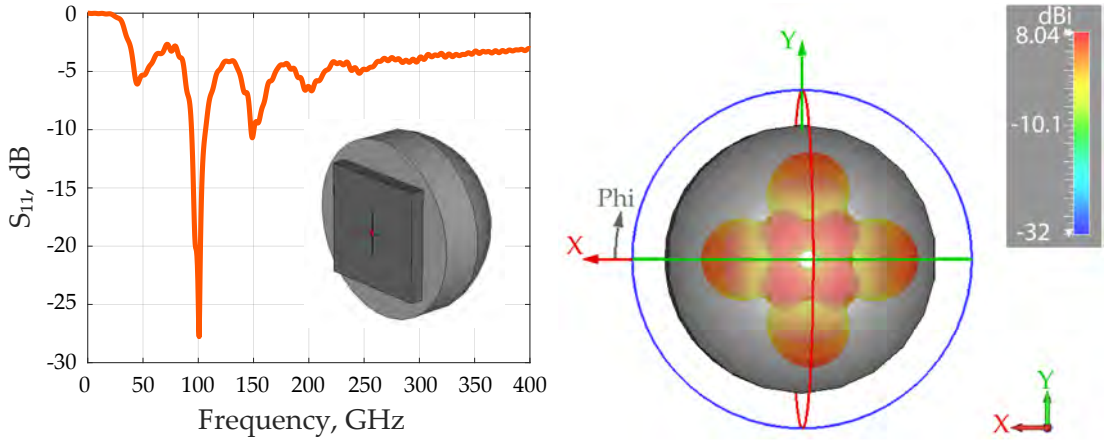

Figure 3.27 – *MP S–parameters: Left) S_{11} parameters of MP_2. Inset: MP_2 with a Si–lens. Right) Far–field result of MP_2 at* 100 GHz.

E MP_2: Performances with Si–lens

All the simulation performed previously were obtained using a permittivity of the vacuum or air in order to study the antenna performance alone. To approach the reality, simulations using a hyper–hemispherical Si–lens (8 mm diameter with an additional 1.8 mm length in order to avoid parasitic FP and quasi–collimate the generated wave) are useful to quantify the realized gain of the multipolar antennas. As an example, the MP_2 is picked up using MM_4 excitation mode (design at first resonance R1). In the Fig. 3.27 (left), the S_{11} is plotted as function of frequency. It shows a good resonance reaching about -27 dB at around 100 GHz. Fig. 3.27 (right) illustrates the far–field at 100 GHz at the output of the Si–lens. The beam of MP_2 is similar to the beam of the same antenna simulated in free space. So, there is a negligible impact on the beam shape using a lens. The realized gain is enhanced by 4 dB using a Si-lens, as seen in the Fig. 3.27 (right) (passing from 4.4 dBi (without Si–lens) to 8.04 dBi (with Si–lens)). In fact,

the Si–lens forces the beam of the multipolar antenna to be more directive and thus the realized gain of the MP_2 is enhanced. The antennas parameters are given in the Appendix A.

3.3 Summary

Dipole and multipolar antennas operating at 100 GHz are designed and analyzed. A comparison of two types of excitation is showed. A comparable performance between multipin port and discret port for a same dipole design is reported. The multipin port is more adapted to the study of multipolar antennas since this approach can be seen as LG transverse modes excitation from the dual–frequency laser. The modes MM_1 and MM_4 for each multipolar antenna MP_2, MP_3 and MP_4 were used for the simulation of multipolar antennas. The results showed a decrease of radiation efficiency when the number of arms increases. This also depends on the mode excitation type (MM_1 and MM_4).

Despite the low efficiency of these antennas, an application could be found in wireless communication. As an example, by considering MIMO technology, 4×4, 6×6 and 8×8 channels can be utilized to transmit high data rate at THz frequencies [166, 167]. A preliminary work was done by a previous PhD student from Lille University on fabricating an UTC array with crossed dipole antennas (MP_2 like multipolar antenna) in order to increase the THz power and the capacity in THz bands [168]. This study has shown that if 4 (or more) powerful UTCs are placed in the center of a multipolar antenna and working at 300 GHz each, the transmission bandwidth would be increased to at least 1.2 THz with many other advantages (such polarization diversity and beam–steering).

Chapter 4

Photomixers for THz Generation

Introduction

Photoconductive THz sources are widely used for spectroscopy, imaging, and sensing [7]. To generate THz waves, a photoconductive antenna is typically illuminated by a femtosecond laser (pulsed regime) or a photomixer by a dual–frequency laser (CW regime) operating at $800\ \mathrm{nm}$ or $1550\ \mathrm{nm}$ [94, 169]. Femtosecond (fs) lasers are often expensive and bulky, so CW dual–frequency lasers are more attractive for portable systems but are more challenging in term of stability as the two beating modes can suffer from modal competition. In terms of operation wavelength, almost no photomixers operating at $1064\ \mathrm{nm}$ were reported, except in Ref. [97, 118, 170], despite the availability and maturity of optical components and high–power lasers at this wavelength. In this chapter, a coherent, compact, tunable and stable CW DF–VeCSEL [118, 160] with a semiconductor saturable absorber mirror as photomixer or a plasmonic–based photomixer [5], all operating at $1064\ \mathrm{nm}$ for CW THz generation, are combined. So, two exploratory research strategies are engaged. The first one aims to demonstrate the feasibility of using SESAM–based devices as photomixers for CW THz generation. This includes the fabrication done in the clean room of University of Montpellier and I–V characterization. The second one aims to demonstrate THz emission by using plasmonic–based devices designed and fabricated by UCLA collaborators. With the latter device, THz emission was successfully achieved at room temperature in a CW regime.

4.1 Semiconductor saturable absorber mirror (SESAM)

SESAM are semiconductor devices and are principally used to mode–lock lasers [171–178]. This semiconductor device has a distributed Bragg reflector (DBR) in the bottom and a quantum well in the top, near the surface of the device as described in Fig. 4.1 (left).

4.1.1 SESAM as photomixer?

SESAM is studied, for the first time, as a potential photomixer for CW THz generation and this for a number of reasons:

1. **Micro–cavity.** Technically, SESAM device used as photomixer detains a better efficiency thanks to the $\mu\mathrm{m}$–cavity effect. In fact, the light that is not absorbed by the QW during the first trip is reflected by the DBR and then absorbed again by the QW thus increasing

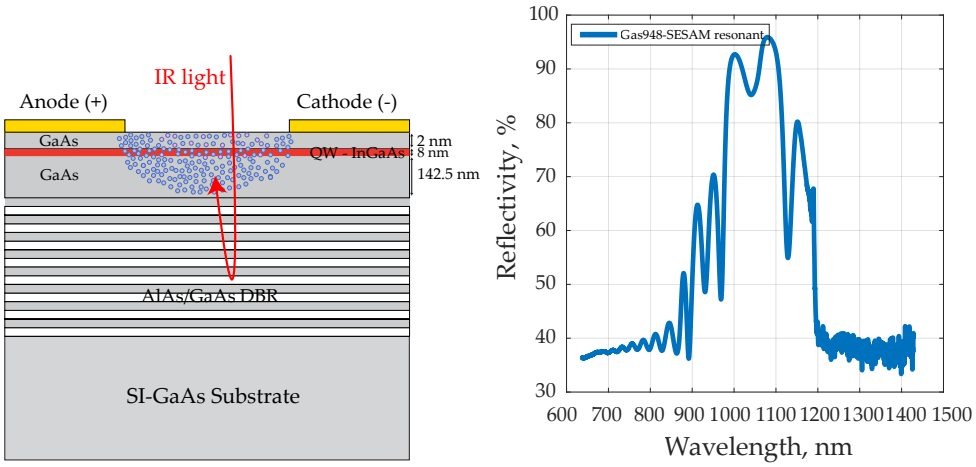

Figure 4.1 – *SESAM structure: Left) SESAM structure contains a SI–GaAs substrate, AlAs/GaAs DBR, and InGaAs/GaAs QW. The electrodes anode (+) and cathode (-) are used only for photomixing devices, otherwise there is no electrode. Right) Reflectivity as a function of wavelength for the SESAM (Gas948).*

effective absorption. The incident wavelength should be within the working stop–band to be absorbed by the QW, otherwise the light will be not absorbed or reflected.

2. **Lifetime.** Since the QW is placed close to the surface, the photocarriers recombines on the SESAM surface with a surface recombination time of ~ 20 ps. Thanks to the fast surface recombination time, the bandwidth should covers sub–millimeter frequencies.

3. **Resistance.** No information is available about the resistance of SESAM devices in the literature, therefore TLM studies will be conducted to evaluate this resistance.

4.1.2 Devices fabrication processes

A SESAM

The SESAM devices (Gas948) used in this thesis were designed by A. Garnache from Photera group and fabricated by I. Sagnes *et al.* from Centre for Nanoscience and Nanotechnology (C2N), Palaiseau. It contains an 8–nm $In_{0.23}Ga_{0.77}As$/GaAs quantum well, grown at 735°C by MOCVD, designed at 1060 nm and placed at 2 nm from the air interface. It was grown on the top of an AlAs/GaAs Bragg mirror [136]. The absorption was expected to be roughly 7% at room temperature. In the Fig. 4.1 (right), reflectivity as a function of wavelength for the SESAM is showed. A high reflectivity is achieved around the wavelength of interest. It is important to note that the valley around 1064 nm is due to the QW absorption.

B Transmission Line Measurement (TLM)

For TLM purposes, contacts were added at the Central Technologique de Montpellier (CTM) using standard photolithography which offers resolution of several micrometers to hundreds of nanometers. More information can be found in references [180, 181]. The process flow for TLM fabrication on SESAM device consists of the following steps described in Fig 4.2:

1. **Substrate preparation:** the sample are inspected by optical microscopy, and they are successively cleaned in acetone (2 min.) and ethanol (2 min.), rinsed with isopropanol (2 min.) and dried under nitrogen flow.

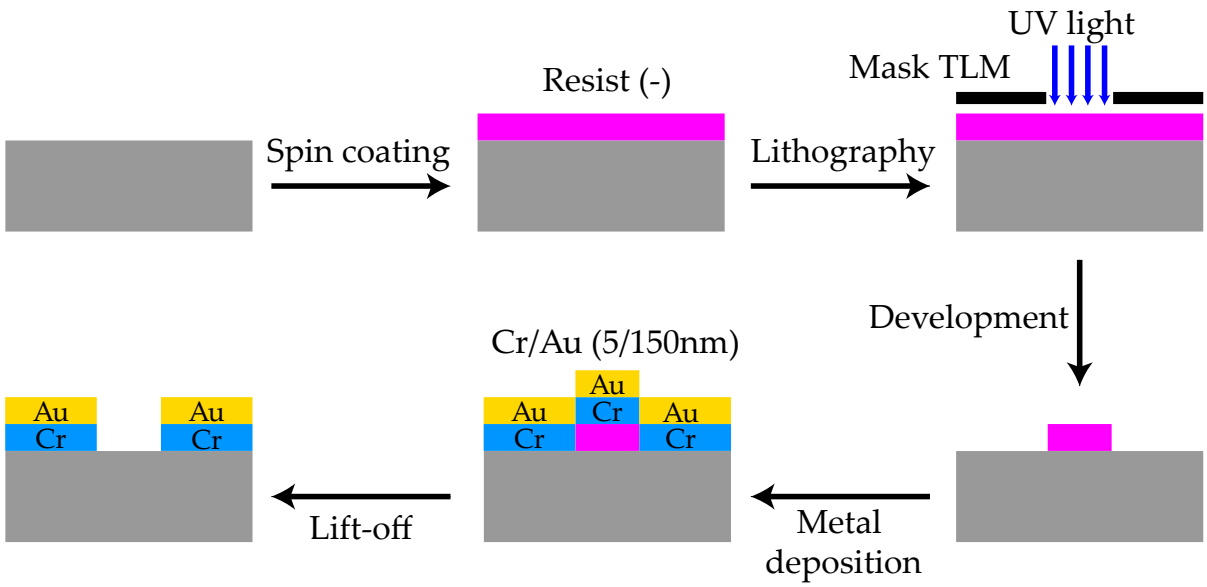

Figure 4.2 – *Simplified process flow for the TLM sample fabrication. A. Substrate preparation. B. Photoresist deposition. C. Photolithography. D. Development. E. Metal deposition. F. Lift–off.*

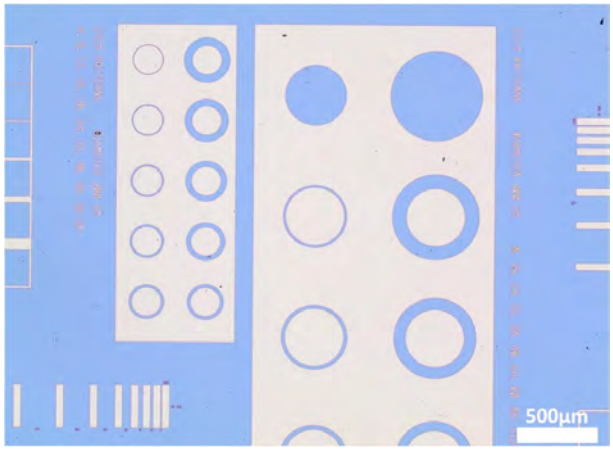

Figure 4.3 – *Circular and rectangular patterns. The latter one was used to characterize the SESAM device. Figure taken from* [4].

2. **Photoresist deposition:** the samples are dehydrated on a hotplate at 120°C for 1 min., to avoid pollution and evaporate liquid residues. The samples are then covered with AZ 5214E photoresist, spread and spun at 4000 rpm for 30 s with 2 s acceleration ramp. Then, the sample is baked during 1 min. at 120° C.
3. **Photolithography:** the mask E256–L3 of Nanomir group with different TLM patterns is used. Circular and rectangular patterns (Fig. 4.3) were fabricated but only rectangular ones were used. To bring the sample and the mask in closest contact, a vacuum contact mode is applied. The resist is exposed during 7 s to UV exposure using a Karl Süss MJB4 mask aligner. Then, a reversal bake is applied during 1 min. at 120°C.
4. **Resist development:** the photoresist is then developed during 1 min. using AZ 726–MIF developer.
5. **Metal deposition:** a layer of chrome of 5 nm thickness is deposited which acts as an adhesive layer on the semiconductor and then a layer of gold of 150 nm is also deposited. It has been demonstrated that Cr/Au contacts have better performances in terms of THz power (50% higher) than Ti/Au contacts [182].

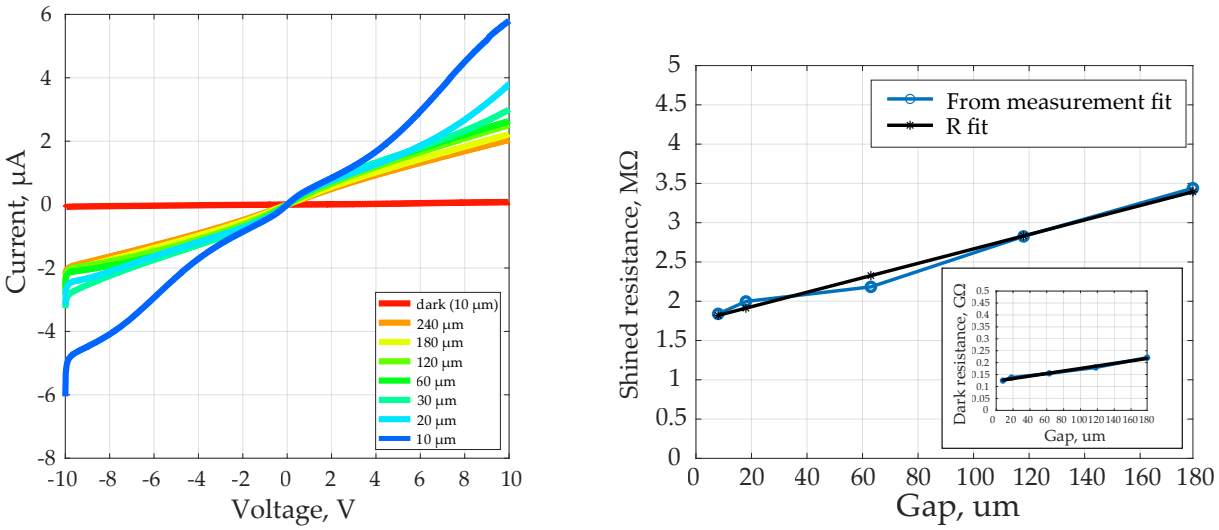

Figure 4.4 – *Optical characterization: Left) Photocurrent as function of bias voltage for different gap. Right) Shined resistance of the SESAM as a function of the gap length, measured at* 10 V. *Inset: Dark resistance of the SESAM as a function of the gap length.*

6. **Lift–off:** during this process, the AZ 5214E photoresist and the metal deposited are removed by using a bath of acetone.
7. **Final cleaning:** the TLM sample is successively rinsed with acetone, ethanol, isopropanol and dried under a nitrogen flow.

The SESAM-TLM devices are glued onto a TO–8 chip by using a lacquer, a cold welding usual technique for attaching metal pieces. Then, the metal grooves on the SESAM device are bonded to the TO–8 pins connected to coaxial cables.

4.1.3 Optical and electrical characterization

A White light excitation

This section describes primary opto–electronic characteristic of the SESAM using white light excitation. Further studies will use excitation at 1064 nm, i.e. the design wavelength. These results were obtained in clean room using probes and a source measure unit (SMU, Keysight B2902A) to apply a bias voltage and at the same time measure the photocurrent. A microscope was used to set down the probes. The light source, a 150–W ($\sim$ 3200 K) fiber optic illuminator, was integrated in the microscope and kept at distance of a few cm from the sample to ensure moderate excitation. The white light beam excites (mostly) GaAs layers. Figures 4.4 show photocurrent as a function of bias voltage for different gaps as well as the evolution of the resistance of the device (including contacts). As first observation, the SESAM responds to the white light as expected, due to GaAs energy gap. The evolution of the photocurrent with the bias voltage (from -10 V to 10 V) is almost linear and this is obtained without annealing process. About ~ 6 µA is achieved with a gap of 10 µm at 10 V while the dark (photo)current, for the gap 10 µm, is $\sim$ 90 nA at 10 V. At low bias voltage, the current increases linearly with the gap length. In fact, the resistance as seen in the Fig. 4.4 on the right, shows fit (linear fit) as function of gap length. The resistances values are calculated by applying the Ohm law at 10 V, with the hypothesis that the resistance is linear with the gap length (according to [97]). The dark resistance is $\sim$ 100 MΩ and the resistance values drops to a few MΩ with white light excitation. To conclude,

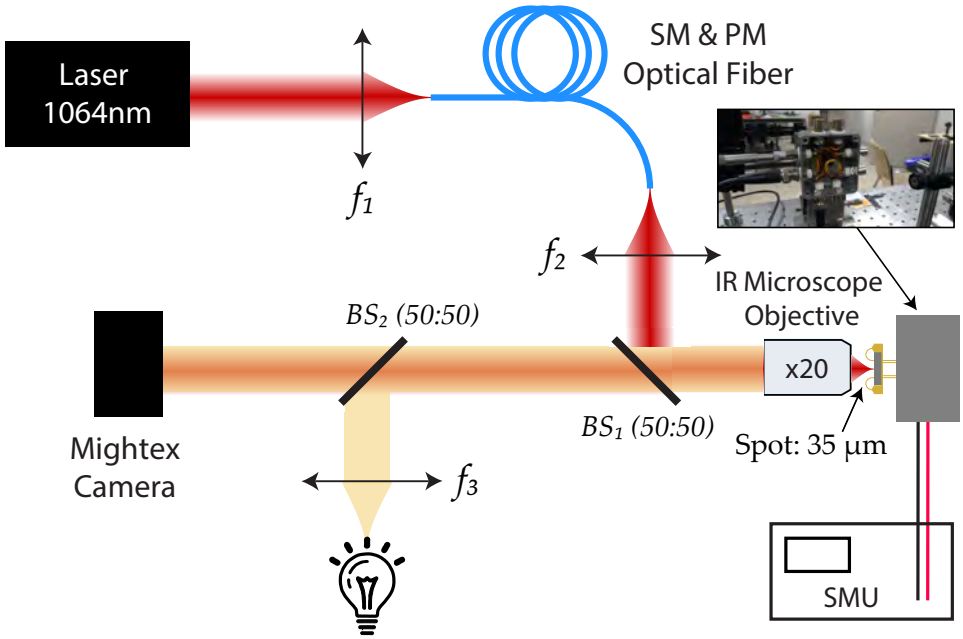

Figure 4.5 – *Experimental setup for I–V characterizations of SESAM device.*

the SESAM reacts well to the white light.

B IR laser excitation

Even if the SESAM responds well to the white light this type of excitation is not adequate for photomixing process and thus a laser operating at $1064\ \mathrm{nm}$ is needed to check the photoconductivity of the SESAM at its designed wavelength. To better evaluate the photoconductivity and the responsivity, the device is tested using several length (TLM). A TLM mask with selected values was available in the clean room at that time and used it for this research. The device was illuminated using a commercial laser (CNI Laser MIL–III–1064), operating at a center wavelength of $1064\ \mathrm{nm}$ with a maximum optical power of $\sim 160\ \mathrm{mW}$. The laser spot was firstly injected into a PM & SM optical fiber using a lens with a focal length of $\mathrm{f_1} = 8\ \mathrm{mm}$ in order to have a clean spatial beam spot and maintaining the desired polarization as shown in Fig 4.5. Then, the collimated laser beam ($\mathrm{f_2} = 20\ \mathrm{mm}$) is injected onto a $20\times$ IR microscope objective in order to achieve a small spot and to excite the SESAM device, between two metallic contacts. The dc bias was supplied by a SMU from Keysight using coaxial cables, which was also used to monitor the dc current flowing in the device while applying the bias voltage. The current was limited by a compliance of $100\ \mu\mathrm{A}$, to avoid the destruction of the device owing to heating effects. An imaging setup using a collimated ($\mathrm{f_3} = 60\ \mathrm{mm}$) fiber optic illuminator (Euromex LE.5210 100W halogen) and a CMOS–based camera (Mightex[1]) was also implemented in order to check the position of the laser beam spot compared to the position of the metallic contacts (Fig. 4.6).

The characterizations were obtained during the M2 internship of Elfady Vita [183]. On the left of Fig. 4.7, the photocurrent is linear as function of bias voltage (at $5\ \mathrm{mW}$) if $\mathrm{V} < 0.5\ \mathrm{V}$ for three different gaps ($240\ \mu\mathrm{m}$, $180\ \mu\mathrm{m}$ and $120\ \mu\mathrm{m}$) and then a saturation is observed. This behavior at higher voltage might be attributed to the electron speed saturation but this is still

1. These cameras have a $5\ \mu\mathrm{m}\times 5\ \mu\mathrm{m}$ pixels resolution.

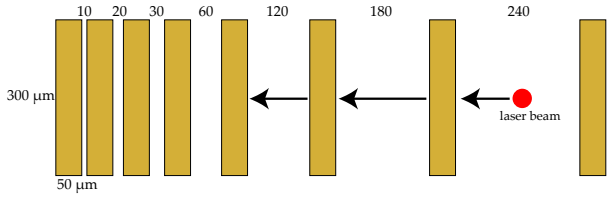

Figure 4.6 – *TLM with beam spot.*

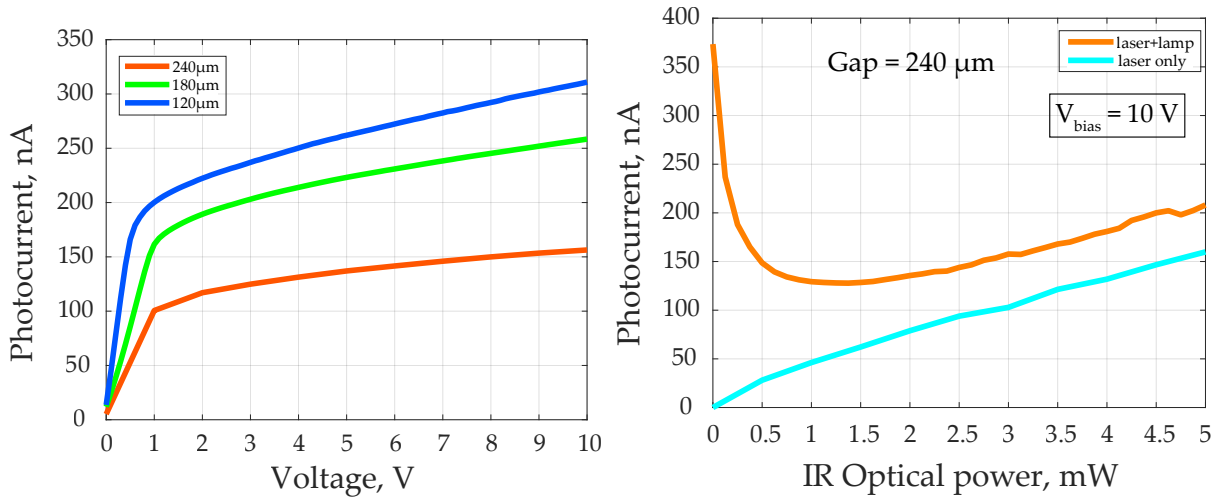

Figure 4.7 – *Optical characterization: Left) I–V characteristic SESAM TLM at* $P_{opt} = 5$ mW *at* 5 V *near the anode. Right) Photocurrent in function of optical power at* 10 V*, with and without the presence of deleterious white light.*

under investigation. On the right of Fig. 4.7, an unusual behavior of the photocurrent evolution when the lamp light is combined with the laser light (at low IR optical power) level is showed (at 10 V). In fact, the effect of the light lamp is stronger when the laser light is completely off. Then, when the IR laser power increases, the lamp light (solid red) power begins to follow the evolution of the IR laser power (solid blue). The initial high photocurrent (laser+lamp) and then the decrease within the first IR optical power (0 to 1.5 mW) is not yet understood but when the laser only is used the photocurrent increases linearly as expected achieving 150 nA at 5 mW at 10 V. During experiments, the lamp light should be off to avoid these deleterious effects.

Fig. 4.8 shows the comparison of the resistance between dark and laser light for different gaps (240 µm, 180 µm and 120 µm). For the dark case, the resistance values are in the GΩ–level range. While, under the laser light (5 mW), the resistance values are in the MΩ–level range. The resistance values are obtained by applying Ohm law at 0.1 V (linear regime) of the Fig. 4.7. Therefore, a decrease factor of ×1000 of the resistance under the laser light is observed. Linear extrapolation is used to anticipate the possible value of the resistance (dark) of the SESAM when the gap between the electrodes is 5 µm. An estimation of a resistance of about 0.3 GΩ which led to a resistivity of 60 Ω cm is proposed by applying a Ohm law and using a linear extrapolation. This would also lead to an estimated dark photocurrent of 5 nA. The measurement condition were at 0 V with 5 mW optical power. The measurement shows also that the photocurrent is symmetric at around 0 V, which means that photocarriers are collected in the same way on both electrodes. The negatives values are due to the fact that photocarriers travel in the opposite directions with respect to electric circuit direction of current. The laser beam spot was 35 µm (the diffusion length is estimated to be 0.19 µm). It should be noted that the not lightened area

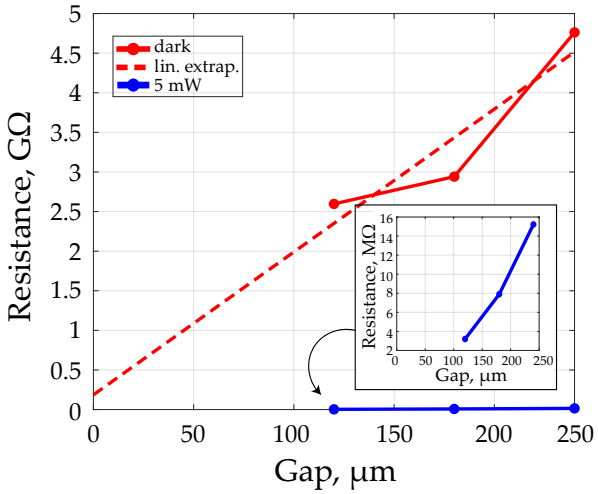

Figure 4.8 – *Resistance as function of gap distances. Inset: Zoom on the* 5 mW *curve.*

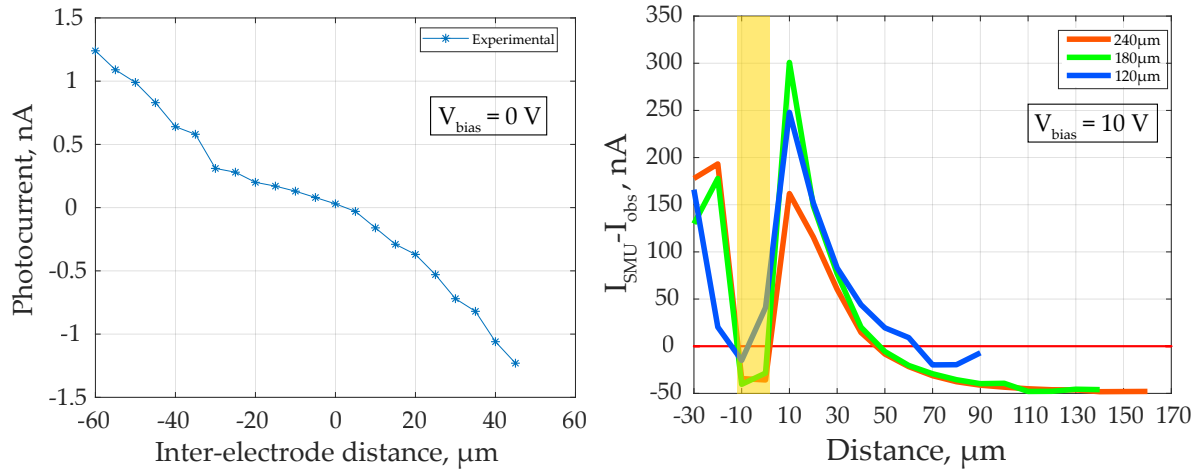

Figure 4.9 – *Optical characterization: Left) Photocurrent in function of the distance between the electrodes (at* 0 V *and* 5 mW*). Right) Photocurrent evolution along the electrodes axis (at* 10 V *and* 5 mW*) for* 240 µm, 180 µm *and* 120 µm *gaps.*

affect overall the datas. This is means that for large gap, the resistance of the lightened area is much higher that the lightened area.

In the Fig. 4.9, the evolution of photocurrent as beam is moved along the electrodes is plotted. So, the waist is much greater than the diffusion length. Fig. 4.9 (right) shows the evolution of the photocurrent along the electrodes axis for each different gap (240 µm, 180 µm and 120 µm) at 10 V. The gold section is the reference and where the photocurrent is near to zero this happens because the IR light is almost totally reflected. A high–peak value is then obtained near the anode. This is a well–known phenomenon seen in the literature [75] and it is due to the higher mobility of the electrons compared to the holes mobility which enables electrons to reach the anode in a shorter time than that for the holes. In agreement with this interpretation, lower photocurrent is illustrated on the cathode side (negative values).

4.1.4 THz antennas and annealing

A THz Antennas

Using the same process than for TLM, SESAM containing 3 bowtie antennas was fabricated by a previous Master student [184] before the beginning of this PhD. The only difference be-

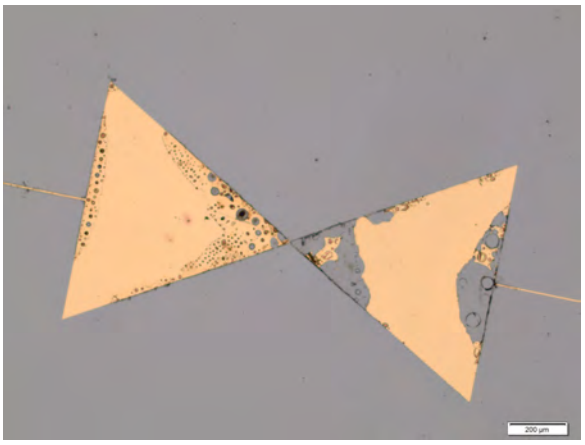

Figure 4.10 – *A (burned) bow–tie antenna.*

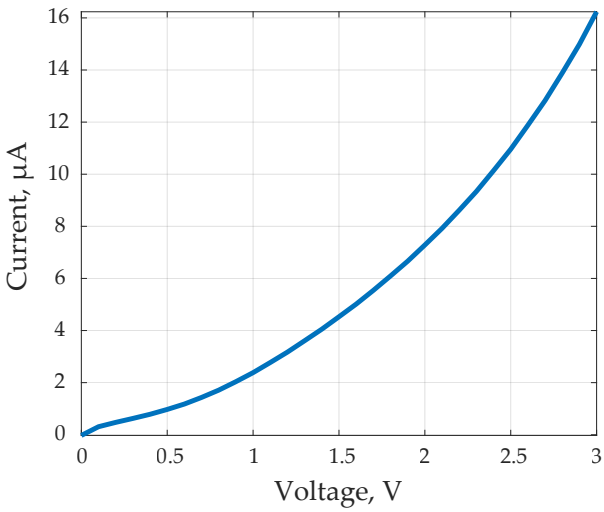

Figure 4.11 – *First I–V characterization of the SESAM device with bow–tie antenna (Schottky contact).*

tween them is the angle ($30°$, $60°$ and $90°$) and the antenna gain is slightly different (around 2 dBi). Typically, a $60°$ bow–tie antenna is that providing the highest realized gain. The gap was $5\ \mu\mathrm{m}$ and the active surface is then $25\ \mu\mathrm{m}^2$. Fig. 4.10 shows a picture of the bow–tie antenna, note that this figure was taken after strong optical excitation ($\sim\ 50\ \mathrm{mW}$), thus explaining the metal degradation.

B Rapid Thermal Annealing (RTA)

A photomixer needs to have ohmic contacts and the contact resistance must be as low as possible. This would push further the breakdown threshold of the device. The Au contact on the semiconductor was initially bad (Schottky behavior, see Fig. 4.11). The contact was improved by rapid thermal annealing (RTA) at about $400°\mathrm{C}$ for $30\ \mathrm{s}$. Annealing only one time is sufficient for SESAM devices to get an ohmic contact. However, the I–V characterization showed a very high current (mA–range) at very low bias voltage ($3\ \mathrm{mA}$ at $\sim\ 0.6\ \mathrm{V}$), corresponding to $200\ \Omega$. This resistance is not compatible with previous results. In fact, the expected resistance should be high ($M\Omega/G\Omega$ levels). Several RTA, measurements of the I–V (and so the resistance) as function of temperature and time were done. The interest is to find an annealing parameter that would allow to decrease the contact resistance as much as possible. The Fig. 4.12 shows the resistance as functions of annealing steps (different duration while the temperature is constant).

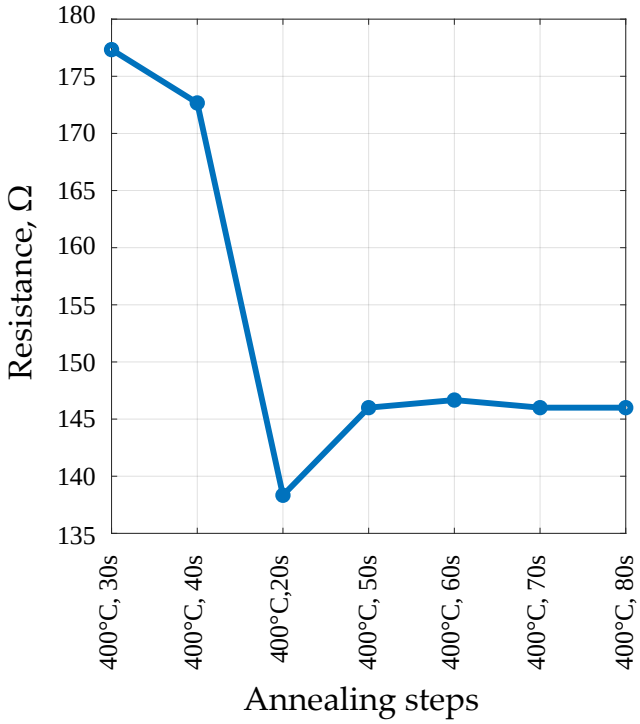

Figure 4.12 – *Contact resistance as function of annealing steps. At a constant temperature but different time of annealing, a low contact resistance can be obtained.*

Similar investigations of metal–semiconductor contacts can be found in Refs. [185, 186]. The results show that contact resistance could be reduced depending on the annealing time and temperature. The minimum resistance (including probes and metal–semiconductor contacts) obtained is $\sim 138\ \Omega$ at 400 °C for a 20 s annealing time (the SESAM resistance before annealing was much higher, in order of MΩ). The hypothesis of this such low resistance is perhaps due to the high–temperature annealing associated with a long exposure time. To conclude, SESAM devices should be annealed at lower temperature and/or at shorter exposure time. This would avoid the short–circuit of the device (i.e. very low resistance).

4.1.5 Discussion

For the moment, we have only been able to carry out preliminary experiments which are not yet fully understood. The understanding of the lamp light effect (Fig. 4.7) along with the non–linear response of the SESAM (Fig. 4.7) are still in progress. The best gap is, the smallest one ($120\ \mu$m) as it provides more photocurrent. Unfortunately, THz emission from SESAM is not yet demonstrated (only one sample was tested at this time). Perhaps, a proper thermal management of the SESAM by using a peltier module would increase the absorption (by tuning the absorption resonance wavelength) and thus increase the chance to detect a THz signal. However, the results obtained thanks to TLM process proved that SESAM devices could be used for THz generation in CW regime (resistance drops under 1064 nm light) and their performances relies on the SESAM capabilities (especially absorption rate and high resistance). So, it would be interesting to push forward the study and fabricate other SESAM–based devices, maybe by incorporating plasmonic contact electrodes to improve the optical–THz conversion efficiency.

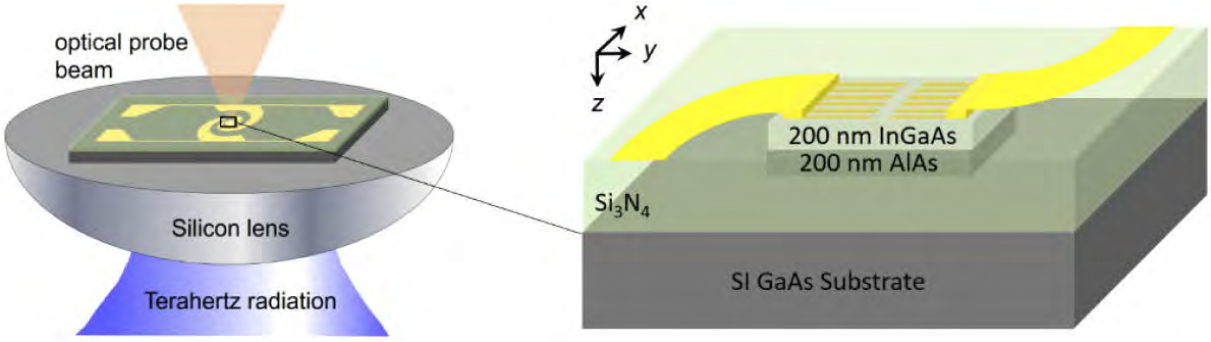

Figure 4.13 – *Schematic of the spiral-antenna-based plasmonic terahertz device operating at* $1060\ \mathrm{nm}$. *Figures taken from* [5].

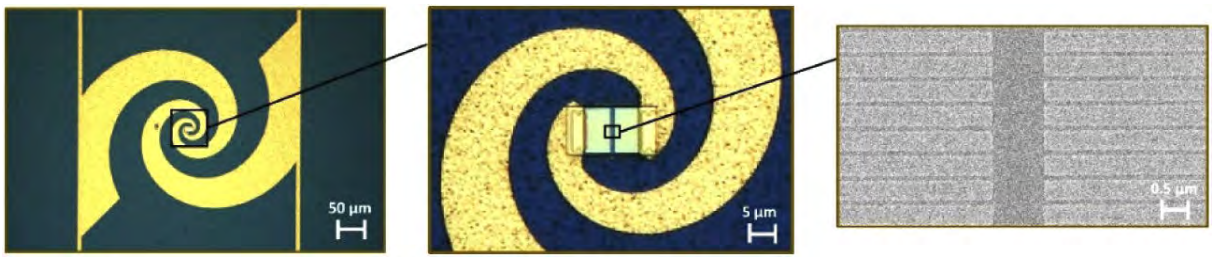

Figure 4.14 – *The optical microscopy image of a similar fabricated photomixer prototype and the scanning electron microscopy image of the plasmonic contact electrodes at the center of the photomixer. Figures taken from* [5].

4.2 Plasmonic–based photomixers

4.2.1 Fabrication

The photomixer consists of a photoconductor with plasmonic contact electrodes integrated with a broadband logarithmic spiral antenna [5]. The photomixer is fabricated at UCLA on an epitaxial semiconductor structure consisting of a 200–nm–thick undoped $In_{0.53}Ga_{0.47}As$ layer and a 200–nm–thick AlAs layer grown on an SI–GaAs substrate (Fig. 4.13). The plasmonic contact electrodes, which are in the form of one–dimensional metallic gratings separated by a small tip–to–tip gap, have a $10\ \mu\mathrm{m} \times 20\ \mu\mathrm{m}$ area each. They are designed to enhance optical intensity inside the $In_{0.53}Ga_{0.47}As$ layer near the tip of the gratings by excitation of surface plasmon waves. The $In_{0.53}Ga_{0.47}As$ layer is etched everywhere except under the plasmonic electrodes and the gap, to form a mesa structure, which prevents photocarrier generation outside the device active area and increase the resistance of the device [5]. Covered with a S_3N_4 anti–reflection coating (ARC), the plasmonic electrodes are optimized to offer the largest absorption of a transverse–magnetic (TM) incident optical beam at $1064\ \mathrm{nm}$ in the $In_{0.53}Ga_{0.47}As$ layer. In order to maximize THz power, a narrow ellipse beam that covers the entire gap ($1\ \mu\mathrm{m} \times 10\ \mu\mathrm{m}$) between the two plasmonic contact electrodes and tightly confined around the grating tips (Fig. 4.14) is used. The devices were fabricated by P.–K. Lu and Prof. M. Jarrahi. The fabrication process starts with electron–beam lithography patterning electron–beam evaporation of $3/77\ \mathrm{nm}$ Ti/Au, and lift–off to realize the plasmonic contact electrodes. Next, the $In_{0.53}Ga_{0.47}As$ layer is dry etched by using Cl_2/Ar chemistry with the plasmonic electrodes masked by a maN–2405 electron–beam resist. The $240\ \mathrm{nm}$–thick Si_3N_4 ARC is then deposited globally using plasma–etched chemical vapor deposition. Then, contact vias at the edge of both plasmonic electrodes are patterned by optical lithography and opened by CHR_3/O_2 reactive ion etching chemistry. Finally, the logarithmic spiral antenna and bonding pads are patterned by optical lithography followed by $50/500\ \mathrm{nm}$

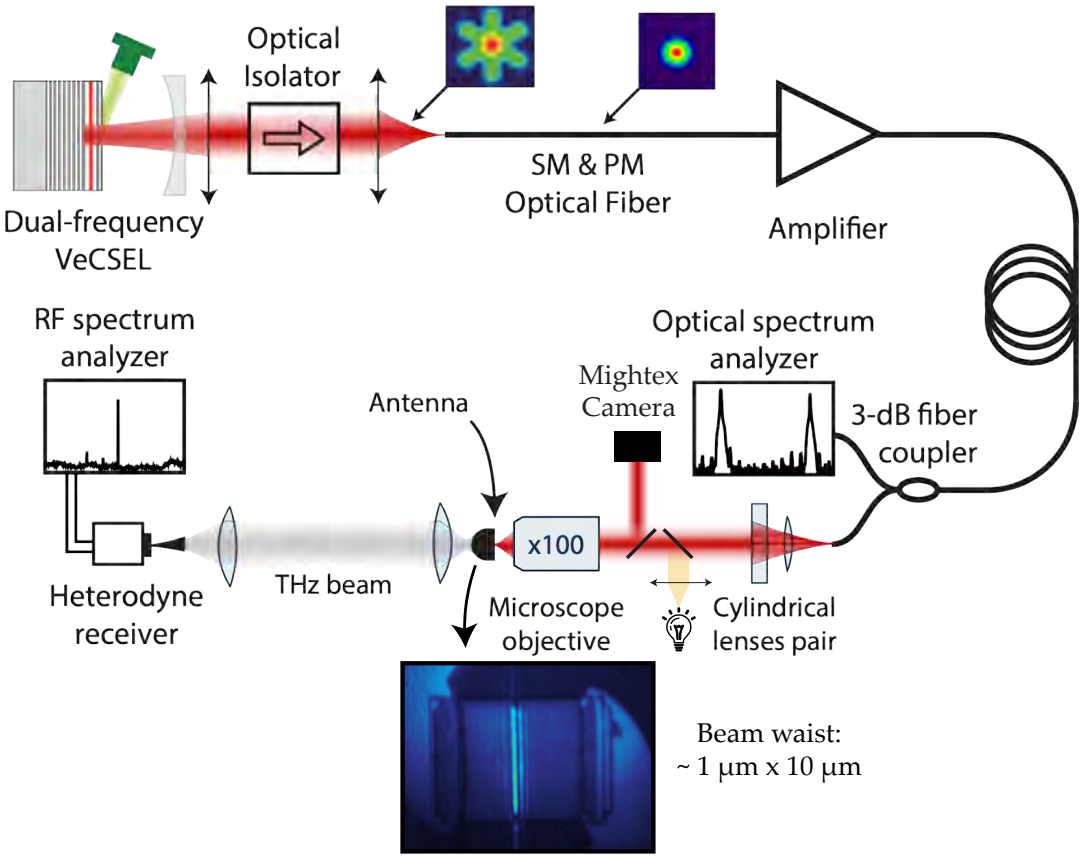

Figure 4.15 – *Experimental setup for THz emission using DF–VeCSEL and short–transit–time photocondutors.*

Ti/Au deposition and lift–off. The photomixer is glued on a hyper–hemispherical silicon lens of $12\ \mathrm{mm}$ diameter and central thickness $5.3\ \mathrm{mm}$ to extract THz waves and quasi–collimate the THz beam to the free space.

4.2.2 Optical and electrical characterization

A Experimental setup

The same DF–VeCSEL, operating at a centre wavelength of $1064\ \mathrm{nm}$ with an output power of $60\ \mathrm{mW}$ using two pump laser diodes (LD785–SE400 from Thorlabs) and operating in CW was used. LG_{00} & LG_{03} modes were used (mask 0.72/0.8), as seen in the Fig. 4.15. At the output of the DF–VeCSEL, the beam was collimated using a lens of focal length of $50\ \mathrm{mm}$ and focusing into a SM & PM optical fiber using a lens of focal length of $11\ \mathrm{mm}$. A $40\ \mathrm{dB}$ optical isolator (Isowave I–196-SD–5L) was also used between the two lenses to avoid parasitic reflection into the DF–VeCSEL. Then, a $2\ \mathrm{W}$ optical amplifier (from Keopsys) was used to achieve higher power optical beating. To monitor the dual–frequency laser and control the optical power, a fiber coupler to split 1% of the amplified optical light to the optical spectrum analyzer (OSA) from Anritsu [2] and a fiber attenuator were also used. The laser spot was then collimated and focused onto the photomixer. Two setups were used to focus onto the photomixer: one using pair of lenses and the other using a $\times 100$ microscope objective (Mitutoyo APO M IR). The dc bias of photomixer was supplied by a SMU, which was also used to monitor the dc current flowing in the device. The current was limited by a compliance of $1\ \mathrm{mA}$, to avoid the destruction of the device owing to

2. The OSA has a resolution of $0.02\ \mathrm{nm}$.

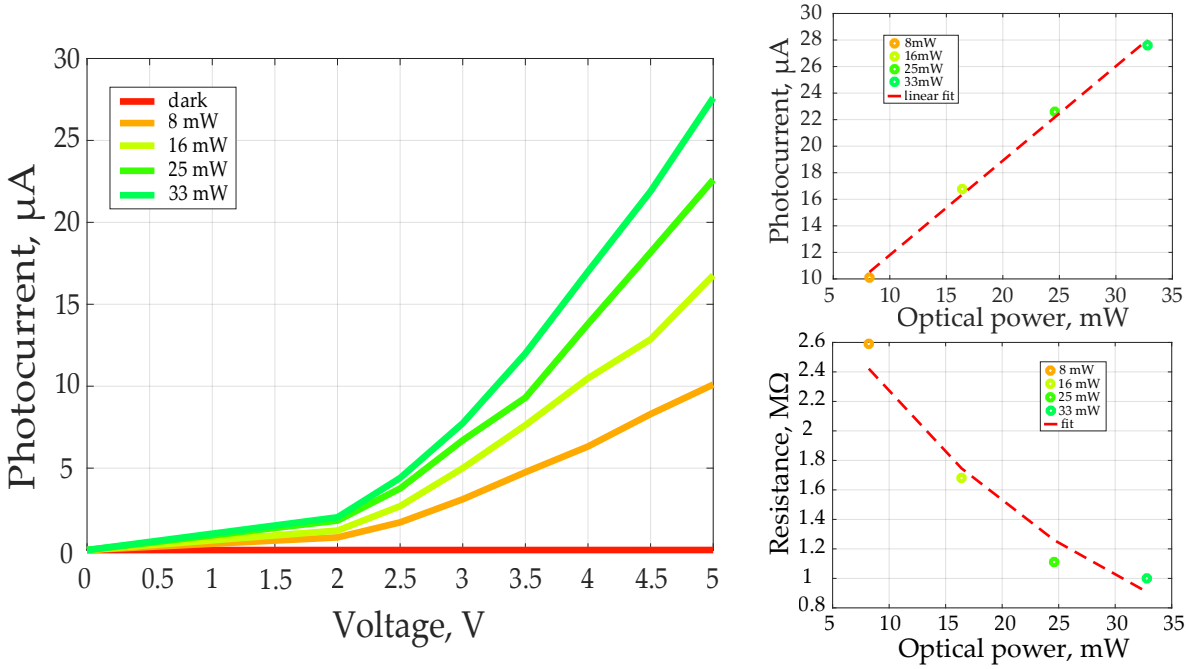

Figure 4.16 – *Optical characterization: Left) I–V characterization of plasmonic–based sample at* 8 mW, 16 mW, 25 mW *and* 33 mW. *Top right) Photocurrent as function of optical power. Bottom right) Resistance as function of optical power.*

heating effects. An imaging setup was implemented using a lens of focal length ranging from 50 mm to 150 mm with an expected magnification from ×20 to ×60, a fiber optic illuminator and a Mightex camera. The fiber optic illuminator is collimated using a lens of focal length of 60 mm. The THz measurement setup consists of a pair of teflon lenses (LAT100 from Thorlabs), a commercially available heterodyne head (RPG) and using a calibrated table loaded into the electrical spectrum analyzer (ESA) to detect the signal in the frequency–range of the ESA (BW of 43 GHz, from R&S) (Fig. 4.15) for incoming signals of 168.5–371.5 GHz.

B I–V characterization

Fig. 4.16 shows the I–V characteristic of the plasmonic device. The photocurrent increases with bias–voltage and with optical power as expected. It is difficult to say whether the current increases linearly (ohmic behavior) or exponentially (Schottky behavior) with bias voltage. But the device responses well to the dual–frequency laser. The dark photocurrent at 5 V is 3 nA, the same values as UCLA data. Depending on the optical setup, the photocurrent was higher or lower than the UCLA data. These UCLA data were obtained under optical excitation of 800 nm. There is a ×1000 factor between dark photocurrent and photocurrent. However, the present photocurrent values does not fit with UCLA data at the moment. This might be attributed to the shape and/or size of the laser beam spot. Other reasons are given in the section 4.2.3. Fig. 4.16 (top right) illustrates the linear evolution of the photocurrent as function of the optical power. And then in the same figure (bottom right), the evolution of the resistance as function of the same optical power is presented. The resistance is obtained by using Ohm law (only one point, at 5 V and under laser light). These results were obtained using achromatic lenses as optical elements to focus the light into the photomixer.

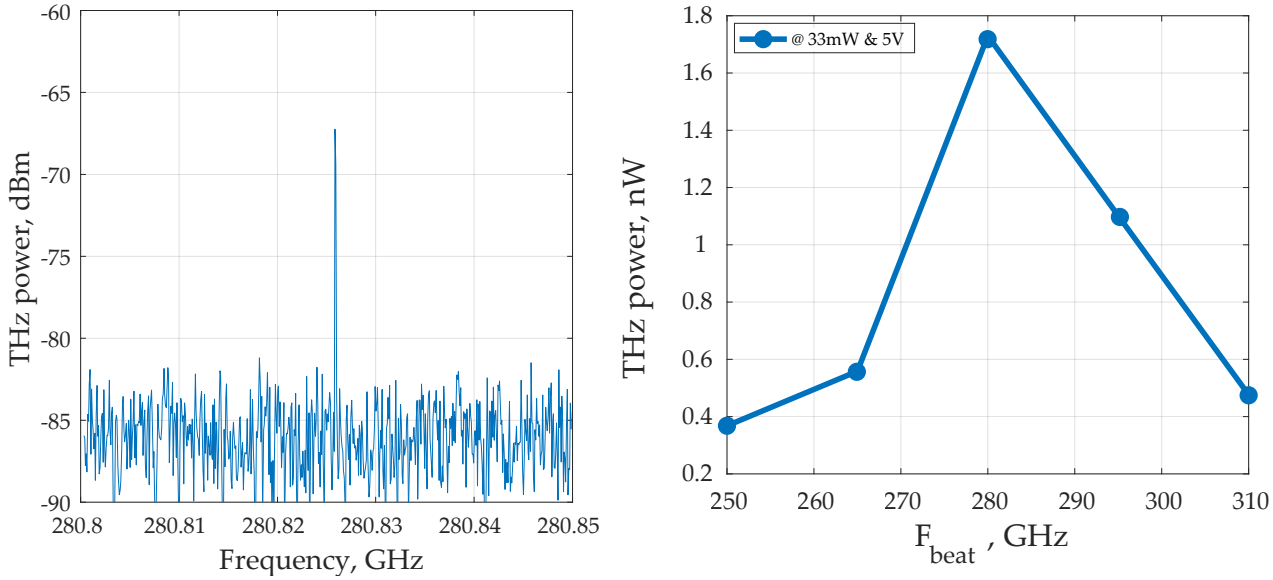

Figure 4.17 – *Optical characterization: Left) THz emission around* 280 GHz. *Right) THz tunability around* 280 GHz *at* 5 V *and* 33 mW *optical power. These results were obtained without using any objective lens but instead a pair of cylindrical lens (focal lengths of* 15 mm *&* 50 mm *respectively) at the output of* 99% *side of the optical coupler and an aspherical lens (focal length of* 20 mm*) for focusing into the photoconductor.*

4.2.3 Results and discussion

A THz emission of about 2 nW (without considering at least 5 dB loss due to teflon lens and unmatched polarization between horn and spiral antennas) using plasmonic-devices at around 280 GHz is shown in the left of Fig. 4.17. This was the first THz emission using this kind of antenna for a CW excitation at 1064 nm. In the right of Fig. 4.17, the tunability of the THz emission (with steps of 15 GHz) thanks to the DF-VeCSEL tunability as well as the resonance of the spiral antenna expected to be around 280 GHz is showed. In the Figures 4.18, THz power function of optical power and voltage are showed. An increase with both optical power (8 mW, 16 mW, 25 mW, 33 mW) and bias voltage (from 2 V to 5 V) is observed. The THz power evolution is quasi–linear as function of optical power and quadratically as function of bias voltage. In fact, THz power is proportional to the photocurrent squared (quadratic) and the photocurrent is proportional to the bias voltage (if the contact is ohmic). The power was expected to be at 1 µW (testing were done by UCLA collaborators using 800 nm lasers and bolometer as detector) so 30 dB higher than present results. The low power could be caused by several factors:

— **THz coupling to waveguide.** A loss could come from the THz coupling to the heterodyne head/waveguide. A 6 dB loss is estimated by simulating Si–lens along with the horn antenna and waveguide dimensions using CST, this simulation was done by A. Penarier at IES.

— **Air-gap between antenna and Si–lens.** A bad gluing between the die and the Si–lens might create air gap, that would significantly decrease the THz output power due to the cavity filtering and impedance mismatch.

— **Inadequate optical beam shape.** The fact that the size spot required is at diffraction limit (1 µm), it was difficult to measure the real spot size since the Mightex resolution is 5 µm and the Phasics SID4 wavefront sensors requires a spot of 3 mm in order to better analyze the wavefront, i.e. to estimate the spot size at the focus by measuring the wavefront phase. Many attempts have been done by using several optical elements configuration

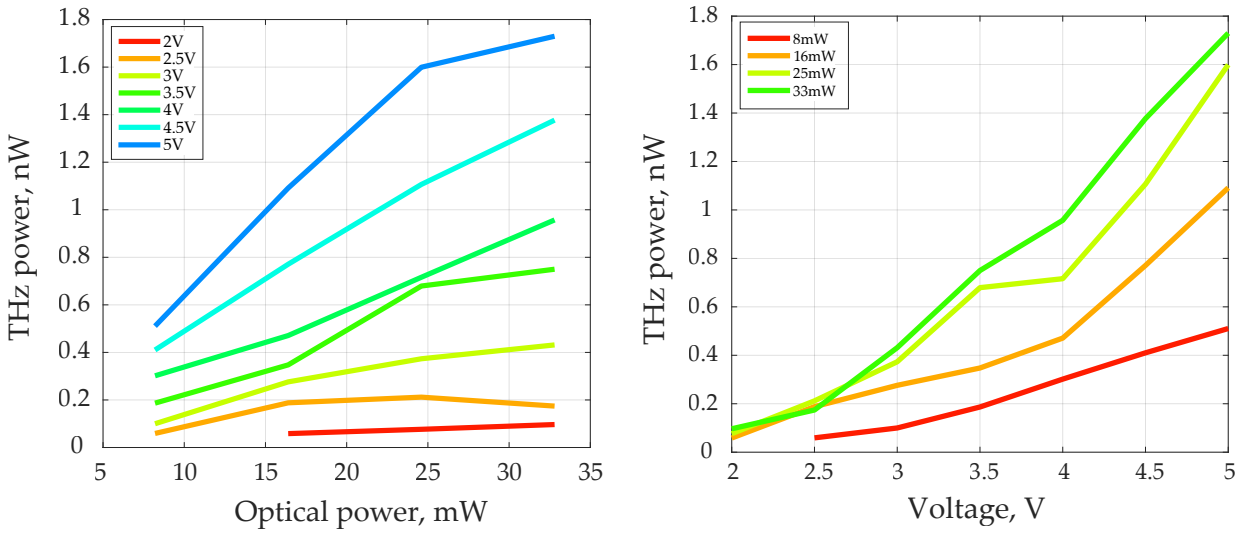

Figure 4.18 – *Optical characterization: Left) THz power function of optical power. Right) THz power function of bias voltage at around* 280 GHz. *These results were obtained without using any objective lens but instead a pair of cylindrical lens (focal lengths of* 15 mm *&* 50 mm *respectively) at the output of* 99% *side of the optical coupler and an aspherical lens (focal length of* 20 mm*) for focusing into the photoconductor.*

and nanopositioning stages in order to achieve an optimal beam shape without really impacting the THz output power.

— **Low signal–to–noise (SNR) ratio at amplifier output.** An experimental comparison has been made between two similar setups (with and without optical amplifier). Using the same condition ($\sim$ 80 µW optical power at 5 V), the photocurrent was similar ($\sim$ 1 µA) but there were THz emission without amplifier, -91 dBm and no THz emission at all with amplifier. A power of 0.45 mW was thus necessary to get the same THz power. So, $\times 5$ power is required (with the amplifier) to get the same THz power, which potentially means a > 6 dB in loss. By measuring the power at the output of the optical amplifier, an amplified stimulated emission power is estimated to be 78% of the desired signal (optical beating) and the SNR is about 6.5 dB. This amplified optical power will only burn the device. In this case, the optical beating efficiency must be improved and/or an optical amplifier with lower available gain should be used. So, the SNR should raise and thus the THz emitted power.

A total loss of about $\sim$ 16 dB is estimated. The photocurrent was x100 (at 30 mW and 5 V) lower compared to UCLA datas and there was a difference of 22 dB in terms of THz power. However, considering all the losses (at least 16 dB), similar THz power is obtained (difference of 6 dB total loss) with even $\times 10$ lower photocurrent. Despite the very low power, these results are at the state of the art compared to previous works where a bolometer was used to evaluate the emitted power [97]. Further improvements are expected by building–up a better optical setup and/or using lower gain optical amplifier.

4.3 Summary

In this chapter, two photomixers were studied: SESAM–based photomixer and InGaAs–based photomixers with plasmonic contact electrodes. Even if the THz emission is not yet reported using SESAM as photomixer, TLM results show encouraging results. These results in-

dicate a fall of resistance by a factor of at least $\times 70$, which means that there should be sufficient photocurrent available to generate THz waves. Although the expected performance is not yet fully achieved $(\text{at least } 1\ \mu\mathrm{W} \text{ at } 280\ \mathrm{GHz} \text{ is expected})$ for the InGaAs–based photomixers, the results obtained here are at the state–of–the–art as well as a first demonstration of THz emission by using a combination of VeCSEL and plasmonic–based photomixers. This is the first CW THz emission without using an external optical modulator and/or chopper using $1064\ \mathrm{nm}$ optical sources. Nevertheless, further improvements on the optical setup are required to improve the emitted THz output power.

Conclusions

The objective of this thesis was the study of original antennas in order to fit with the spatial distribution of the LG transverses modes at the output of the DF–VeCSEL and thus increase the THz power.

In the first chapter, THz sources were reviewed in terms of power, coherence, tunability and so forth, all operating at room temperature. Almost no present THz source meet the requirements to develop ultra high data rate telecommunications. To meet all of these requirements, photomixing presents a very promising solution. However, depending on the type of photomixer, they generally suffer in terms of low conversion efficiency leading to insufficient emitted THz power. PCA and UTC devices present the potential to increase the THz power and thus to significantly help the development of THz systems.

In the second chapter, dual–frequency VeCSELs are proved to be an excellent candidate for the THz emission as all the mentioned requirements are met except for the THz power. Powerful, highly–coherent, stable and highly–tunable emission was achieved by DF–VeCSELs technologies based on Laguerre–Gauss tranverses modes. This powerful photonic source combined with a powerful photomixer, makes it a very competitive THz source.

In order to increase the THzpower using these DF–VeCSEL ny collecting all the optical beating spot, multipolar antennas design were proposed and investigated in the third chapter. The simplest of antennas design (dipole) was used. Using FIT–based simulation (CST Studio Suite), numerical results for different geometric parameters of the multipolar antennas evidenced the important role of electromagnetic coupling which strongly impact the antenna efficiency and so the overall photomixer efficiency. A trade–off exist between the strong (low) coupling and the low (strong) optical–THz conversion efficiency. In fact, the gap length is limited to few μm (carrier transit time) with a consequence that the antenna is less efficient due to strong coupling (arms too close between them).

In the fourth chapter, two different photomixers designed at around 1064 nm were characterized: SESAM-based photomixers and plasmonic–based photomixers. TLM were fabricated and characterized in order to evaluate the resistance of the SESAM. A SESAM ready photomixer integrating a bow–tie antenna design at 100 GHz was tested. Despite the fact that THz is not achieved yet, the results can be considered as quite encouraging because a significant resistance drop was observed as SESAM was photo–excited. To increase the possibility of THz emission, incorporating plasmonic contact electrodes could be a solution. Another solution could be to

add a few steps on fabrication by etching away all the active layer except the gap area.

Using InGaAs–based plasmonic photomixers, THz emission was successfully demonstrated using $1064\ \mathrm{nm}$ excitation for the first time. This was a first emission in C.W. using $1064\ \mathrm{nm}$ designed devices. Also, this is the first time a DF–VeCSEL is combined with efficient plasmonic–based photomixers. Although the expected THz power is not fully achieved yet, these work are at the state–of–the–art.

After the successfully demonstration of C.W. THz generation using plasmonic–based devices driven by the DF–VeCSEL in extra–cavity operation mode, the ultimate goal would be the integration of these photomixers and the DF–VeCSEL in a single–cavity forming a powerful, coherent and tunable THz emitter. This is a long–term research project due to the numerous challenges (dynamics, non–linear effects, diffraction loss, etc...) and the technological limits to overcome.

Appendix A

Antenna design parameters

In this Appendix, the design parameters of the multipolar antennas seen in the Chap. 3 are reported. For each multipolar antenna MP_{02}, MP_{03} and MP_{04}, they are simulated at resonances R1, R2 and R3 for each excitation mode MM_1 and MM_4.

A.1 Multipolar antenna, MP_2

A.1.1 Design at first resonance (R1)

MM_1	
Arm length (μm)	735
Gap (μm)	80
Arm width (μm)	40

MM_4	
Arm length (μm)	900
Gap (μm)	80
Arm width (μm)	40

A.1.2 Design at second resonance (R2)

MM_1	
Arm length (μm)	2220
Gap (μm)	80
Arm width (μm)	40

MM_4	
Arm length (μm)	2310
Gap (μm)	80
Arm width (μm)	40

A.1.3 Design at third resonance (R3)

MM_1	
Arm length (μm)	3710
Gap (μm)	80
Arm width (μm)	40

MM_4	
Arm length (μm)	3800
Gap (μm)	80
Arm width (μm)	40

A.2 Multipolar antenna, MP_3

A.2.1 Design at first resonance (R1)

MM_1	
Arm length (μm)	780
Gap (μm)	80
Arm width (μm)	40

MM_4	
Arm length (μm)	780
Gap (μm)	80
Arm width (μm)	40

A.2.2 Design at second resonance (R2)

MM_1	
Arm length (μm)	2260
Gap (μm)	80
Arm width (μm)	40

MM_4	
Arm length (μm)	2400
Gap (μm)	80
Arm width (μm)	40

A.2.3 Design at third resonance (R3)

MM_1	
Arm length (μm)	3750
Gap (μm)	80
Arm width (μm)	40

MM_4	
Arm length (μm)	3900
Gap (μm)	80
Arm width (μm)	40

A.3 Multipolar antenna, MP_4

A.3.1 Design at first resonance (R1)

MM_1	
Arm length (μm)	780
Gap (μm)	80
Arm width (μm)	20

MM_4	
Arm length (μm)	780
Gap (μm)	80
Arm width (μm)	20

A.3.2 Design at second resonance (R2)

MM_1	
Arm length (μm)	2310
Gap (μm)	80
Arm width (μm)	20

MM_4	
Arm length (μm)	2310
Gap (μm)	80
Arm width (μm)	20

A.3.3 Design at third resonance (R3)

MM_1	
Arm length (μm)	3750
Gap (μm)	80
Arm width (μm)	20

MM_4	
Arm length (μm)	3800
Gap (μm)	80
Arm width (μm)	20

Appendix B

Publications

Peer–Reviewed Journal Papers

1. F. Z. Mahi, A. Abbes, C. Palermo and L. Varani **"Systematic analysis of semiconductor photoconductivity dynamics under different laser excitations: two– and three–level models,"** (*In preparation*).
2. A. Abbes, R. Emadi, A. Pénarier, P. Nouvel, E. Moreno, S. Blin and L. Varani **"Coherent THz Wave Generation and Detection Using Multipolar Antennas Coupled to InGaAs/SI–GaAs Photomixers,"** (*In preparation*).

Invited talk (presented by A. Abbes)

1. **"Upscaling the output power of a photo–mixing THz source driven by a dual–frequency laser operating on two transverse modes,"** Terahertz Emitters, Receivers and Application X, SPIE Optics+Photonics, San Diego, CA, USA, August 11–15, 2019. doi: https://doi.org/10.1117/12.2530266 (*Invited Talk*)

International Conference Papers and Abstracts (with proceedings)

1. A. Abbes, P–K. Lu, P. Nouvel, A. Pénarier, L. Varani, A. Garnache, M. Jarrahi and S. Blin **"280 GHz Radiation Source Driven by a 1064 nm Continuous–Wave Dual–Frequency Vertical External Cavity Semicondutor Laser,"** IRMMW 2021, Chengdu, China, August 29–September 3, 2021 (Virtual). doi: 10.1109/IRMMW-THz50926.2021.9566938
2. M. Myara, B. Chomet, A. Abbes, A. Garnache, S. Blin, G. Beaudoin and I. Sagnes **"Upscaling the output power of a photo–mixing THz source driven by a dual–frequency laser operating on two transverse modes,"** Proc. SPIE 10926, Quantum Sensing and Nano Electronics and Photonics XVI, 10926E (1 February 2019). doi: 10.1117/12.2514721 (*Invited Talk*)
3. A. Abbes, R. Paquet, B. Chomet, A. Garnache, M. Myara, P. Nouvel, A. Pénarier, G. Beaudoin, I. Sagnes, D. Coquillat, W. Knap and S. Blin **"Towards wireless THz communications: Photonic–driven source and transistor–based detector,"** 2018 25th International Conference on Telecommunication (ICT), Saint Malo, France, June 26–28, 2018. doi: 10.1109/ICT.2018.8464900 (*Invited Talk*)

International Conference Paper and Abstract

1. A. Abbes, B. Chomet, M. Myara, A. Garnache, G. Beaudoin, I. Sagnes and S. Blin **"Towards transverse multiplexing of THz photo–driven emitters driven by a dual–transverse–mode dual–frequency laser,"** French–German Terahertz Conference 2019 (FGTC 2019), Kaiserlautern, Germany, April 2–5, 2019.

National Conference Paper and Abstract (with proceeding)

1. A. Abbes, S. Blin, B. Chomet, R. Paquet, M. Myara, L. Le Gratiet, G. Beaudoin, I. Sagnes and A. Garnache, **"Upscaling photo–mixing THz power driven by a dual–transverse–modes laser,"** in Proc. Journées Nationales du Réseau Doctoral en Micro–nanoélectronique, JNRDM'2019, Montpellier, France, June 3–5, 2019. Proc.: http://www.cnfm.fr/JNRDM

National Conference Paper and Abstract

1. A. Abbes, P–K. Lu, P. Nouvel, A. Pénarier, L. Varani, A. Garnache, M. Jarrahi and S. Blin **"280 GHz Radiation Source Driven by a 1064 nm Continuous–Wave Dual–Frequency Vertical External Cavity Semicondutor Laser,"**, GDR NanoTeraMIR, June 9–10, 2021 (Virtual).

Poster (with proceeding)

1. A. Abbes, S. Blin, B. Chomet, R. Paquet, M. Myara, L. Le Gratiet, G. Beaudoin, I. Sagnes and A. Garnache, **"THz Emission Driven by a Dual–Transverse–Modes Laser,"** 2018 2nd URSI Atlantic Radio Science Meeting (URSI AT–RASC), Gran Canaria, Spain, May 28–June 1, 2018. doi: 10.23919/URSI-AT-RASC.2018.8471486

Poster

1. S. Blin, A. Abbes, B. Chomet, M. Myara, G. Beaudoin, I. Sagnes, L. Varani and A. Garnache, **"Towards THz power enhancement using spatial multiplexing photo–mixers driven by a dual–frequency VeCSEL,"** The 21st International Conference on Electron Dynamics in Semiconductors, Optoelectronics and Nanostructures, Nara, Japan, July 14–19, 2019.

Other Peer-Reviewed Journal Paper

1. J. Le Gouët, J. Oudin, P. Perrault, A. Abbes, A. Odier and A. Dubois, **"On the Effect of Low Temperatures on the Maximum Output Power of a Coherent Erbium–Doped Fiber Amplifier,"** *Journal of Lightwave Technology*, vol. 37, no. 14, pp. 3611–3619, 15 July, 2019. doi: 10.1109/JLT.2019.2918357

Other Publications

1. A. Bassli, A. Abbes, P. Nouvel, A. Penarier, M. Myara, J. Belkadid and S. Blin **"3D Imaging of Materials at 0.1 THz for Inner–Defect Detection,"** French–German Terahertz Conference

2019 (FGTC 2019), Kaiserlautern, Germany, April 2–5, 2019.

Popularization

1. N. Vigne, B. Chomet, A. Abbes, M. Seghilani, S. Blin, M. Myara, G. Beaudoin, L. Legratiet, K. Pantzas, I. Sagnes, P. Lalanne, S. Denet and A. Garnache **"États originaux de la lumière par structuration 3D de l'émission d'un laser à métasurface,"** *Photoniques*, no. 109, pp. 46–50, 2021.

Bibliography

[1] B. Chomet, "Integration of high coherence tunable semiconductor laser. non-linear multimode dynamics and route to single frequency operation." PhD Thesis, University of Montpellier (2019).

[2] A. Laurain, "Sources laser à semiconducteur à émission verticale de haute cohérence et de forte puissance dans le proche et le moyen infrarouge." PhD Thesis, University of Montpellier (2010).

[3] R. Paquet, "Nouvelles sources lasers pour génération THz." PhD Thesis, University of Montpellier (2016).

[4] E. Cabezon, "Photo-generated Metasurfaces at Terahertz Frequencies," PhD Thesis, University of Clermont Auvergne (2019).

[5] P.-K. Lu, D. Turan, and M. Jarrahi, "High–sensitivity telecommunication–compatible photoconductive terahertz detection through carrier transit time reduction," Opt. Express **28**, 26324–26335 (2020).

[6] M. Asada and S. Suzuki, "Terahertz Emitter Using Resonant-Tunneling Diode and Applications," Sensors **21**, 1384 (2021).

[7] M. Tonouchi, "Cutting-edge terahertz technology," Nat. Photon. **1**, 97–105 (2007).

[8] S. Dhillon, M. S. Vitiello, E. H. Linfield *et al.*, "The 2017 terahertz science and technology roadmap," J. Phys. D: Appl. Phys. **50**, 043001 (2017).

[9] P. Jepsen, D. Cooke, and M. Koch, "THz spectroscopy and imaging - Modern techniques and applications," Laser & Photon. Rev. **5**, 124–166 (2011).

[10] P. Siegel, "Terahertz Technology in Biology and Medicine," IEEE Trans. Microw. Theory Techn. **52**, 2438–2447 (2004).

[11] G. G. Hernandez-Cardoso, S. C. Rojas-Landeros, M. Alfaro-Gomez *et al.*, "Terahertz imaging for early screening of diabetic foot syndrome: A proof of concept," Sci. Rep. **7**, 42124 (2017).

[12] S. Yamaguchi, Y. Fukushi, O. Kubota *et al.*, "Brain tumor imaging of rat fresh tissue using terahertz spectroscopy," Sci. Rep. **6**, 30124 (2016).

[13] S. Fan, B. S. Y. Ung, E. P. J. Parrott *et al.*, "*In vivo* terahertz reflection imaging of human scars during and after the healing process," J. Biophoton. **10**, 1143–1151 (2017).

[14] S. H. Baek, J. H. Kang, Y. H. Hwang *et al.*, "Detection of Methomyl, a Carbamate Insecticide, in Food Matrices Using Terahertz Time-Domain Spectroscopy," J. Infrared Milli Terahertz Waves **37**, 486–497 (2016).

[15] P. H. Siegel, "THz Instruments for Space," IEEE Trans. Antennas Propag. **55**, 2957–2965 (2007).

[16] T. Nakagawa, "Observations of the Universe in the Terahertz Range: From AKARI to SPICA," IEEE Trans. Terahertz Sci. Technol. **5**, 7 (2015).

[17] G. Chattopadhyay, "Terahertz Instruments for CubeSats," in "2017 IEEE MTT-S International Microwave and RF Conference (IMaRC)," (2017 IEEE MTT-S International Microwave and RF Conference (IMaRC), Ahmedabad, 2017), pp. 1–5.

[18] N. Wang, S. Cakmakyapan, Y.-J. Lin *et al.*, "Room-temperature heterodyne terahertz detection with quantum-level sensitivity," Nat. Astron. **3**, 977–982 (2019).

[19] G. C. Bower, J. Dexter, K. Asada *et al.*, "ALMA Observations of the Terahertz Spectrum of Sagittarius A*," Astrophys. J. Lett. **881**, L2 (2019).

[20] S. Koenig, D. Lopez-Diaz, J. Antes *et al.*, "Wireless sub-THz communication system with high data rate," Nat. Photon. **7**, 977–981 (2013).

[21] G. Ducournau, P. Szriftgiser, F. Pavanello *et al.*, "THz Communications using Photonics and Electronic Devices: the Race to Data-Rate," J. Infrared Millim. Terahertz Waves **36**, 198–220 (2015).

[22] T. Nagatsuma, G. Ducournau, and C. C. Renaud, "Advances in terahertz communications accelerated by photonics," Nat. Photon. **10**, 371–379 (2016).

[23] S. Jia, X. Yu, H. Hu *et al.*, "120 Gb/s Multi-Channel THz Wireless Transmission and THz Receiver Performance Analysis," IEEE Photon. Technol. Lett. **29**, 310–313 (2017).

[24] J. Ma, N. J. Karl, S. Bretin *et al.*, "Frequency-division multiplexer and demultiplexer for terahertz wireless links," Nat. Commun. **8**, 729 (2017).

[25] S. Jia, G. Jacobsen, M. Galili *et al.*, "0.4 THz Photonic-Wireless Link With 106 Gb/s Single Channel Bitrate," J. Lightwave Technol. **36**, 610–616 (2018).

[26] T. Kürner, D. Mittleman, and T. Nagatsuma, "THz communications," Book, Springer (2021).

[27] C. Jansen, S. Wietzke, O. Peters *et al.*, "Terahertz imaging: applications and perspectives," Appl. Opt. **49**, E48 (2010).

[28] J. Grzyb, B. Heinemann, and U. R. Pfeiffer, "Solid-State Terahertz Superresolution Imaging Device in 130-nm SiGe BiCMOS Technology," IEEE Trans. Microwave Theory Techn. **65**, 4357–4372 (2017).

[29] D. M. Mittleman, "Twenty years of terahertz imaging," Opt. Express **26**, 9417 (2018).

[30] P. Hillger, J. Grzyb, R. Jain, and U. R. Pfeiffer, "Terahertz Imaging and Sensing Applications With Silicon-Based Technologies," IEEE Trans. THz Sci. Technol. **9**, 1–19 (2019).

[31] S. Fan, T. Li, J. Zhou *et al.*, "Terahertz non-destructive imaging of cracks and cracking in structures of cement-based materials," AIP Adv. **7**, 115202 (2017).

[32] M. C. Kemp, P. F. Taday, B. E. Cole *et al.*, "Security applications of terahertz technology," Proc. SPIE **5070**, 44 (2003).

[33] Y. Salamin, I.-C. Benea-Chelmus, Y. Fedoryshyn *et al.*, "Compact and ultra-efficient broadband plasmonic terahertz field detector," Nat. Commun **10**, 5550 (2019).

[34] R. T. Ako, A. Upadhyay, W. Withayachumnankul *et al.*, "Dielectrics for Terahertz Metasurfaces: Material Selection and Fabrication Techniques," Adv. Optical Mater. **8**, 1900750 (2020).

[35] B. Li, K. Hu, and Y. Shen, "A Scientometric Analysis of Global Terahertz Research by Web of Science Data," IEEE Access **8**, 56092–56112 (2020).

[36] F. Zhang, H.-W. Wang, K. Tominaga, and M. Hayashi, "Mixing of intermolecular and intramolecular vibrations in optical phonon modes: terahertz spectroscopy and solid-state density functional theory," Wiley Interdiscip. Rev. Comput. Mol. Sci. **6**, 386–409 (2016).

[37] G. Winnewisser, "Interstellar and laboratory spectroscopy in the terahertz region," J. Mol. Struct. **408-409**, 1–10 (1997).

[38] A. Menikh, S. P. Mickan, H. Liu, R. MacColl, and X.-C. Zhang, "Label-free amplified bioaffinity detection using terahertz wave technology," Biosens. Bioelectron. **20**, 658–662 (2004).

[39] Y. C. Shen, T. Lo, P. F. Taday *et al.*, "Detection and identification of explosives using terahertz pulsed spectroscopic imaging," Appl. Phys. Lett. **86**, 241116 (2005).

[40] M. Naftaly and R. E. Miles, "Terahertz Time-Domain Spectroscopy for Material Characterization," Proc. IEEE **95**, 1658–1665 (2007).

[41] R. M. Woodward, B. E. Cole, V. P. Wallace *et al.*, "Terahertz pulse imaging in reflection geometry of human skin cancer and skin tissue," Phys. Med. Biol. **47**, 3853–3863 (2002).

[42] C. D. Stoik, M. J. Bohn, and J. L. Blackshire, "Nondestructive evaluation of aircraft composites using transmissive terahertz time domain spectroscopy," Opt. Express **16**, 17039 (2008).

[43] W. R. Tribe, D. A. Newnham, P. F. Taday, and M. C. Kemp, "Hidden object detection: security applications of terahertz technology," Proc. IEEE, Terahertz and Gigahertz Electronics and Photonics III (2004).

[44] T. Buecher, S. Malz, K. Aufinger, and U. R. Pfeiffer, "A 210–291-GHz (8×) Frequency Multiplier Chain With Low Power Consumption in 0.13-um SiGe," IEEE Microw. Wireless Compon. Lett. **30**, 512–515 (2020).

[45] U. R. Pfeiffer, C. Mishra, R. M. Rassel *et al.*, "Schottky Barrier Diode Circuits in Silicon for Future Millimeter-Wave and Terahertz Applications," IEEE Trans. Microwave Theory Techn. **56**, 364–371 (2008).

[46] D. Pavlidis, "Fundamentals of Terahertz Devices and Applications," Book, Wiley (2021).

[47] A. Tessmann, A. Leuther, S. Wagner *et al.*, "A 300 GHz low-noise amplifier S-MMIC for use in next-generation imaging and communication applications," 2017 IEEE MTT-S International Microwave Symposium (IMS) pp. 760–763 (2017).

[48] L. John, A. Tessmann, A. Leuther *et al.*, "Broadband 300-GHz Power Amplifier MMICs in InGaAs mHEMT Technology," IEEE Trans. THz Sci. Technol. **10**, 309–320 (2020).

[49] K. Sengupta, T. Nagatsuma, and D. M. Mittleman, "Terahertz integrated electronic and hybrid electronic–photonic systems," Nat. Electron. **1**, 622–635 (2018).

[50] S. H. Naghavi, M. T. Taba, R. Han *et al.*, "Filling the Gap With Sand: When CMOS Reaches THz," IEEE Solid-State Circuits Mag. **11**, 33–42 (2019).

[51] X. Yi, C. Wang, Z. Hu *et al.*, "Emerging Terahertz Integrated Systems in Silicon," IEEE Trans. Circuits Syst. I **68**, 3537–3550 (2021).

[52] S. Kumar, "Recent Progress in Terahertz Quantum Cascade Lasers," IEEE J. Sel. Top. Quantum Electron. **17**, 38–47 (2011).

[53] B. S. Williams, "Terahertz quantum-cascade lasers," Nat. Photon. **1**, 517–525 (2007).

[54] M. S. Vitiello, G. Scalari, B. Williams, and P. De Natale, "Quantum cascade lasers: 20 years of challenges," Opt. Express **23**, 5167 (2015).

[55] M. S. Vitiello and A. Tredicucci, "Physics and technology of Terahertz quantum cascade lasers," Advances in Physics: X **6**, 1893809 (2021).

[56] J. Faist, F. Capasso, D. L. Sivco, C. Sirtori, A. L. Hutchinson, and A. Y. Cho, "Quantum cascade laser," Science **264**, 553–556 (1994).

[57] R. Köhler, A. Tredicucci, F. Beltram *et al.*, "Terahertz semiconductor-heterostructure laser," Nature **417**, 156–159 (2002).

[58] B. S. Williams, S. Kumar, Q. Hu, and J. L. Reno, "Operation of terahertz quantum-cascade lasers at 164 K in pulsed mode and at 117 K in continuous-wave mode," Opt. Express **13**, 3331 (2005).

[59] S. Fathololoumi, E. Dupont, C. Chan *et al.*, "Terahertz quantum cascade lasers operating up to 200 K with optimized oscillator strength and improved injection tunneling," Opt. Express **20**, 3866 (2012).

[60] L. Bosco, M. Franckié, G. Scalari *et al.*, "Thermoelectrically cooled THz quantum cascade laser operating up to 210 K," Appl. Phys. Lett. **115**, 010601 (2019).

[61] A. Khalatpour, A. K. Paulsen, C. Deimert *et al.*, "High-power portable terahertz laser systems," Nat. Photon. **15**, 16–20 (2021).

[62] X. Wang, C. Shen, T. Jiang *et al.*, "High-power terahertz quantum cascade lasers with 0.23 W in continuous wave mode," AIP Adv. **6**, 075210 (2016).

[63] L. Li, L. Chen, J. Freeman *et al.*, "Multi-Watt high-power THz frequency quantum cascade lasers," Electron. lett. **53**, 799–800 (2017).

[64] C. A. Curwen, J. L. Reno, and B. S. Williams, "Terahertz quantum cascade VECSEL with watt-level output power," Appl. Phys. Lett. **113**, 011104 (2018).

[65] B. Williams, S. Kumar, Q. Hu, and J. Reno, "High-power terahertz quantum-cascade lasers," Electron. Lett. **42**, 89–91 (2006).

[66] C. A. Curwen, J. L. Reno, and B. S. Williams, "Broadband continuous single-mode tuning of a short-cavity quantum-cascade VECSEL," Nat. Photon. **13**, 855–859 (2019).

[67] H. Nguyen-Van, A. N. Baranov, Z. Loghmari *et al.*, "Quantum cascade lasers grown on silicon," Sci. Rep. **8**, 7206 (2018).

[68] D. Burghoff, T.-Y. Kao, N. Han *et al.*, "Terahertz laser frequency combs," Nat. Photon. **8**, 462–467 (2014).

[69] M. S. Vitiello, L. Consolino, M. Inguscio, and P. De Natale, "Toward new frontiers for terahertz quantum cascade laser frequency combs," Nanophotonics **10**, 187–194 (2020).

[70] Q. Lu, F. Wang, D. Wu *et al.*, "Room temperature terahertz semiconductor frequency comb," Nat. Commun. **10**, 2403 (2019).

[71] M. Piccardo, M. Tamagnone, B. Schwarz *et al.*, "Radio frequency transmitter based on a laser frequency comb," Proc. Natl. Acad. Sci. U.S.A. **116**, 9181–9185 (2019).

[72] V. Pistore, H. Nong, P.-B. Vigneron *et al.*, "Millimeter wave photonics with terahertz semiconductor lasers," Nat. Commun. **12**, 1427 (2021).

[73] A. Pagies, G. Ducournau, and J.-F. Lampin, "Low-threshold terahertz molecular laser optically pumped by a quantum cascade laser," APL Photonics **1**, 031302 (2016).

[74] P. Chevalier, A. Amirzhan, F. Wang *et al.*, "Widely tunable compact terahertz gas lasers," Science **366**, 856–860 (2019).

[75] I. S. Gregory, "The development of a continuous-wave terahertz imaging system," PhD Thesis, University of Cambridge (2004).

[76] F. Meyer, T. Vogel, S. Ahmed, and C. J. Saraceno, "Single-cycle, MHz repetition rate THz source with 66 mW of average power," Opt. Lett. **45**, 2494–2497 (2020).

[77] T. O. Buchmann, E. J. Railton Kelleher, M. Jazbinsek, B. Zhou, J.-H. Seok, O.-P. Kwon, F. Rotermund, and P. U. Jepsen, "High-power few-cycle THz generation at MHz repetition rates in an organic crystal," APL Photon. **5**, 106103 (2020).

[78] C. Paradis, J. Drs, N. Modsching, O. Razskazovskaya, F. Meyer, C. Kränkel, C. J. Saraceno, V. J. Wittwer, and T. Südmeyer, "Broadband terahertz pulse generation driven by an ultrafast thin-disk laser oscillator," Opt. Express **26**, 26377 (2018).

[79] F. Meyer, N. Hekmat, T. Vogel, A. Omar, S. Mansourzadeh, F. Fobbe, M. Hoffmann, Y. Wang, and C. J. Saraceno, "Milliwatt-class broadband THz source driven by a 112 W, sub-100 fs thin-disk laser," Opt. Express **27**, 30340 (2019).

[80] J. Drs, N. Modsching, C. Paradis, C. Kränkel, V. J. Wittwer, O. Razskazovskaya, and T. Südmeyer, "Optical rectification of ultrafast Yb lasers: pushing power and bandwidth of terahertz generation in GaP," J. Opt. Soc. Am. B **36**, 3039 (2019).

[81] T. O. Buchmann, E. J. Railton Kelleher *et al.*, "High-power few-cycle THz generation at MHz repetition rates in an organic crystal," APL Photon. **5**, 106103 (2020).

[82] K. Aoki, J. Savolainen, and M. Havenith, "Broadband terahertz pulse generation by optical rectification in GaP crystals," Appl. Phys. Lett. **110**, 201103 (2017).

[83] W. Jia, M. Liu, Y. Lu *et al.*, "Broadband terahertz wave generation from an epsilon-near-zero material," Light Sci. Appl. **10**, 11 (2021).

[84] Q. Tian, H. Xu, Y. Wang *et al.*, "Efficient generation of a high-field terahertz pulse train in bulk lithium niobate crystals by optical rectification," Opt. Express **29**, 9624 (2021).

[85] D. Zhai, E. Hérault, F. Garet, and J.-L. Coutaz, "Terahertz generation from ZnTe optically pumped above and below the bandgap," Opt. Express **29**, 17491 (2021).

[86] C. Gollner, M. Shalaby, C. Brodeur *et al.*, "Highly efficient THz generation by optical rectification of mid-IR pulses in DAST," APL Photon. **6**, 046105 (2021).

[87] W. Tian, G. Cirmi, H. T. Olgun, and others., "J-level multi-cycle terahertz generation in a periodically poled Rb:KTP crystal," Opt. Lett. **46**, 741 (2021).

[88] G. A. Valdivia-Berroeta, I. C. Tangen, C. B. Bahr *et al.*, "Crystal Growth, Tetrahertz Generation, and Optical Characterization of EHPSI-4NBS," J. Phys. Chem. C **125**, 16097–16102 (2021).

[89] D. Jang, C. Kang, S. K. Lee *et al.*, "Scalable terahertz generation by large-area optical rectification at 80 TW laser power," Opt. Lett. **44**, 5634 (2019).

[90] A. D. Koulouklidis, C. Gollner, V. Shumakova *et al.*, "Observation of extremely efficient terahertz generation from mid-infrared two-color laser filaments," Nat. Commun. **11**, 292 (2020).

[91] J. Yang and C. Wang, "Efficient terahertz generation scheme in a thin-film lithium niobate-silicon hybrid platform," Opt. Express **29**, 16477 (2021).

[92] M. Scheller, J. M. Yarborough, J. V. Moloney *et al.*, "Room temperature continuous wave milliwatt terahertz source," Opt. Express **18**, 27112 (2010).

[93] M. Scheller, J. R. Paul, A. Laurain *et al.*, "Terahertz generation by difference frequency conversion of two single-frequency VECSELs in an external resonance cavity," in "Vertical External Cavity Surface Emitting Lasers (VECSELs) IV," (SPIE, 2014), pp. 60 – 65.

[94] N. T. Yardimci and M. Jarrahi, "Nanostructure-Enhanced Photoconductive Terahertz Emission and Detection," Small p. 1802437 (2018).

[95] E. R. Brown, K. A. McIntosh, K. B. Nichols, and C. L. Dennis, "Photomixing up to 3.8 THz in low-temperature-grown GaAs," Appl. Phys. Lett. **66**, 285–287 (1995).

[96] J. E. Bjarnason, T. L. J. Chan, A. W. M. Lee *et al.*, "ErAs:GaAs photomixer with two-decade tunability and 12 μW peak output power," Appl. Phys. Lett. **85**, 3983–3985 (2004).

[97] R. Czarny, "Etude et réalisation d'une source THz accordable et de grande pureté spectrale," PhD Thesis, University of Lille (2007).

[98] U. Willer, R. Wilk, W. Schippers *et al.*, "A novel THz source based on a two-color Nd:LSB microchip-laser and a LT-GaAsSb photomixer," Appl. Phys. B **87**, 13–16 (2007).

[99] J. Mangeney, A. Merigault, N. Zerounian *et al.*, "Continuous wave terahertz generation up to 2 THz by photomixing on ion-irradiated $In_{0.53}Ga_{0.47}As$ at 1.55 μm wavelengths," Appl. Phys. Lett. **91**, 241102 (2007).

[100] C. Berry, N. Wang, M. Hashemi *et al.*, "Significant performance enhancement in photoconductive terahertz optoelectronics by incorporating plasmonic contact electrodes," Nat. Commun. **4**, 1622 (2013).

[101] S.-H. Yang, M. R. Hashemi, C. W. Berry, and M. Jarrahi, "7.5% Optical-to-Terahertz Conversion Efficiency Offered by Photoconductive Emitters With Three-Dimensional Plasmonic Contact Electrodes," IEEE Trans. Terahertz Sci. Technol. **4**, 575–581 (2014).

[102] Q. Qiu and Z. Huang, "Photodetectors of 2D Materials from Ultraviolet to Terahertz Waves," Adv. Mater. **33**, 2008126 (2021).

[103] I. Gregory, C. Baker, W. Tribe, I. Bradley, M. Evans, E. Linfield, A. Davies, and M. Missous, "Optimization of photomixers and antennas for continuous-wave terahertz emission," IEEE Journal of Quantum Electronics **41**, 717–728 (2005).

[104] S.-H. Yang, R. Watts, X. Li *et al.*, "Tunable terahertz wave generation through a bimodal laser diode and plasmonic photomixer," Opt. Express **23**, 31206 (2015).

[105] E. Peytavit, S. Lepilliet, F. Hindle *et al.*, "Milliwatt-level output power in the sub-terahertz range generated by photomixing in a GaAs photoconductor," Appl. Phys. Lett. **99**, 223508 (2011).

[106] M. Billet, P. Latzel, F. Pavanello *et al.*, "Resonant cavities for efficient LT-GaAs photoconductors operating at 1550 nm," APL Photon. **1**, 076102 (2016).

[107] T. Ishibashi, N. Shimizu, S. Kodama *et al.*, "Uni-traveling-carrier photodiodes," in "Ultrafast Electronics and Optoelectronics," , vol. 13 (Optical Society of America, 1997), vol. 13, p. paper UC3.

[108] T. Ishibashi and H. Ito, "Uni-traveling-carrier photodiodes," J. Appl. Phys **127**, 031101 (2020).

[109] P. Latzel, F. Pavanello, M. Billet *et al.*, "Generation of mW Level in the 300-GHz Band Using Resonant-Cavity-Enhanced Unitraveling Carrier Photodiodes," IEEE Trans. THz Sci. Technol. **7**, 800–807 (2017).

[110] S. Nellen, T. Ishibashi, A. Deninger *et al.*, "Experimental Comparison of UTC- and PIN-Photodiodes for Continuous-Wave Terahertz Generation," J Infrared Milli Terahertz Waves **41**, 343–354 (2020).

[111] H. Ito and T. Ishibashi, "Photonic Terahertz-Wave Generation Using Slot-Antenna-Integrated Uni-Traveling-Carrier Photodiodes," IEEE J. Select. Topics Quantum Electron. **23**, 1–7 (2017).

[112] T. Harter, S. Muehlbrandt, S. Ummethala *et al.*, "Silicon–plasmonic integrated circuits for terahertz signal generation and coherent detection," Nat. Photon. **12**, 625–633 (2018).

[113] G. Ducournau, "Silicon photonics targets terahertz region," Nat. Photon. **12**, 574–575 (2018).

[114] T. Harter, S. Ummethala, M. Blaicher *et al.*, "Wireless THz link with optoelectronic transmitter and receiver," Optica **6**, 1063 (2019).

[115] S. Ummethala, T. Harter, K. Koehnle *et al.*, "THz-to-optical conversion in wireless communications using an ultra-broadband plasmonic modulator," Nat. Photon. **13**, 519–524 (2019).

[116] N. Shimizu, Y. Miyamoto, and T. Ishibashi, "Uni-traveling-carrier photodiodes," 1999 IEEE LEOS Annual Meeting Conference Proceedings. LEOS'99. 12th Annual Meeting. IEEE Lasers and Electro-Optics Society 1999 Annual Meeting (Cat. No.99CH37009) (1999).

[117] H. Ito, T. Furuta, F. Nakajima *et al.*, "Photonic generation of continuous THz wave using uni-traveling-carrier photodiode," J. Light. Technol. **23**, 4016–4021 (2005).

[118] S. Blin, R. Paquet, M. Myara *et al.*, "Coherent and Tunable THz Emission Driven by an Integrated III–V Semiconductor Laser," IEEE J. Sel. Top. Quantum Electron. **23**, 1–11 (2017).

[119] T. H. Maiman, "Stimulated Optical Radiation in Ruby," Nature **187**, 493–494 (1960).

[120] M. Sellahi, "Laser à semi-conducteur III-V à émission verticale de haute cohérence et de forte puissance : Etat vortex, continuum et bifréquence THz," PhD Thesis, University of Montpellier (2014).

[121] A. Forbes, M. de Oliveira, and M. R. Dennis, "Structured light," Nat. Photon. **15**, 253–262 (2021).

[122] A. E. Siegman, *Lasers* (University Science Books, 1986).

[123] G. P. Agrawal and N. K. Dutta, *Semiconductor Lasers* (Springer, 1993).

[124] L. A. Coldren, S. W. Corzine, and M. Mashanovitch, *Diode lasers and photonic integrated circuits* (Wiley, 2012).

[125] M. Guina, A. Rantamäki, and A. Härkönen, "Optically pumped VECSELs: review of technology and progress," J. Phys. D: Appl. Phys. **50**, 383001 (2017).

[126] A. C. Tropper, H. D. Foreman, A. Garnache *et al.*, "Vertical-external-cavity semiconductor lasers," J. Phys. D: Appl. Phys. **37**, R75–R85 (2004).

[127] S. Blin, "Photonics." Master lectures, University of Montpellier .

[128] H. Abbaspour, V. Ahmadi, and M. H. Yavari, "Analysis of qd vcsel dynamic characteristics considering homogeneous and inhomogeneous broadening," IEEE J. Sel. Top. Quantum Electron. **17**, 1327–1333 (2011).

[129] H. Kogelnik and T. Li, "Laser beams and resonators," Appl. Opt. **5**, 1550–1567 (1966).

[130] A. L. Schawlow and C. H. Townes, "Infrared and Optical Masers," Phys. Rev. **112**, 1940–1949 (1958).

[131] C. Henry, "Theory of the phase noise and power spectrum of a single mode injection laser," IEEE J. Quantum Electron. **19**, 1391–1397 (1983).

[132] B. Rudin, A. Rutz, M. Hoffmann *et al.*, "Highly efficient optically pumped vertical-emitting semiconductor laser with more than 20 W average output power in a fundamental transverse mode," Opt. Lett. **33**, 2719–2721 (2008).

[133] M. S. Seghilani, "Highly coherent III-V-semiconductor laser emitting phase-, amplitude- and polarization-structured light for advanced sensing applications: Vortex, SPIN, Feedback Dynamics," PhD Thesis, University of Montpellier .

[134] A. Garnache, A. Ouvrard, and D. Romanini, "Single–Frequency operation of External–Cavity VCSELs: Non-linear multimode temporal dynamics and quantum limit." Opt. Express **15**, 9403–9417 (2007).

[135] A. Laurain, M. Myara, G. Beaudoin, I. Sagnes, and A. Garnache, "High power single–frequency continuously–tunable compact extended–cavity semiconductor laser," Opt. Express **17**, 9503–9508 (2009).

[136] A. Garnache, S. Hoogland, A. C. Tropper *et al.*, "Sub-500-fs soliton-like pulse in a passively mode-locked broadband surface-emitting laser with 100-mW average power," Appl. Phys. Lett. **80**, 3892 (2002).

[137] J. I. Chanin, *Fundamentals of laser dynamics* (Cambridge, 2006).

[138] P. J. Moore, Z. J. Chaboyer, and G. Das, "Tunable dual-wavelength fiber laser," Opt. Fiber Technol. **15**, 377–379 (2009).

[139] F. Siebe, K. Siebert, R. Leonhardt, and H. G. Roskos, "A Fully Tunable Dual–Color CW Ti:Al_2O_3 Laser," IEEE J. Quantum Electron. **35**, 1731–1736 (1999).

[140] N. Kim, J. Shin, E. Sim *et al.*, "Monolithic dual-mode distributed feedback semiconductor laser for tunable continuous-wave terahertz generation," Opt. Express **17**, 13851–13859 (2009).

[141] X. Liu, X. Yang, F. Lu *et al.*, "Stable and uniform dual–wavelength erbium–doped fiber laser based on fiber Bragg gratings and photonic crystal fiber," Opt. Express **13**, 142–147 (2005).

[142] S. Roh, R. Swint, A. Jones *et al.*, "Dual-wavelength asymmetric cladding InGaAs-GaAs ridge waveguide distributed Bragg reflector lasers," IEEE Photon. Technol. Lett. **11**, 15–17 (1999).

[143] H. Kim, P. van der Wal, A. Schmitz, and R. Gusten, "Power Stabilization of the Dual-Mode Laser Using Volume Holographic Gratings," J. Light. Technol. **26**, 1317–1322 (2008).

[144] N. Wang and M. Jarrahi, "Noise Analysis of Photoconductive Terahertz Detectors," J. Infrared Millim. Terahertz Waves **34**, 519–528 (2013).

[145] F. Pozzi, R. M. De La Rue, and M. Sorel, "Dual-Wavelength InAlGaAs–InP Laterally Coupled Distributed Feedback Laser," IEEE Photon. Technol. Lett. **18**, 2563–2565 (2006).

[146] T. Leinonen, Y. Morozov, A. Harkonen, and M. Pessa, "Vertical external-cavity surface-emitting laser for dual-wavelength generation," IEEE Photon. Technol. Lett. **17**, 2508–2510 (2005).

[147] M. Matus, M. Kolesik, J. V. Moloney *et al.*, "Dynamics of two-color laser systems with spectrally filtered feedback," J. Opt. Soc. Am. B **21**, 1758–1771 (2004).

[148] C.-S. Friedrich, C. Brenner, S. Hoffmann *et al.*, "New Two-Color Laser Concepts for THz Generation," IEEE J. Sel. Top. Quantum Electron. **14**, 270–276 (2008).

[149] I. Park, C. Sydlo, I. Fischer, W. Elsäßer, and H. L. Hartnagel, "Generation and spectroscopic application of tunable continuous-wave terahertz radiation using a dual-mode semiconductor laser," Meas. Sci. Technol. **19**, 065305 (2008).

[150] S. Hoffmann and M. Hofmann, "Generation of Terahertz radiation with two color semiconductor lasers," Laser Photonics Rev. **1**, 44–56 (2007).

[151] M. Alouini, M. Brunel, F. Bretenaker *et al.*, "Dual tunable wavelength Er,Yb:glass laser for terahertz beat frequency generation," IEEE Photon. Technol. Lett. **10**, 1554–1556 (1998).

[152] M. Brunel, F. Bretenaker, and A. Le Floch, "Tunable optical microwave source using spatially resolved laser eigenstates," Opt. Lett. **22**, 384–386 (1997).

[153] G. Danion, C. Hamel, L. Frein *et al.*, "Dual frequency laser with two continuously and widely tunable frequencies for optical referencing of GHz to THz beatnotes," Opt. Express **22**, 17673–17678 (2014).

[154] R. Czarny, M. Alouini, C. Larat *et al.*, "THz-dual-frequency Yb^{3+}:$KGd(WO_4)_3$ laser for continuous wave THz generation through photomixing," Electron. Lett. **40**, 942–943 (2004).

[155] A. Brenier, "Tunable THz frequency difference from a diode-pumped dual-wavelength Yb^{3+}:$KGd(WO_4)_3$ laser with chirped volume Bragg gratings," Laser Phys. Lett. **8**, 520–524 (2011).

[156] F. A. Camargo, J. Barrientos, G. Baili *et al.*, "Coherent dual-frequency emission of a vertical external-cavity semiconductor laser at the cesium d_2 line," IEEE Photon. Technol. Lett. **24**, 1218–1220 (2012).

[157] A. Rolland, G. Loas, M. Brunel *et al.*, "Non-linear optoelectronic phase-locked loop for stabilization of opto-millimeter waves: towards a narrow linewidth tunable THz source," Opt. Express **19**, 17944–17950 (2011).

[158] A. E. Amili, G. Loas, S. De *et al.*, "Experimental demonstration of a dual-frequency laser free from anti-phase noise," Opt. Lett. **37**, 4901–4903 (2012).

[159] G. Baili, L. Morvan, M. Alouini *et al.*, "Experimental demonstration of a tunable dual-frequency semiconductor laser free of relaxation oscillations," Opt. Lett. **34**, 3421–3423 (2009).

[160] R. Paquet, S. Blin, M. Myara *et al.*, "Coherent continuous-wave dual-frequency high-Q external-cavity semiconductor laser for GHz–THz applications," Opt. Lett. **41**, 3751–3754 (2016).

[161] C. A. Balanis, *Antenna theory: analysis and design* (John Wiley, 2005).

[162] D. S. Prinsloo, M. V. Ivashina, R. Maaskant, and P. Meyer, "Beamforming strategies for active multi-mode antennas: Maximum gain, Signal-to-Noise ratio, and polarization discrimination," in "2014 International Conference on Electromagnetics in Advanced Applications (ICEAA)," (IEEE, Palm Beach, Aruba, 2014), pp. 507–510.

[163] D. Prinsloo, P. Meyer, R. Maaskant, and M. V. Ivashina, "Conical quad-mode antenna with integrated tapered slot antennas for wide-field polarimetry," in "2015 IEEE-APS Topical Conference on Antennas and Propagation in Wireless Communications (APWC)," (IEEE, Torino, Italy, 2015), pp. 1235–1238.

[164] P. Meyer and D. S. Prinsloo, "Generalized Multimode Scattering Parameter and Antenna Far-Field Conversions," IEEE Trans. Antennas Propag. **63**, 4818–4826 (2015).

[165] D. S. Prinsloo, A. Alayon Glazunov, R. Maaskant *et al.*, "Characterization and Performance of an Ultra-Wideband Wide-Coverage Multimode MIMO Antenna," IEEE Trans. Antennas Propagat. **67**, 5812–5823 (2019).

[166] Tzung-I, Lee and Yuanxun, Ethan Wang, "A planar multipolar antenna for MIMO applications," in "2007 IEEE Antennas and Propagation Society International Symposium," (IEEE, Honolulu, HI, 2007), pp. 2429–2432.

[167] Z. Xu, X. Dong, and J. Bornemann, "Design of a Reconfigurable MIMO System for THz Communications Based on Graphene Antennas," IEEE Trans. THz Sci. Technol. **4**, 609–617 (2014).

[168] S. Bretin, "Communications sans fil aux fréquences terahertz : Applications à la vidéo haute définition temps réel." PhD Thesis, Université de Lille (2019).

[169] N. M. Burford and M. O. El-Shenawee, "Review of terahertz photoconductive antenna technology," Optical Engineering **56**, 010901 (2017).

[170] K. Kitahara, K. Oto, M. Nakajima, and K. Muro, "Note: Development of a high resolution and wide band terahertz spectrometer based on a 1 μm–band external cavity diode laser," Rev. Sci. Instrum. **84**, 126102 (2013).

[171] F. Kartner, I. Jung, and U. Keller, "Soliton mode-locking with saturable absorbers," IEEE J. Sel. Topics Quantum Electron. **2**, 540–556 (1996).

[172] U. Keller, K. Weingarten, F. Kartner *et al.*, "Semiconductor saturable absorber mirrors (SESAM's) for femtosecond to nanosecond pulse generation in solid-state lasers," IEEE J. Sel. Top. Quantum Electron. **2**, 435–453 (1996).

[173] G. Steinmeyer, "Frontiers in Ultrashort Pulse Generation: Pushing the Limits in Linear and Nonlinear Optics," Science **286**, 1507–1512 (1999).

[174] U. Keller, "Recent developments in compact ultrafast lasers," Nature **424**, 831–838 (2003).

[175] U. Keller and A. C. Tropper, "Passively modelocked surface-emitting semiconductor lasers," Phys. Rep. **429**, 67–120 (2006).

[176] A. H. Quarterman, K. G. Wilcox, V. Apostolopoulos *et al.*, "A passively mode–locked external–cavity semiconductor laser emitting 60–fs pulses," Nat. Photon. **3**, 729–731 (2009).

[177] S. M. Link, D. J. H. C. Maas, D. Waldburger, and U. Keller, "Dual-comb spectroscopy of water vapor with a free-running semiconductor disk laser," Science **356**, 1164–1168 (2017).

[178] K. Ursula, "Ultrafast lasers," Book, Springer (2021).

[179] T. C. Sverre, A. P. Turnbull, P. C. Gow *et al.*, "Mode-locked VECSEL SESAM with intracavity antenna for terahertz emission," Proc. SPIE 10087, Vertical External Cavity Surface Emitting Lasers (VECSELs) VII **100870O**, 124–130 (2017).

[180] Y. Nan and L. W. Zhong, "Handbook of microscopy for nanotechnology," Book, Springer (2005).

[181] B. Bharat, "Handbook of nanotechnology," Book, Springer (2017).

[182] D. Turan, S. C. Corzo-Garcia, N. T. Yardimci *et al.*, "Impact of the Metal Adhesion Layer on the Radiation Power of Plasmonic Photoconductive Terahertz Sources," J. Infrared Millim Terahertz Waves **38**, 1448–1456 (2017).

[183] V. Elfady, "Émission térahertz par photo–mélange," Master Thesis, University of Montpellier (2021).

[184] A. Kerchaoui, "Sources térahertz photo–mélangées par antennes photoconductrices térahertz," Master Thesis, University of Montpellier (2017).

[185] J. B. Leonard, "Contact to semiconductors," Book, Noyes Publiations (1994).

[186] S. M. Sze and K. K. Ng, "Physics of semiconductor devices," Book, Wiley-Interscience (2007).

Sources térahertz photo–mélangées par antennes photoconductrices térahertz multipolaires

Résumé du projet de thèse : Longtemps restreint au domaine de l'astronomie, la récente exploitation des ondes électromagnétiques aux fréquences térahertz (1 THz = 10^{12} Hz) a permis de mettre en valeur un intérêt dans d'autres domaines tels que la spectroscopie THz, le contrôle non–destructif industriel, la sécurité et les télécommunications. Cependant, le manque de sources compatibles à des exploitations industrielles restreint le développement des possibles applications à ces fréquences. Cette thèse s'intéresse aux sources THz photo–mélangées continues, dont le principe consiste à superposer deux faisceaux lasers de fréquences proches (différence de fréquences proche de 1 THz) afin de permettre au battement optique résultant d'exciter un photo–mélangeur rayonnant à l'aide d'une antenne un signal à la différence de fréquence. Afin d'éviter un bruit de fréquence excessif qui résulterait d'une simple transposition du bruit de fréquence optique, une source bi–fréquence est utilisée afin d'assurer une corrélation entre les bruits des deux signaux, offrant in fine lors du battement une réduction de quatre ordres de grandeur du bruit de fréquence. La source utilisée est un laser semi–conducteur (InGaAs/GaAs) à émission verticale en cavité externe fonctionnant sur deux modes transverses de Laguerre–Gauss (LG) grâce à l'intégration de masques de pertes, l'un des modes étant le mode Gaussien fondamental, l'autre étant un mode d'ordre supérieur sans énergie au centre (typiquement LG_{0n} avec $n = 2, 3$ ou 4). Le laser réalisé émet un faisceau à une longueur d'onde de 1064 nm offrant plusieurs spots (2*n) dans l'espace transverse, où les 2 modes se superposent, générant ainsi un battement THz. Afin d'utiliser l'intégralité des spots disponibles et de démultiplier la puissance THz par le nombre de spots, l'étude d'antennes multipolaires a été effectuée, montrant de surcroît une possible exaltation du gain de deux antennes dipôles croisées comparé à un dipôle simple (6.5 dBi versus 2.2 dBi). Cependant, peu de photo–mélangeurs sont rapportés dans la littérature pour des excitations à la longueur d'onde de 1064 nm, malgré la disponibilité de composants et de lasers matures à forte puissance. L'étude d'un miroir à absorbant saturable rapide, constitué d'un puits quantique InGaAs/GaAs en surface (afin de réduire la durée de vie), a permis de montrer un effet photo–conducteur encourageant pour une possible émission THz, et l'étude d'électrodes plasmoniques sur InGaAs/GaAs a permis de démontrer une première émission THz continue. La continuité de ce travail peut ouvrir ainsi la voie à des sources THz continues 6 à 8 fois plus puissantes avec une efficacité de conversion optique–THz accrue et un gain de rayonnement supérieur aux solutions existantes.

MOTS-CLÉS : Lasers, antennes, semiconducteur, térahertz, photo-mélangeur

---

Photomixed terahertz emitters by multipolar photoconductive terahertz antennas

Summary of the thesis project: Longtime restricted to the field of astronomy, the recent exploitation of electromagnetic waves at terahertz frequencies (1 THz = 10^{12} Hz) has highlighted an interest in other areas such as THz spectroscopy, industrial non–destructive testing, security and telecommunications. However, the lack of compatible sources for industrial use restricts the development of possible applications at these frequencies. This thesis focuses on continuous photomixed THz sources, whose working principle consists in superimposing two laser beams of close frequencies (frequency difference close to 1 THz) in order to allow the resulting optical beat to excite a photomixer radiating with the help of an antenna a signal at the frequency difference. In order to avoid an excessive frequency noise which would result from a simple transposition of the optical frequency noise, a bi-frequency source is used to ensure a correlation between the noises of the two signals, offering in the presence of the beating a reduction of four orders of magnitude of the frequency noise. The used source is a semiconductor laser (InGaAs/GaAs) with vertical emission in external cavity operating on two transverse Laguerre–Gauss (LG) modes thanks to the integration of loss masks, one of the modes being the fundamental Gaussian mode, the other being a higher order mode without energy at the center (typically LG_{0n} with $n = 2, 3$ or 4). The realized laser emits a beam at a wavelength of 1064 nm offering several spots (2*n) in the transverse space, where the 2 modes are superimposed, thus generating a THz beat. In order to use all the available spots and to multiply the THz power by the number of spots, the study of multipolar antennas has been performed, showing in addition a possible exaltation of the gain of two crossed dipole antennas compared to a single dipole (6.5 dBi versus 2.2 dBi). However, few photomixers are reported in the literature for excitations at the wavelength of 1064 nm, despite the availability of mature high–power components and lasers. The study of a fast saturable absorber mirror, constituted by an InGaAs/GaAs quantum well on the surface (in order to reduce the lifetime), allowed to show a photoconductive effect encouraging for a possible THz emission, and the study of plasmonic electrodes on InGaAs/GaAs allowed to demonstrate a first continuous THz emission. The continuity of this work may open the way to continuous THz sources 6 to 8 times more powerful with an increased optical-THz conversion efficiency and a radiation gain superior to existing solutions.

KEYWORDS: Lasers, antennas, semiconductor, terahertz, photomixer